

Die approbierte Originalversion dieser Dissertation ist in der Hauptbibliothek der Technischen Universität Wien aufgestellt und zugänglich.

<http://www.ub.tuwien.ac.at>

The approved original version of this thesis is available at the main library of the Vienna University of Technology.

<http://www.ub.tuwien.ac.at/eng>



DISSERTATION

The Reconstructed $\text{Fe}_3\text{O}_4(001)$ Surface as an Adsorption Template

ausgeführt zum Zwecke der Erlangung des akademischen Grades eines
Doktors der technischen Wissenschaften unter der Leitung von

Univ.-Prof. Dr. Ulrike Diebold

eingereicht an der Technischen Universität Wien
bei der Fakultät für Physik

von

Ing. Zbynek Novotny
Matrikelnummer: 0828690
Wiedn. Hauptstraße 8-10
1040 Wien

Wien, im September 2013

Acknowledgement

First of all, I am grateful to Prof. Ulrike Diebold for supervision during my doctorate research, for her scientific support, and for providing an encouraging environment within her group. Besides my advisor, I would like to thank Dr. Gareth S. Parkinson for co-supervision and numerous fruitful discussions during last three years. I am also very thankful to Prof. Michael Schmid, who introduced me to the world of surface science and the related experimental techniques.

I take this opportunity to record my sincere thanks to all the faculty members of IAP group. Prof. Peter Blaha, Rukan Kosak, T. A. Manz, and R. Pentcheva for their collaboration and extensive theoretical work.

I am grateful to Margareta Wagner for helping me with the german version of the abstract. The author acknowledges Prof. Z. Mao and T. J. Liu from Tulane University for the growth of synthetic Fe_3O_4 samples, Juan de la Figuera for fruitful discussion about magnetite, and U.S. Department of Energy for a financial support.

Last but not least, I want to thank my friends Jana, Claudia, Irati, Ivana, Marina, Zuzana, and Petra for their support during my time in Vienna.

Vienna, September 2013

Z. N.

Abstract (English)

Magnetite, Fe_3O_4 , is a fascinating material for its electronic, magnetic, and catalytic properties. Fe_3O_4 crystallizes in the inverse spinel structure. In the (001) direction, the crystal is composed of an alternating stack of A layers (containing tetrahedral FeA atoms), and B layers (octahedral FeB and O atoms). This thesis investigates the (001) B layer surface.

The B layer surface forms a $(\sqrt{2} \times \sqrt{2}) R45^\circ$ reconstruction. Here, pairs of FeB and neighboring O ions are slightly displaced laterally, forming undulating rows with two inequivalent FeA bulk continuation sites. We term these narrow and wide sites, and a preference for adsorbates to occupy the narrow site is a common theme in this work.

The most common defects on this surface are oxygen vacancies (V_O 's). These readily dissociate water molecules at room temperature (RT), forming pairs of surface OH groups. Another common defect are anti-phase domain boundaries (APDBs). APDBs are formed on the surface because the $(\sqrt{2} \times \sqrt{2}) R45^\circ$ reconstruction has two equivalent domains with respect to the bulk structure. Where two inequivalent domains meet, an APDB is formed. Simulated scanning tunneling microscopy (STM) images reproduce the appearance of the APDBs in the experimental data and reveal that they are preferential adsorption sites for hydroxyl groups. Water adsorbs dissociatively also in the absence of V_O 's, up to a saturation coverage of 0.66 ML of surface OH (1 ML = 1.42×10^{14} atoms/cm²). However, STM images of the water-exposed $\text{Fe}_3\text{O}_4(001)$ surface appear identical to those obtained following deposition of atomic H, with no evidence for the water hydroxyl (OH) species. The absence of the OH is confirmed by low energy He⁺ ion scattering utilizing H₂¹⁸O. Annealing of the hydrogenated surface leads to the abstraction of lattice O atoms and desorption of water.

At RT, Fe adsorbs as single adatoms for low coverage, and as adatoms and clusters for higher coverage. Mild annealing of the sample leads to a surface containing Fe monomers (FeA) and Fe octahedral pairs (Fe-OP) at narrow sites. Two-fold coordinated FeA and 5-fold coordinated Fe-OP form at 423 K, while only Fe-OP's are observed at 573 K. For higher Fe coverage the surface exhibits an FeO-like structure with all surface octahedral sites filled with Fe cations. X-ray photoelectron spectroscopy indicates that all Fe-rich surfaces contain mostly Fe²⁺.

The $(\sqrt{2} \times \sqrt{2}) R45^\circ$ reconstructed B layer surface acts as a rather robust adsorption-template. At fractional monolayer coverages and at RT, H, Fe, Au, and Pd adsorb as single adatoms at the narrow sites of the surface unit cell, forming ordered structures on the surface.

Supported Au atoms show a remarkable stability, both chemically in up to 10^{-4} mbar of CO, and thermally up to 673 K. At higher annealing temperatures, different sizes of three-dimensional Au clusters are observed. XPS measurements are consistent with a positive charge state of the single adatoms.

For Pd adatoms, CO induces mobility via formation of a Pd-CO complex. When at least three Pd-CO meet on the surface, homogeneous nucleation of a cluster takes place. Clusters grow through cluster migration and coalescence. Surface OH groups have the opposite effect to CO,

Acknowledgement

immobilizing the Pd-CO group and stabilizing an Pd adatom on the surface.

Abstract (Deutsch)

Magnetit, Fe_3O_4 , ist ein faszinierendes Material aufgrund seiner elektronischen, magnetischen, und katalytischen Eigenschaften. Fe_3O_4 kristallisiert in der inversen Spinnellstruktur. In der (001)-Richtung wird der Kristall durch ein alternierendes Stapeln einer A-Schicht (tetraedrische FeA Atome) und einer B-Schicht (oktaedrische FeB und O-Atome) gebildet. Diese Arbeit untersucht die (001) Oberfläche B-Schicht.

Die B-Schicht bildet eine $(\sqrt{2} \times \sqrt{2}) R45^\circ$ Rekonstruktion. Dazu werden Paare von benachbarten FeB und O-Ionen leicht seitlich verschoben, sodass sich wellenförmige Reihen mit zwei inäquivalenten Plätzen bilden. Diese werden hier als schmale und breite Plätze bezeichnet. Die häufigsten Defekte auf dieser Oberfläche sind Sauerstoff-Fehlstellen (V_O), an denen Wassermoleküle bei Raumtemperatur (RT) dissoziieren und Paare von OH Gruppen an der Oberfläche bilden. Ein weiterer häufiger Defekt sind anti-phases Domänengrenzen (APDG). APDG bilden sich auf der Oberfläche, da die $(\sqrt{2} \times \sqrt{2}) R45^\circ$ Rekonstruktion zwei Domänen in Bezug auf die Volumsstruktur besitzt. Treffen zwei inäquivalente Domänen aufeinander, bildet sich eine APDG. Simulationen der Rastertunnelmikroskopbilder (RTM) reproduzieren das Aussehen der APDG der experimentellen Daten und zeigen, dass sie bevorzugte Adsorptionsplätze für Hydroxyl-Gruppen sind.

Wasser adsorbiert dissoziativ auch in Abwesenheit von V_O bis zu einer Sättigungsbedeckung von 0,66 ML (1 ML = $1,42 \times 10^{14}$ Atome/cm²). Nach der Adsorption von Wasser auf $\text{Fe}_3\text{O}_4(001)$ schaut die Oberfläche in RTM gleich aus wie nach der Adsorption von atomaren H; es gibt keine Hinweise über den Verbleib Wasser-Hydroxyl (OH)-gruppen. Das Fehlen von OH wird durch niederenergetische He^+ Ionenstreuung und der Verwendung von H_2^{18}O bestätigt. Tempern der hydrierten Oberfläche führt zu Abstraktion der Gitter O-Atome und der Desorption von Wasser.

Bei RT und niedriger Bedeckung adsorbiert Fe als einzelne Adatome, bei höherer Bedeckung findet man Adatome und Cluster. Schwaches Tempern der Probe führt zu einer Oberfläche, auf der Fe Monomere (FeA) und oktaedrischen Fe-Paare (Fe-OP) in den schmalen Plätzen der Oberflächenrekonstruktion sitzen. Zweifach koordinierte FeA und fünffach koordinierte Fe-OP bilden sich bei 423 K, während ausschliesslich Fe-OP bei 573 K beobachtet wurden. Bei höherer Fe Bedeckung weist die Oberfläche eine FeO-Struktur auf, bei der alle Oktaederlücken mit Fe-Kationen gefüllt sind. Röntgen-Photoelektronenspektroskopie zeigt, dass alle Fe-reichen Oberflächen großteils Fe^{2+} enthalten.

Die $(\sqrt{2} \times \sqrt{2}) R45^\circ$ rekonstruierte B-Schicht ist eine relativ robust Vorlage für Adsorption. Bedeckungen unter eine Monolage und bei RT, von H, Fe, Au, und Pd adsorbieren als einzige Adatome an den schmalen Plätzen der Oberfläche und bilden so geordnete Strukturen.

Au-Atome zeigen eine bemerkenswerte Stabilität, sowohl chemisch in bis zu 10^{-4} mbar CO, als auch thermisch bis zu einer Probertemperatur von 673 K. Bei höheren Temperaturen wurden drei-dimensionale Au-Cluster unterschiedlicher Größe beobachtet. XPS-Messungen

Acknowledgement

stehen im Einklang mit einer positiven Ladung der einzelnen Au-Adatome.

Bei Pd Adatomen induziert CO Mobilität durch Bildung eines Pd-CO Komplexes. Wenn sich mindestens drei Pd-CO auf der Oberfläche treffen, erfolgt homogene Keimbildung zu einem Cluster. Diese Cluster wachsen durch Migration und Koaleszenz. OH-Gruppen an der Oberfläche haben den gegenteiligen Effekt zu CO: Immobilisierung der Pd-CO Gruppe und Stabilisierung eines Pd Adatoms auf der Oberfläche.

List of abbreviations

APDB	Anti-phase domain boundaries
e-beam	electron beam
FeA	Fe atoms in tetrahedral sites
FeB	Fe atoms in octahedral sites
FFT	Fast Fourier transform
LEED	Low energy electron diffraction
LEIS	Low energy ion scattering
LDOS	Local density of states
LN ₂	Liquid nitrogen
ML	Monolayer
NSC	Natural single crystal
OP	Octahedral pair
QCM	Quartz crystal microbalance
QMS	Quadrupole mass spectrometer
RHEED	Reflection high energy electron diffraction
RT	Room Temperature
S	Surface layer
S-1	First subsurface layer
SEM	Scanning electron microscope
SIMS	Secondary ion mass spectroscopy
SMOKE	Surface magneto-optical Kerr effect
STM	Scanning tunneling microscopy
SSC	Synthetic single crystal
STEM	Scanning transmission electron microscope
STS	Scanning tunneling spectroscopy
TOF	Turnover frequency (of a catalytic reaction)
TPD	Temperature programmed desorption
TSP	Titanium sublimation pump
UHV	Ultra-high vacuum
XPS	X-ray photoelectron spectroscopy
WGS	Water-gas shift reaction

Contents

Acknowledgement	iii
Abstract (English/Deutsch)	v
List of abbreviations	ix
1 Introduction	1
1.1 Heterogeneous catalysis	1
1.1.1 Supported nanoparticles: the size effect	1
1.1.2 Cluster nucleation and sintering	2
1.1.3 Single atom catalyst	4
2 Iron oxides	5
2.1 Fe ₃ O ₄	6
2.2 Fe ₃ O ₄ (001)	6
3 Experimental techniques	9
3.1 Scanning tunneling microscopy (STM)	9
3.2 X-ray photoelectron spectroscopy (XPS)	11
3.3 Low energy ion scattering (LEIS)	11
3.4 Molecular beam epitaxy (MBE)	12
3.5 Experimental setups	12
3.5.1 RT STM system	12
3.5.2 SPECS system	13
3.5.3 PINUP system	13
4 Experimental details	15
4.1 Samples	15
4.2 Sample mount for UHV experiments	16
4.3 Sample preparation	16
4.4 Evaporation materials	18
4.5 Liquids and gases	19
4.6 Analysis of experimental data	19
4.7 Definitions	19

Contents

5	Fe₃O₄(001) B layer: Adsorption of simple molecules	21
5.1	Adsorption of atomic H	21
5.2	Adsorption of H ₂ O and D ₂ O	22
5.2.1	Results	23
5.2.2	Discussion	27
6	Fe₃O₄(001) B layer: Typical defects	29
6.1	Surface anti-phase domain boundaries	29
6.1.1	Discussion	31
6.2	Other typical defects	31
7	Fe-rich (001) surface terminations	33
7.1	Deposition of Fe onto the B layer surface	34
7.1.1	Fe deposition at RT: adatoms and clusters	34
7.1.2	Fe octahedral pairs	35
7.1.3	High Fe coverage	38
7.1.4	Fe-rich terminations of Fe ₃ O ₄ (001): electronic structure	40
7.1.5	Discussion	42
7.2	Influence of sample preparation on the surface termination	43
7.3	Outlook	44
8	Template-induced adsorption	47
8.1	Au-Fe ₃ O ₄ (001)	47
8.1.1	Initial Au adsorption	48
8.1.2	Chemical stability of Au adatoms	49
8.1.3	Thermal stability of Au adatoms	51
8.1.4	Higher Au coverage: adatoms and clusters	52
8.1.5	Spectroscopic measurements	56
8.1.6	Discussion	57
8.1.7	Conclusion	59
8.2	Pd-Fe ₃ O ₄ (001)	60
8.2.1	Sub-monolayer Pd coverage: Pd adatoms	60
8.2.2	Formation of Pd clusters	66
8.2.3	Additional considerations	67
8.2.4	Outlook	68
8.3	Monte Carlo simulation of metal adsorption at RT	69
8.3.1	Discussion	72
9	Conclusion	75
A	List of known features on the Fe₃O₄(001) surface	77
B	List of samples	81
B.1	Sample-dependent surface terminations	84
B.1.1	Fe ₃ O ₄ (001)361 SSC	84
B.1.2	Fe ₃ O ₄ (001)349 NSC	86
B.1.3	Fe ₃ O ₄ (001)370 NSC	87
B.1.4	Fe ₃ O ₄ (001)/MgO(001) thin film	88

List of figures	90
List of tables	93
Bibliography	103

1 Introduction

The aim of this thesis is to investigate the surface properties of $\text{Fe}_3\text{O}_4(001)$ single crystals. Initially, the goal was to identify the surface defects, to find active adsorption sites on the surface, and to investigate adsorption of molecules. During the course of the experiments, a rather surprising adsorption property of the reconstructed (001) surface was discovered. We found that this surface is capable to stabilize single atomic species at elevated temperatures, i. e., well above room temperature (RT). In contrast, single metal atoms tend to agglomerate into clusters already at temperatures well below RT on most other oxide materials [1]. Consequently, the $\text{Fe}_3\text{O}_4(001)$ surface is, potentially, an important substrate in the emerging field of the single atom catalysts [2].

1.1 Heterogeneous catalysis

In heterogeneous catalysis, the phase of the catalysts differs from the phase of the reactants. Typically, the catalyst is a solid, while the reactants are gases or liquids. Heterogeneous catalysis plays a vital role in the industry. The catalyst has an influence on the thermodynamics of a chemical reactions. It can either promote the chemical reaction, or inhibit another one. Typical catalysts are coinage metals (Pd, Pt, Au, Cu etc.). Many industrially important chemical reactions will be not feasible without the use of a catalysts. However, the full understanding of the underlying principles in heterogeneous catalysis is still not complete.

1.1.1 Supported nanoparticles: the size effect

Nanoparticles (or clusters) often have a significantly higher catalytic activity compared to their bulk counterparts [3, 4]. The interesting and often unexpected properties of nanoparticles are caused by the large surface area. The enhanced activity of the small nanoparticles has been ascribed to a number of effects, including the non-metallic character of these particles [5], under-coordinated atoms within the nanoparticles, metal/metal-oxide support interaction, or charge transfer from the support [6]. Pioneering work in this field was performed by Haruta with his discovery of the remarkable activity of gold nanoparticles [7]. Gold is the least reactive metal. In heterogeneous catalysis, smooth gold surfaces and gold nanoparticles with a diameter above 10 nm have little practical use. However, nano-sized gold particles supported on

selected metal oxides can dramatically enhance catalytic activity for many important chemical reactions [7]. The exact role of gold nanoparticles is still under debate. Haruta attributed the unique catalytic activity of Au based on three factors: the size of the Au nanoparticles, the selection of the support, and a strong metal–oxide support interaction between Au nanoparticles and the oxide support [8]. Regarding the first point, Haruta showed that for low temperature CO oxidation on three selected metal oxide substrates, the turn-over frequency (TOF) increases with decreasing diameter of Au nanoparticles [9] (see figure 1.1). The TOF starts to increase abruptly when the Au particle diameter is 5 nm, and for the smallest nanoparticles with diameter of 2.5 nm synthesized in ref. [9], the TOF was highest. This pioneering work revealed the size–effect of gold nanoparticles and initiated much research in this field.

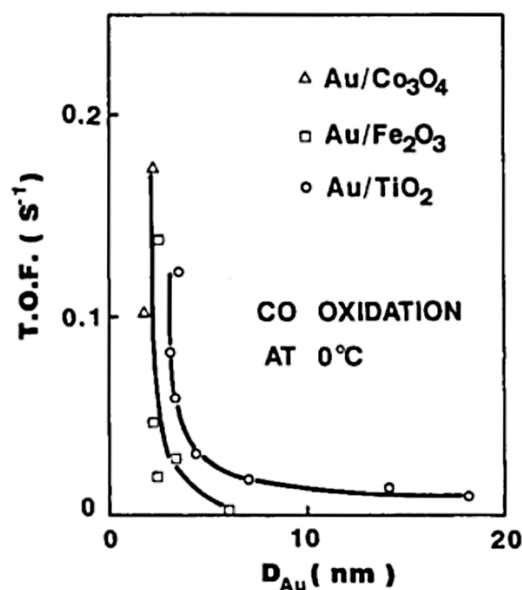


Figure 1.1: TOF for CO oxidation at 273K as a function of mean Au particle diameter on Co_3O_4 , Fe_2O_3 and TiO_2 . Reprinted from ref. [9].

With further decrease of the size of Au nanoparticles, the catalytic activity of gold does not increase indefinitely. It has been shown that on TiO_2 the TOF has a “volcano shape” behavior [4] for the Au nanoparticles with diameter between 1 – 6 nm (see figure 1.2). The maximum activity is reported for nanoparticles with 3 nm diameter [4]. Others, however, argued that the smallest clusters, i.e., ultimately, single adatoms are catalytically most active in specific reactions (see section 1.1.3).

Although there is a widespread controversy about the exact origin of the unique catalytic activity of the small nanoparticles, it is widely accepted that supported nanoparticles play a vital role in heterogeneous catalysis.

1.1.2 Cluster nucleation and sintering

In order to achieve a high yield and selectivity of chemical reactions, the catalytically active nanoparticles have to be monodispersed on a high–surface–area support. The nanoparticles, from now on termed clusters, are often present on special sites of the support material. These

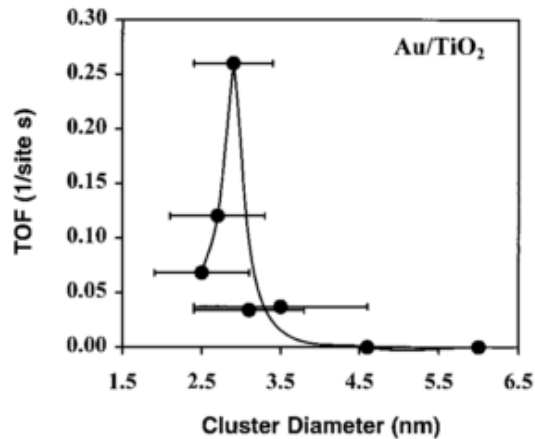


Figure 1.2: TOF for CO oxidation at 300K as a function of mean Au particle diameter on TiO₂. Reprinted from ref. [4]:

typically include oxygen vacancies, domain boundaries, step edges, dopant materials or other types of defects [10, 11, 12]. This site specific nucleation is called heterogeneous nucleation. If there is no specific site for cluster nucleation on the supporting substrate, the nucleation is homogenous.

A major problem in the catalysts using supported nanoparticles is sintering of these nanoparticles. Sintering is defined as a growth of the catalytically active material, which results in the loss of the active sites of the catalysts. The driving force in sintering is the surface free energy of the nanoparticles: with a decreasing size, the surface free energy gradually increases. Large nanoparticles are consequently more favorable than smaller ones.

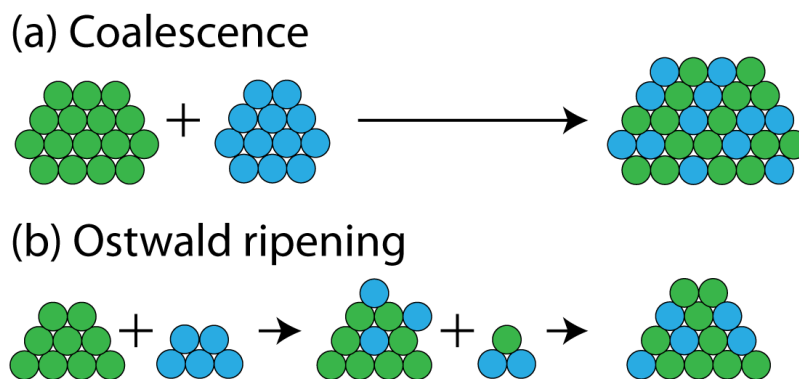


Figure 1.3: Two main mechanisms of cluster sintering: (a) cluster migration and coalescence and, (b) Ostwald ripening.

Two main mechanisms of sintering are traditionally assumed: (a) cluster migration and coalescence, and (b) Ostwald sintering (see figure 1.3). In a case of particle migration and coalescence, clusters diffuse on the surface. When two clusters meet, they merge together. In a case of Ostwald ripening, both small and large clusters continuously evaporate the atoms

they are made from. Since the large clusters are energetically more favorable than the smaller ones, the large clusters are becoming larger over time, while the smaller ones eventually disappear.

Sintering is typically thought to be a thermally driven process. For large clusters, the most common mechanism of sintering is Ostwald ripening [13, 14]. Additionally, it has been recognized early on that the gas composition can also strongly induce the sintering rate [15, 16, 17, 18, 19].

1.1.3 Single atom catalyst

The ultimate small-size limit for supported metal particles are single atoms [2]. Single atom catalysts would provide the ultimate efficiency in the use of metal atoms, and potentially also a high catalytic activity. Recently, a few model systems of single atom catalysts have been discovered. These include Pt_1FeO_x [20], which is found to be capable to oxidize CO. It was proposed that for water-gas shift (WGS) catalysis only non-metallic Au and Pt species (possibly single adatoms) are catalytically active, while the metallic particles are spectators [21]. Pd single atoms trapped at ascending step edges on Cu(111) form a stable Pd-Cu alloy. These can be used for a selective heterogeneous hydrogenation [22]. Furthermore, charged Au and Pt single adatoms have been proposed to be active species in several other catalytic reactions [21].

Unfortunately, no suitable model system for the study of single adatom chemistry under reaction conditions exists. Adatoms on flat surfaces typically agglomerate into clusters well below typical reaction temperatures [1].

In the following chapters of this thesis, we will introduce the reconstructed, $\text{Fe}_3\text{O}_4(001)$ B layer surface. This surface allows stabilization of single adatoms both with high density and a monodisperse distribution. We will show that Au adatoms do not agglomerate on this surface for temperatures as high as 673 K. Consequently, this substrate is potentially a versatile model system to study reactivity of single adatoms under reaction conditions.

2 Iron oxides

Iron is the fourth most abundant element on the Earth. Under ambient conditions, Fe forms several stable oxides and hydroxides [23]. Fe-oxides differ in the concentration, coordination and oxidation states of the Fe interstitials within a close packed oxygen lattice [23]. The three most common forms of iron oxides are shown in figure 2.1.

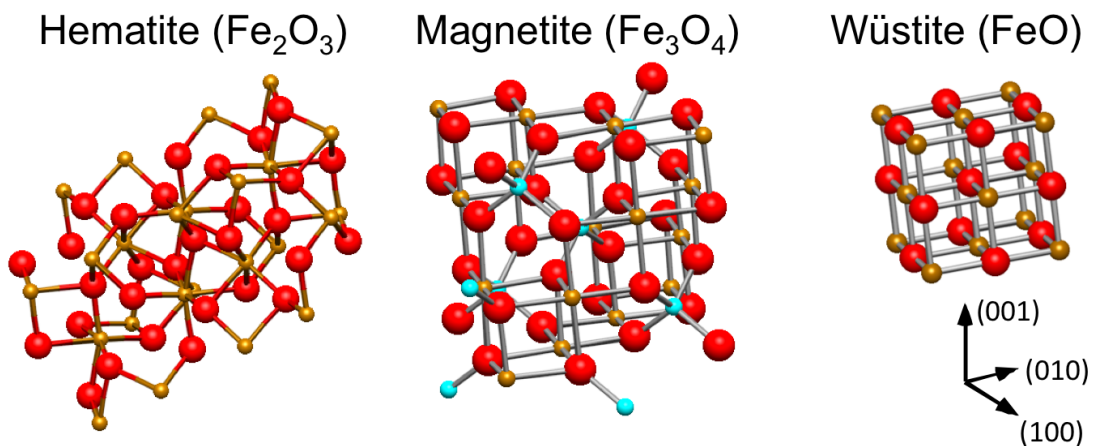


Figure 2.1: Structural models of hematite ($\alpha\text{-Fe}_2\text{O}_3$, left), magnetite (Fe_3O_4 , middle), and wüstite (FeO , right). Oxygen atoms are red, octahedrally-coordinated Fe atoms yellow, and tetrahedrally-coordinated Fe atoms cyan.

Hematite ($\alpha\text{-Fe}_2\text{O}_3$), is the stable oxide phase under highly oxidizing conditions. Hematite has the corundum structure (hcp oxygen lattice with two thirds of octahedrally coordinated sites filled with Fe^{3+}). Hematite is the most common oxide form having the Fe_2O_3 stoichiometry. Maghemite ($\gamma\text{-Fe}_2\text{O}_3$), is a metastable oxide form, having a cubic structure with Fe^{3+} occupying tetrahedral sites. Maghemite can be transformed to hematite at elevated temperatures. Under strongly reducing conditions, wüstite (FeO) is formed, adopting the rocksalt structure with Fe^{2+} filling all octahedral sites. Magnetite, Fe_3O_4 , represents a stable intermediate case.

2.1 Fe₃O₄

Above 125 K, magnetite crystalizes in the inverse spinel structure, described by the formula AB₂O₄. The lattice unit cell is 8.397 Å. It is a mixed valence oxide, with both Fe²⁺ and Fe³⁺ present in the fcc oxygen lattice. Fe³⁺ cations occupy tetrahedral interstitial sites (FeA, blue in the model in figure 2.2a), while a 1:1 mixture of Fe²⁺ and Fe³⁺ is present in octahedrally coordinated FeB sites (yellow in model in figure 2.2a). In the (001) direction, the crystal is built up by A–B stacking of an A layer (FeA) and a B layer (FeB + O). The chemical formula for magnetite at RT is often written as (Fe³⁺)(Fe^{2.5+}, Fe^{2.5+})O₄²⁻. This expresses a significant electron delocalization on the FeB atoms. The delocalization is responsible for a high RT conductivity, rendering all FeB atoms equivalent.

Above 125 K, magnetite is predicted to be a half-metal [24]: it shows metallic properties for one spin orientation, while acting as an insulator for the opposite spin. The mixed valence of magnetite leads to ferrimagnetism. This is caused by the spin coupling of the octahedrally coordinated Fe²⁺ and Fe³⁺, with the spins of tetrahedrally coordinated Fe³⁺ coupled anti-parallel to the former. Fe₃O₄ has a Curie temperature of 858 K.

Magnetite is an industrially important material. Fe₃O₄ is used as a catalyst in the Haber-Bosch process and in the water gas shift reaction [25, 26]. Magnetic iron oxides are often used in magnetic storage media. When magnetite nanoparticles are inserted into arsenic-contaminated water, they act as a sorbent and they clean the water.

On cooling through $T_V = 125$ K, magnetite undergoes the so-called Verwey transition [27, 28]. This first order phase transition is represented by a drop in conductivity by two orders of magnitude, as well as changes in structural and magnetic properties. Originally, the Verwey transition was explained by a long range charge order on the FeB lattice [27]. Although the mechanisms of the Verwey transition are still not fully understood, there is a general agreement about several aspects. The transition takes place only in stoichiometric single crystals. Non-stoichiometry results in lowering of the T_V , or a complete disappearance of the Verwey transition. The symmetry of the bulk unit cell changes from cubic ($T > T_V$) to monoclinic [29, 28]. The magnetic easy axis changes from the $\langle 111 \rangle_{cubic}$ at $T > T_V$ to $\langle 001 \rangle_{monoclinic}$ at $T < T_V$.

2.2 Fe₃O₄(001)

For the 001 surface, there are two possible planes to slice through the bulk A–B stacking sequence. The (001) surface of magnetite can be terminated either by tetrahedrally coordinated FeA atoms (termed A layer), or by octahedrally coordinated FeB and O atoms (B layer). In both cases, the unreconstructed surface unit cell has a lattice constant of 5.94 Å (see dashed square in figure 2.3a). Based on the electrostatic arguments of Tasker [30], both of these two terminations have a non-zero net dipole moment perpendicular to the surface (classified as a Tasker type 3 surface). A substantial surface reconstruction should be expected. Fe₃O₄, however, has a significant conductivity above T_V , and it is not clear that the “polarity catastrophe” [31], typical for insulating materials, would occur in this case.

A $(\sqrt{2} \times \sqrt{2})R45^\circ$ reconstruction¹ is regularly observed experimentally [32, 33, 34, 35]. Pioneering scanning tunneling microscopy (STM) measurements revealed that the (001) surface

¹This reconstruction is also termed $c(2 \times 2)$, when a non-primitive unit cell is used to describe the symmetry.

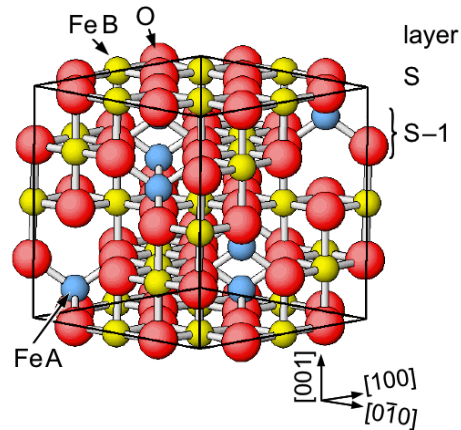


Figure 2.2: Inverse spinel bulk unit cell of Fe_3O_4 . In the (001) direction, planes comprised of tetrahedrally coordinated FeA atoms (A layer) alternate with planes containing FeB atoms and oxygen atoms (B layer).

terminated with octahedrally coordinated Fe atoms [36, 37]. This evidence came from observation of rows of atoms that were changing direction by 90° between two adjacent terraces. The minimal step height observed in refs. [36, 37, 32] was 2.1 \AA , corresponding to the distance between two B layers (or A layers). In the inverse spinel structure, the rows of FeB atoms turn by 90° between two adjacent B layer terraces. This was a clear indication that magnetite is terminated with B layer surface. In contrast, the unreconstructed B layer has a 1×1 symmetry (see dashed square in figure 2.3a). For this reason, a large number of surface terminations were proposed, partly to explain the surface reconstruction, and partially based on compensation arguments. A detailed discussion of these proposed surface terminations is given in chapter 7.

The surface structure of the $\text{Fe}_3\text{O}_4(001)-(\sqrt{2} \times \sqrt{2}) R45^\circ$ reconstruction was solved in 2005 by a combined density functional theory (DFT) and X-ray diffraction study [35]. The lowered symmetry is caused by subtle lateral relaxations of the surface FeB and O atoms (of the order of 0.1 \AA), as shown in figure 2.3a. The alternating, lateral relaxation of pairs of Fe atoms in a direction that is perpendicular to the FeB rows (i.e. along $\langle 110 \rangle$) leads to a wave-like undulation of the FeB rows. According to ref [35], the displacement should be of the order of 0.1 \AA . STM strongly overestimate the wiggling amplitude, however, while for certain imaging conditions, the undulation of the FeB rows can be even suppressed. In STM images of the clean surface, only FeB atoms are imaged. Oxygen atoms do not have any electronic states close to the Fermi energy [24], and are invisible in STM under typical scanning conditions.

This reconstruction creates two non-equivalent sites for FeA bulk continuation sites of the reconstructed surface. Throughout this thesis, we will term these narrow and wide, respectively. The narrow site is located at the bridging oxygen site, where pairs of FeB atoms relax closer to each other. The wide site is located at the same place, but for FeB atoms relaxed apart from each other. The nearest neighbor distance between two narrow sites is 8.39 \AA in the $\langle 100 \rangle$ direction, the second nearest neighbor distance is 11.88 \AA in the $\langle 110 \rangle$ direction. In figure 2.3a, we also highlight two positions within the narrow site, at the place of two octahedral, hollow

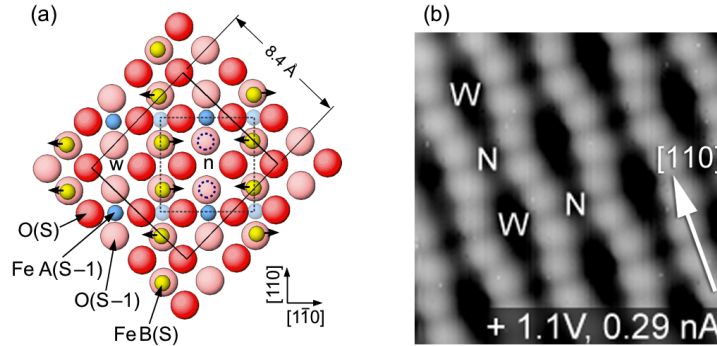


Figure 2.3: A model of the reconstructed B layer surface. Top view of the distorted B layer termination of the $\text{Fe}_3\text{O}_4(001)$, as determined by DFT+U calculations [35]. In plane relaxation of the surface FeB and O atoms, perpendicular to the FeB (S) row direction, lead to a $(\sqrt{2} \times \sqrt{2}) R45^\circ$ symmetry. The black, dashed square represents a primitive cell of an unreconstructed surface. The square drawn with a full line highlights one reconstructed unit cell ($a = 8.4 \text{ \AA}$). Due to the reconstruction, the two bulk continuation FeA sites are inequivalent. We label them narrow (n) and wide (w), respectively. (b) STM image of a defect free B layer surface. Undulating rows of FeB atoms are observed along $[110]$ direction. The position of narrow and wide site are highlighted in the image.

sites (broken blue circles). These sites will be of importance in chapter 7.

For the B layer termination, all atoms in the surface FeB (S) and subsurface FeA (S - 1) layer are Fe^{3+} [38, 39]. Later ab-initio calculations revealed that the subsurface FeB (S - 1) layer contains alternating pairs of Fe^{2+} and Fe^{3+} cations, ordered with the $(\sqrt{2} \times \sqrt{2}) R45^\circ$ symmetry [40, 41]. Underneath the narrow site is a pair of Fe^{2+} (S - 1), and below the wide site is a pair of Fe^{3+} (S - 1) cations. The charge ordering in the sub-surface layers leads to a half-metal to insulation transition in the surface, opening a band gap of $\sim 0.3 \text{ eV}$ [40]. The presence of a surface band gap value (0.2 eV) was also measured experimentally by scanning tunneling spectroscopy [42].

3 Experimental techniques

3.1 Scanning tunneling microscopy (STM)

The main experimental technique used in this thesis is scanning tunneling microscopy (STM). Developed in 1982 [43, 44], this microscope has become an important tool for a real space analysis of metals and semiconductors at the atomic level. The principle of the microscope is based on a quantum mechanical electron tunneling through a controllable vacuum gap. In practice, this is realized by approaching a sharp metal tip to close proximity (a few Å) of a conducting sample. The basic principle of vacuum tunneling process can be described by a time-separated 1D Schrödinger equation with a rectangular potential given by $\phi = V - E$:

$$\left(-\frac{\hbar^2}{2m}\Delta + V\right)\psi(z) = E\psi(z), \quad (3.1)$$

where V is the potential barrier height, ψ is the wave function, and E is the electron energy. The solution of equation 3.1 is an exponentially decreasing wave function:

$$\psi(z) \propto \exp\left(-2d\sqrt{\frac{2m\phi}{\hbar^2}}\right). \quad (3.2)$$

The tunneling current is proportional to the transmission probability T :

$$T \propto |\psi(z)|^2. \quad (3.3)$$

Equation 3.3 shows that electron tunneling depends exponentially on the sample-tip distance. The tunneling current also depends on the local density of states around the Fermi level of the tip/sample, and the applied voltage. This is illustrated in image 3.1, where, in case of a positive sample bias (a), the electrons tunnel from the tip into empty states of the sample. When the sample is negatively biased (b), electrons tunnel from the filled states of the sample into the STM tip.

The scheme of the microscope is shown in figure 3.2. The STM microscope is typically operated in the constant current mode. This is achieved via a feedback loop that changes the distance between the sample and the STM tip. In each cycle of the feedback loop, the measured value of tunneling value is compared with a set value. The difference is processed by a differential am-

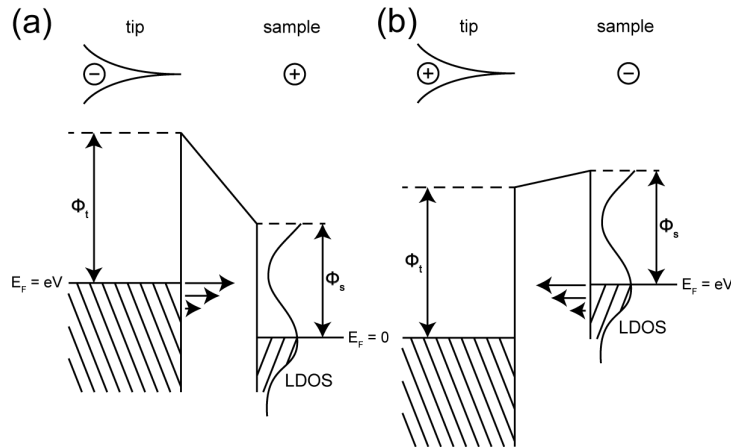


Figure 3.1: Schematics of electron tunneling in STM for a case of (a) positive sample bias and (b) negative sample bias.

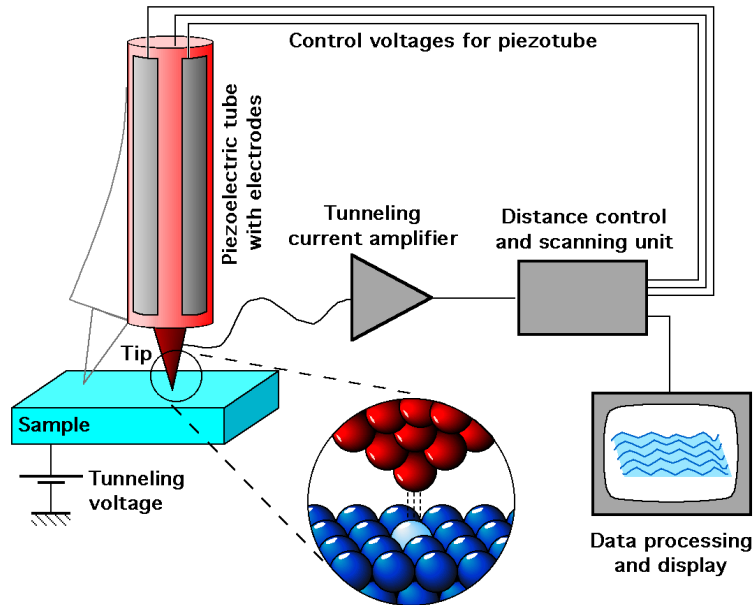


Figure 3.2: Schematic view of an scanning tunneling microscope. Reprinted with permission from ref [45].

plifier, and multiplied by a gain value. A high gain value can cause a feedback loop oscillations. On the contrary, a very low gain can cause a slow response of the tip to the surface topography, with the possibility of a tip crash. The output value from the amplifier then drives the change in the tip distance (z -piezovoltage). This feedback loop cycle is repeated with a high frequency, in order to ensure a constant tunneling current. The value of the z -piezovoltage is recorded for a grid of points on a 2D area on the surface.

It is important to note that STM does not measure the real position of atoms, but the local density of electronic states. A more detailed description of STM can be found in ref. [46].

3.2 X-ray photoelectron spectroscopy (XPS)

X-ray photoelectron spectroscopy (XPS) is a quantitative technique that measures elemental composition, chemical state and electronic states within the surface region of probed sample. XPS measures the binding energy (E_B) of each electron emitted due to the photoelectric effect, according to the formula:

$$E_B = h\nu - E_K - \phi, \quad (3.4)$$

where $h\nu$ is the energy of incident photons, E_K is the kinetic energy of the emitted electrons, and ϕ is a work function of the detector. A dual source (Al, Mg) X-ray $K\alpha$, combined with a hemispherical electron analyzer is used in an XPS setup. This source provides photons with an energy high enough to remove electrons from core levels. The measured E_B of the core levels depends on the chemical environment, while the intensity of the core level peak is proportional to the concentration of the element in the sample and its depth. When photoelectrons emitted normal to the sample's surface are detected, XPS has probing a depth of $\sim 3\lambda$. Detection of the photoelectrons at a grazing angle makes XPS more surface-sensitive. A detailed description of the XPS technique can be found in ref. [47].

3.3 Low energy ion scattering (LEIS)

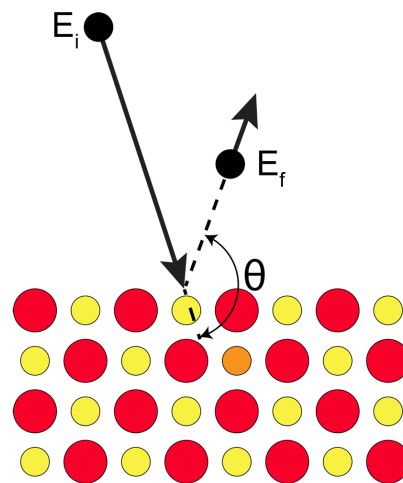


Figure 3.3: LEIS: schematic model of interaction of an noble gas ions with the surface. Low energy ions (black) interact with the surface. If the ions are scattered from the surface with a scattering angle θ pointing to the electron analyzer, they are detected. Rare gas ions penetrating the first layer have a very low probability to return as an ion through the first layer.

Low energy ion scattering (LEIS) is a surface science technique sensitive to the outermost surface layer only. LEIS uses a beam of noble rare gas ions, typically He^+ , directed onto the sample surface. Ions scattered from the surface to the hemispherical energy analyzer are measured. These ions have a scattering angle θ (see figure 3.3). In LEIS, the incident ions have energy (E_i) in the range between 0.5 – 5 keV. For these energies, the interaction of ions

with surface atoms can be described in terms of classical mechanics as a collision of two hard spheres. Using the conservation of energy and of momentum, a formula of the outgoing ions energy can be derived, as shown in equation 3.5:

$$E_f = \left[\frac{\cos\theta + \sqrt{R^2 - \sin^2\theta}}{1 + R} \right] E_i, \quad (3.5)$$

where θ is a scattering angle, $R = M_{atom}/M_{ion}$ is the mass ratio between the atom on the surface and the mass of the incident ion. Values of E_i , θ and M_{ion} are usually known. From measurement of E_f , the composition of the surface (M_{atom}) can be determined easily. The extreme sensitivity to the surface layer is due to the very high neutralization probability of rare gas ions. As a consequence, ions penetrating to the deeper layers are not detected. More details about the LEIS technique, including the capability of LEIS to determine the structure of the surface, can be found in reference [48].

3.4 Molecular beam epitaxy (MBE)

Molecular beam epitaxy (MBE) is a method to grow single crystalline films. MBE utilizes the principle of molecular effusion, and should be always operated under UHV vacuum. Compared to other deposition methods, the combination of UHV and the absence of a carrier gas results in a very high purity of the grown films. MBE allows deposition of charge-neutral material, with coverages ranging from sub-monolayer to continuous films.

The main concept of MBE is the heating of a deposited material to a temperature where it starts to sublime. Heating can be done indirectly, when the deposited material is placed in a Knudsen effusion cell, or directly by bombarding the solid material with electrons. The calibration of the deposition rate is typically done prior to metal deposition by a quartz crystal monitor (QCM). During the deposition, the growth can be directly monitored by reflection high energy electron diffraction (RHEED) [49].

3.5 Experimental setups

Several UHV systems were used throughout the work done in this thesis. A brief description is included in this section, employing the components mentioned above.

3.5.1 RT STM system

The Room Temperature Scanning Tunneling Microscope (RT STM) is a UHV setup that consists of two connected chambers, a preparation chamber and an analysis chamber, with a base pressure below 1×10^{-10} mbar and 5×10^{-11} mbar, respectively. The UHV in the preparation chamber is maintained via an ion pump and a turbomolecular pumped backed by a rotary vane pre-vacuum pump. The analysis chamber is pumped by an ion pump and an LN₂ cooled titanium sublimation pump (TSP) pump. The pressure in the preparation chamber is measured with a Penning gauge, in the analysis chamber with a Bayard-Alpert ion gauge, and the pre-vacuum pressure with a Pirani gauge.

The preparation chamber is equipped with an Ar⁺ ion source (VG EX05 with an additional scanning unit) for sample cleaning, an electron beam heating stage for sample annealing and a QMS (Hiden HAL) for residual gas analysis. Materials can be evaporated with LN₂ cooled electron beam evaporators (up to three single or triple Omicron EFM3). Deposition rate is calibrated with a water-cooled quartz crystal microbalance (QCM).

The analysis chamber contains a customized commercial STM (Omicron μ -STM) operated (mostly) in constant current mode with electrochemically etched W tips, AES (Perkin Elmer), LEED (SPECS Er LEED, 2 grid), XPS (dual anode X-ray source VG XR3E2, differentially pumped with an additional ion pump and SPECS EA10+ electron analyzer), LEIS (VG AG-6 ion source and SPECS EA10+ electron analyzer), and QMS (Balzers QMG 125).

Samples mounted on an Omicron sample plate can be introduced into the preparation chamber without breaking the vacuum via a loadlock (initially pumped down with a rotary pump, then with a LN₂ cooled cryogenic pump). Sample transfer between the preparation and analysis chamber, which are separated by a UHV gate valve, is done with a magnetically coupled transfer rod. Within the analysis chamber the sample is transferred with a wobble stick. Gases can be introduced into both chambers via a high precision UHV leak valves.

A more detailed description of this system, including a schematic diagram, can be found elsewhere [50].

3.5.2 SPECS system

The SPECS UHV setup is optimized for the MBE growth of thin films. The system consists of separate preparation, analysis and load lock chambers, with base pressures of 1×10^{-10} mbar, 5×10^{-11} mbar, and 1×10^{-9} mbar, respectively. The pressure in each chamber is measured with a Bayard–Alpert ion gauge; pre-vacuum pressure with a thermocouple (TC) gauge. Each chamber is pumped with a turbomolecular pump backed by a scroll pump. The preparation and analysis chambers also contain an ion pump with a built-in TSP pump.

Both, preparation and analysis chamber contain a manipulator with an electron-beam heating stage and a QMS (SRS RGA 100). Samples mounted on SPECS sample plates are transferred between the chambers via a magnetically coupled transfer rod. Gases can be introduced to both chambers via a high precision UHV leak valves.

The preparation chamber includes an ion source (SPECS IQE 11/35). The chamber is suited to house evaporators of various types. The growth of thin films can be monitored with reflection high energy electron diffraction (RHEED) or with an custom built QCM.

The analysis chamber allows sample analysis with STM (Aarhus 150 Rel.1), low primary beam current LEED (Omicron MCP1), and XPS (X-ray source Omicron DAR 400 with electron analyzer SPECS Phoibos 100).

3.5.3 PINUP system

The UHV system “PINUP” consists of a μ -metal chamber with a sample manipulator with heating and cooling (50 - 1000 K). The vacuum is established via a turbololecular pump and a TSP pump. The pressure is read with a Bayard–Alpert ion gauge. The base pressure of this vacuum system is below 5×10^{-11} mbar.

Chapter 3. Experimental techniques

This system contains two ion sources: Leybold Heraeus for Ar⁺ sputtering, and SPECS IQE 12/38 for LEIS measurements. A small rotatable hemispherical analyzer allows different scattering geometries during LEIS measurements. The chamber is equipped with an ErLEED 1000-D unit, suitable for LEED I-V measurements, AES (Perkin-Elmer), and QMS (Pfeiffer PrismaPlus). A SMOKE setup, capable of measurement of both in-plane and out-of-plane magnetism, is located in the bottom level of the chamber. Atmospheric-side coils with yokes reaching into the vacuum chamber produce a maximum magnetic field of 100 mT in the 3 cm gap. Kerr rotation and ellipticity of a He-Ne laser beam reflected from the sample are measured with a modulation technique, using a photoelastic modulator.

4 Experimental details

4.1 Samples

All published work done in this PhD thesis [51, 52, 53, 39, 54, 55] utilized a synthetic $\text{Fe}_3\text{O}_4(001)$ single crystal, internally labeled as No. 357. This crystal was grown via the floating zone method by Prof. Mao and co-workers at Tulane University, New Orleans, USA. The as-received single crystal bar showed a sharp Verwey transition at 121 K upon cooling, as shown in figure 4.1b. The (001) crystal was oriented, cut and polished by MaTeck GmbH (orientation accuracy $< 0.1^\circ$). The $\text{Fe}_3\text{O}_4(001)357$ crystal has a round shape (approx. 5 mm diameter, 1 mm thick) and is shown, mounted on a molybdenum sample plate, in figure 4.1a.

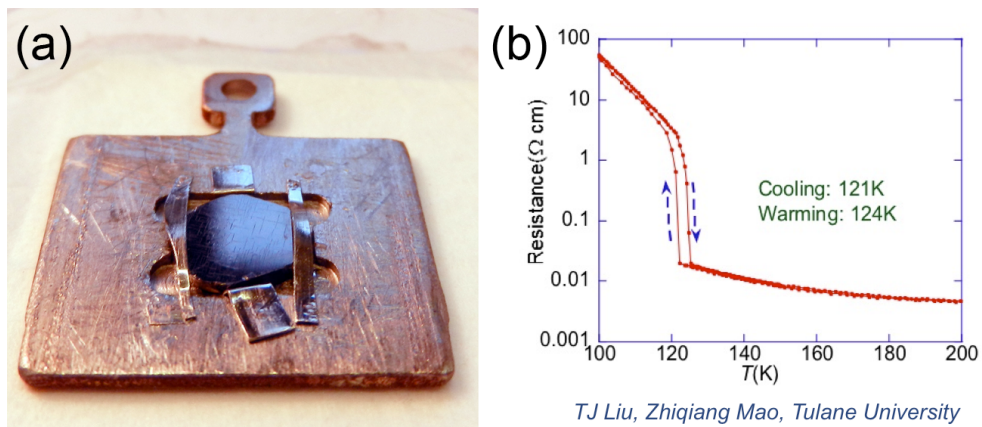


Figure 4.1: (a) The $\text{Fe}_3\text{O}_4(001)357$ synthetic single crystal mounted with Ta clips on a Mo sample plate. (b) The temperature-dependent resistance measured on the as grown single crystalline bar by T. J. Liu and Prof. Mao at Tulane university, New Orleans, USA. Note the sharp Verwey transition at 121 K.

Initially, this synthetic single crystal (SSC) contained no visually observable defects. After two years of repeated sputtering, annealing, and re-oxidation, the morphology of the surface changed significantly, as is shown in figure 4.2. In part (a), a large scale image of the mounted sample is shown. The zoom-in inset shows that the surface is rough and contains a large number of line defects. During a collaboration with Juan de la Figuera in 2012, high resolution

optical microscope images of the crystal were acquired. They revealed that the roughness is caused by a large number of pyramids, as shown in figure 4.2b. The line defects are hematite (Fe_2O_3), as determined by local Raman spectroscopy. Both the pyramids and hematite defects are a consequence of crystal exposure to O_2 at temperatures above 450° [56]. Small areas of flat surface were present in the proximity of the hematite inclusions (dark areas in the inset of figure 4.2a). In November 2012, the sample was sent to MaTeck GmbH for re-polishing (with an orientation accuracy $< 0.1^\circ$). Scanning electron microscope (SEM) images acquired afterwards showed that a flat surface was restored (see figure 4.2d,e). At the same time, a search for a new high-quality sample was initiated. A complete list of all the samples is included in appendix B. Several selected samples (both natural single crystals and synthetic single crystals) are studied in more detail in appendix B.1.

4.2 Sample mount for UHV experiments

Samples were always mounted on sample plates from molybdenum (Specs or Omicron design, depending on the UHV system used). The single crystals were fixed to the sample plate using tantalum clips. Starting from experiments with Au and Pd deposition, a thin Au sheet was placed between the back side of the sample and the sample plate in order to improve the thermal contact. The materials used for sample mount were cleaned in an ultrasonic bath cleaner using acetone and ultra-pure isopropanol in the last cleaning cycle. The remaining fragments of these organic solvents were removed by blowing with CO_2 .

4.3 Sample preparation

The typical sample preparation used in this thesis was determined for a stoichiometric synthetic single crystal. Using natural single crystals and epitaxially grown thin films often poses experimental difficulties caused by impurities, non-stoichiometry and, in case of thin films, the possibility of charging effects, because the commonly used substrate for (001) magnetite film growth, $\text{MgO}(001)$, is an insulator. These issues are discussed in depth in section B.1. The following recipe applies to the $\text{Fe}_3\text{O}_4(001)$ sample No. 357. The sample preparation consists of:

1. Sputtering using Ar^+ ions accelerated to 1 keV. Typical sputter dose is 15 minutes with an ion current of $1 \mu\text{A}$ (measured on the sample).
2. Annealing in UHV at (873 – 923) K for 15 minutes.
3. Annealing in O_2 ($p = 2 \times 10^{-6}$ mbar) at (873 – 923) K for 45 minutes.
4. Annealing in UHV at (873 – 923) K for 5 minutes (while the O_2 is pumped down).
5. Flash-annealing in UHV at (873 – 923) K.

Steps 1 – 4 are done in a sequence, and henceforth will be termed as one sample preparation cycle. When the sample is introduced to the UHV from air, or after metal deposition, several sample preparation cycles are necessary (typically 6 cycles) to restore the pristine surface.

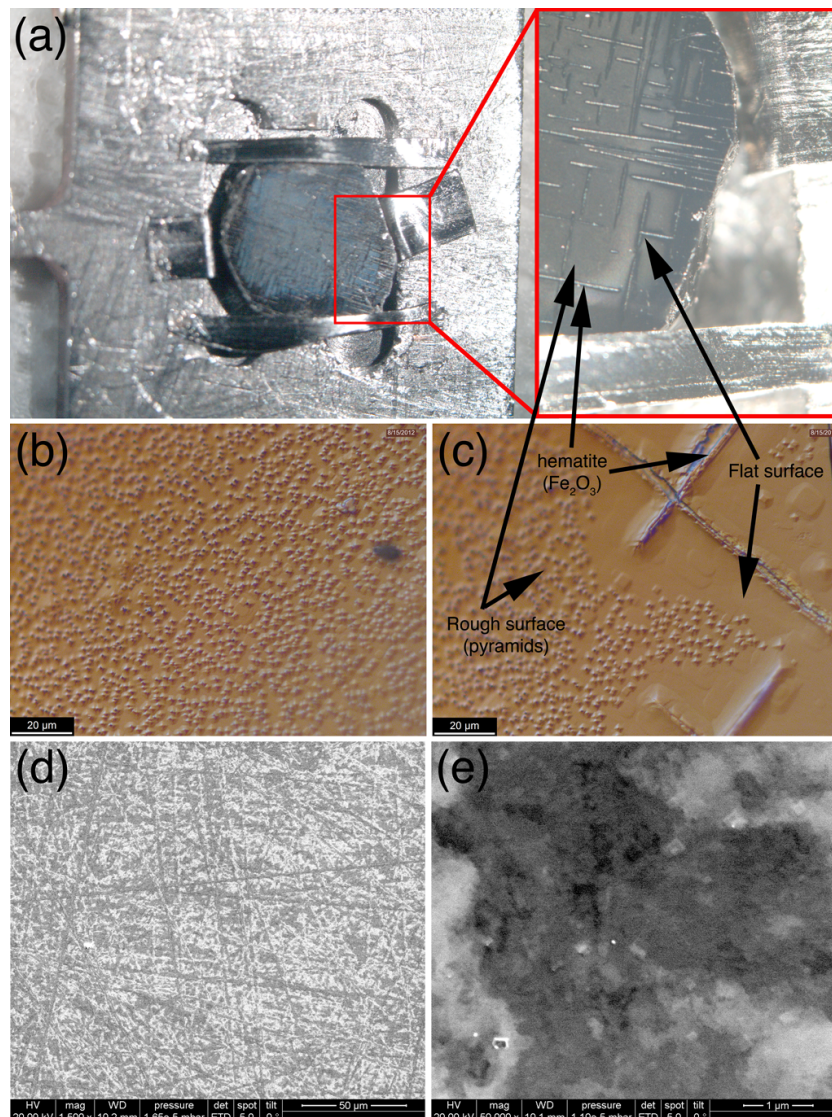


Figure 4.2: Degradation of the $\text{Fe}_3\text{O}_4(001)357$ crystal after two year's use. Figure (a) shows an optical image of the SSC No. 357. The inset shows that most of the surface area is rough. It also contains line defects. Areas in the vicinity of the line defects are flat and reflective. The roughness is caused by small pyramids present on the surface, as is shown in a high resolution optical image in part (b). The line defects were identified as hematite inclusions [56], the dark areas of the crystal next to line defects is flat Fe_3O_4 surface. Images (b,c) were acquired and analyzed by Juan de la Figuera and Kevin F. McCarty, and are reprinted with the permission of the authors. (d) and (e) shows SEM images obtained directly after the sample was re-polished. In the large scale image (d), macroscopically rough areas, caused by the polishing process, can be identified. The zoom in image shows that the pyramids had been removed from the surface. Images acquired by Michael Stoeger-Pollach, USTEM, TU Wien using an FEI Quanta 200 FEGSEM microscope.

In this case the clean surface can be obtained by skipping the re-oxidation in several cycles and the clean surface is usually obtained by using steps in a following order: 1,2,3,4; 1,2; 1,2; 1,2,3,4; 1,2; 1,2,3,4.

As a consequence of annealing in O₂, the base pressure in the preparation chamber gets worse by ~one order of magnitude. We left the sample in the analysis chamber until the pressure in the preparation chamber reached the base pressure value. Then, we typically flash-annealed the sample (step 5 in the list shown above), which yields an almost defect-free and adsorbate-free surface.

For sputtering, an Ar⁺ ion energy of 1 keV was found to be an optimum value. Using energies above 1.5 keV is not recommended, because the preferential sputtering of oxygen over iron will increase. This will then result in a significantly reduced near-surface region. The sputtering dose should not deviate much from the mentioned value (15 minutes with an ion current of 1 μA). If the ion current is larger (lower), the sputtering time has to be adapted in order to bombard the surface with the same ion dose. When a sputter gun with a scanning unit was used (all systems except SPECS), the sputtering beam was always optimized with an oscilloscope operated in the x-y mode, where the two channels are reading beam deflection and the intensity is controlled by an ion current, which is adjusted using a current amplifier.

For annealing, the biggest challenge is the accurate temperature reading. All UHV systems used in the group employ an indirect temperature measurement. The measurement is typically done via a type K thermocouple (valid for all UHV systems except PINUP, which employs a type N thermocouple) spot-welded to a spring holding the sample plate inside the manipulator. Therefore, the temperature is measured not directly on the sample and the optimum value is system-specific. Typically an exact temperature reading is not a crucial factor for the success of the experiment. It was critical, however, for the study of H₂O desorption, done in the SPECS system. Here, the correct temperature was obtained by via a calibrated IR pyrometer. For a temperature estimate during sample preparation, the value was obtained with the help of STM, looking at the size of terraces. When the thermal stability of single Au adatoms was investigated (will be described in chapter 8), a very slow temperature ramp was used, in order to allow the system to reach equilibrium conditions.

For annealing in O₂, a pressure of $p = 2 \times 10^{-6}$ mbar was used. However, we found that even a lower oxygen backpressure (down to $p = 5 \times 10^{-7}$ mbar) allows a reproducible preparation of a clean, reconstructed surface over an extended period of time.

4.4 Evaporation materials

Iron (99.99+% purity, MaTeck GmbH) was deposited in the SPECS UHV system from 2 mm rod with a water-cooled electron beam evaporator (single Omicron EFM3 and OS-Vap-4). The pressure during deposition was in the low 10⁻⁸ mbar range.

Gold (99.99% purity, Oegussa GmbH) was deposited in the RT STM UHV system from a Mo crucible with an LN₂ cooled electron beam evaporator (single Omicron EFM3). Typical parameters used for Au deposition were: filament current $I_f = 1.89$ A, emission current $I_{em} = 13.9$ mA, flux current $I_f = 84$ nA, deposition rate 1 ML per ~70 s. The orifice electrode of the evaporator was positively biased during deposition. The pressure during deposition in the low 10⁻¹⁰ mbar range.

Palladium (99.99+% purity, MaTeck GmbH) was deposited in the RT STM UHV system from

a twisted 1 mm thick rod with an LN₂ cooled electron beam evaporator (triple Omicron EFM3). Typical parameters used for Pd deposition were: filament current $I_f = 1.95$ A, emission current $I_{em} = 5.8$ mA, flux current $I_f = 6$ nA, deposition rate 1 ML per ~ 100 s. The orifice electrode of the evaporator was positively biased during deposition. The pressure during deposition was in the low 10^{-10} mbar range.

4.5 Liquids and gases

The purity of all liquids and gases was checked with QMS. The dosing in the UHV vacuum system was done through high precision leak valves. H₂O (deionized), D₂O (99.9 atom % D, Aldrich), H₂¹⁸O (98 atom % ¹⁸O, Aldrich) was further purified using usually 4–5 freeze–pump–thaw cycles. The pumping was always done with a turbomolecular pump. The chemicals were inserted into a clean glass to metal adapter (typically MDC Stainless steel to 7740 Pyrex–UHV Series) and this adapter was always connected to an all–metal valve (Swagelok), in order to allow transport of the chemicals between UHV systems. The following gases were used: O₂ (99.999%), CO (99.997%), Ar (99.999%) and He (99.999%). The purity was regularly checked with QMS.

4.6 Analysis of experimental data

STM images were analyzed using the ImageJ software package, together with specialized plug–ins developed by Michel Schmid. A typical STM image processing includes background subtraction, removal of the non–linear distortion, noise removal from the fast Fourier transform (FFT) spectrum and adjustment of brightness and contrast. For several features described later, their apparent height in STM is mentioned. This value is always measured with respect to the average height of the neighboring FeB atoms, at a bias voltage of +1 V.

4.7 Definitions

Room temperature (RT) denotes a temperature in the range (297 – 303) K. In this thesis, the coverage unit (1 ML) is defined as one extra atom per reconstructed ($\sqrt{2} \times \sqrt{2}$) R45° surface unit cell. This corresponds to 1.42×10^{14} atoms/cm².

5 $\text{Fe}_3\text{O}_4(001)$ B layer: Adsorption of simple molecules

The ideal, defect-free, reconstructed $\text{Fe}_3\text{O}_4(001)-(\sqrt{2} \times \sqrt{2}) R45^\circ$ surface was described in section 2.2. We studied the $\text{Fe}_3\text{O}_4(001)$ surface under UHV conditions. Even in a very good vacuum, a mixture of gases (H_2 , H_2O , CO , CO_2) is present. Understanding the reactivity of the surface with these simple molecules provides a basis for a better understanding of the origin of the typical surface defects, identification of active sites and chemical processes on the surface.

We found experimentally that the reconstructed B layer surface is inert against adsorption of H_2 , O_2 , CO and CO_2 for pressures up to 10^{-6} at RT. On the other hand, it is possible to adsorb atomic hydrogen and dissociate water molecules (H_2O and D_2O) at RT.

5.1 Adsorption of atomic H

The experiments involving adsorption of atomic H at RT were performed by G. S. Parkinson and co-workers, and published in ref. [34]. Although the author of this thesis was not involved in this work, the results are relevant for the following sections, and will therefore be shortly summarized.

In ref. [34], the clean, reconstructed $\text{Fe}_3\text{O}_4(001)$ surface was exposed to atomic H. H_2 was cracked to atomic H by a hot tungsten filament, positioned in line of sight with, and close to the sample. After 3 minutes of exposure to atomic H (H_2 pressure of 10^{-7} mbar), 0.035 ML of bright double protrusions (see figure 5.1a) appeared atop of the surface FeB rows. Using DFT+U calculations, the authors of ref. [34] found that H is preferentially bound to the O atom within the narrow site (see structural model in figures 2.2 and 5.1). The adsorbed H is strongly displaced from the atop position (see structural model in figure 5.1 and) and the OH group is nearly parallel to the surface, irrespective of the OH coverage. STM does not directly image surface OH (white in the model in figure 5.1), but their presence leads to a modification of the DOS of the two neighboring FeB atoms (orange in the model in figure 5.1). These are reduced to the +2 charge state and appear as a bright double protrusion in STM.

In STM movies, it was frequently observed that the H hops between two symmetrically equivalent oxygen atoms within the narrow site at RT. This is indicated in two consecutive STM images in figures 5.1a and b, where the hopping of the H causes the FeB atoms on the opposite row to become bright.

The authors of ref. [34] found that, after the surface is saturated with OH, it undergoes a semi-

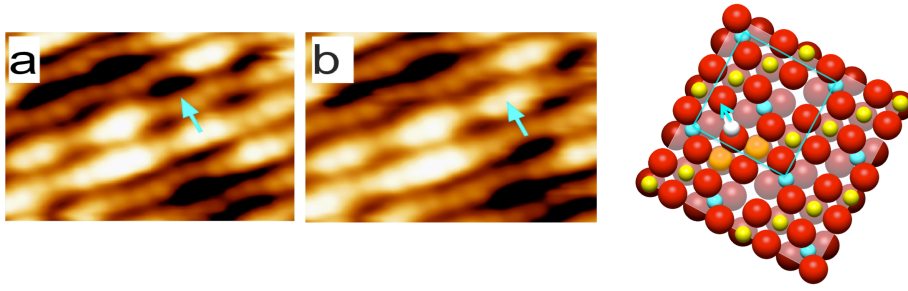


Figure 5.1: STM images of a clean reconstructed B layer following a dose of atomic H (3 minutes at H₂ pressure of 10⁻⁷ mbar; OH coverage = 0.035 ML). The H is imaged indirectly as a bright double protrusion atop the FeB atoms. Between frame (a) and (b), H hops between two oxygens atoms within the narrow adsorption site, as indicated by an arrow. The schematic model (right) shows an adsorbed H (white). The two neighboring FeB atoms (orange in the model) are influenced by this surface OH. Scanning details: (4.8 × 3.2) nm², V_s = +1.4 V, I_t = 0.14 nA. Image reprinted from ref. [34] with permission of the authors.

conductor to half-metal transition, linked to changes in the local geometric structure, and an enrichment with Fe²⁺ cations at the surface.

5.2 Adsorption of H₂O and D₂O

Water reaction with oxide surfaces plays an important role in heterogeneous catalysis, electrochemistry, corrosion processes, and environmental science. On oxide surfaces, water adsorption can be molecular or dissociative [10]. In case of water dissociation, surface oxygen vacancies (V_O) and other defects play an important role. The adsorption of water on the Fe₃O₄(001) B layer surface was theoretically studied by DFT+U calculations [38, 57]. It was predicted that, in the presence of V_O's, water adsorbs dissociatively according to equation 5.1:



where O_W denotes the oxygen atom belonging to the water molecule, and O_S is the surface oxygen atom. In equation 5.1, a water molecule (H_2O_W) dissociates on an V_O . Oxygen from the water (O_W) fills the V_O . This results in a transformation of O_W to O_S .

Dissociation of a water molecule in the absence of V_O results in one surface $O_S H$ group and one $O_W H$ group. In the latter case, the surface hydroxyl contains an oxygen atom that is not embedded into the surface lattice. This is described by equation 5.2:



The desorption of D₂O from the Fe₃O₄/MgO(001) was studied previously by temperature programmed desorption (TPD) [58]. D₂O was adsorbed at 110 K. During the temperature ramp (2 K/s up to 710 K), mass 4 (D₂) and mass 20 (D₂O) was monitored with QMS. While no appreciable desorption of D₂ was observed, the D₂O desorption spectra (replotted in figure 5.2) show a variety of peaks. The peaks located at 320, 280 and 225 K were identified as chemisorbed water from the first monolayer at various sites on the surface. The desorption

peak located at 520 K was not assigned to any specific desorption process in ref. [58].

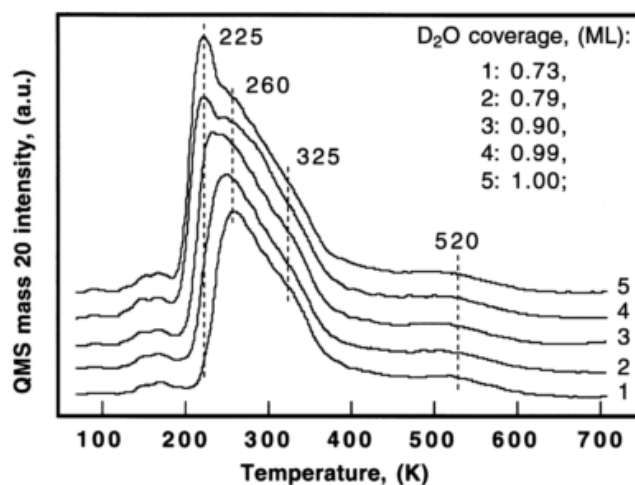


Figure 5.2: TPD spectrum of a water desorption from a Fe₃O₄/MgO(001). Image reprinted from ref. [58].

In this section, we will show that exposure of a clean, reconstructed B layer surface to water (for pressure below 10^{-5}) results only in a low coverage of surface O_SH (i.e. adsorption of H on the O sublattice, as described previously in section 5.1). We will identify the wide desorption peak located at 520 K in figure 5.2 as a result of desorption of water through the abstraction of lattice O_S atoms (Mars–van–Krevelen mechanism).

5.2.1 Results

Water adsorption was performed at RT. Since RT lies in the middle of a desorption peak (see figure 5.2), the dosing was done while the sample was inserted in the STM block of the Aarhus STM, providing a large thermal sink. The sample was facing upwards (i.e. the opposite to the STM tip) and the temperature of the sample was measured with a diode built–in into the STM block. This approach allowed a good reproducibility of the experiments. All STM images shown in this section were done using purified H₂O (see section 4.5). The key experiments of this chapter were repeated with D₂O with the same results.

In figure 5.3 we show the clean B layer surface following the adsorption of water with nominal exposures ranging from 0.045 L to 90 L. Adsorption of water results in an increase in the number of double protrusions, previously identified as surface OH groups (see section 5.1). The identification of OH group is done unambiguously; the characteristic hopping of the bright double protrusions between the FeB rows within the narrow site was regularly observed in STM movies. For very low water exposures (0.045 L and 0.45 L), surface OH's were always observed in pairs. This is due to a water dissociation at surface oxygen vacancies (V_O 's) according to equation 5.2. With increasing water dose, isolated OH groups start to appear. At 90 L, saturation of OH was reached. All LEED images acquired after water exposure still exhibited a $(\sqrt{2} \times \sqrt{2})R45^\circ$ symmetry. This is consistent with a single H adsorption in narrow sites.

The density of surface OH as a function of dose at RT is plotted in figure 5.3. In this figure,

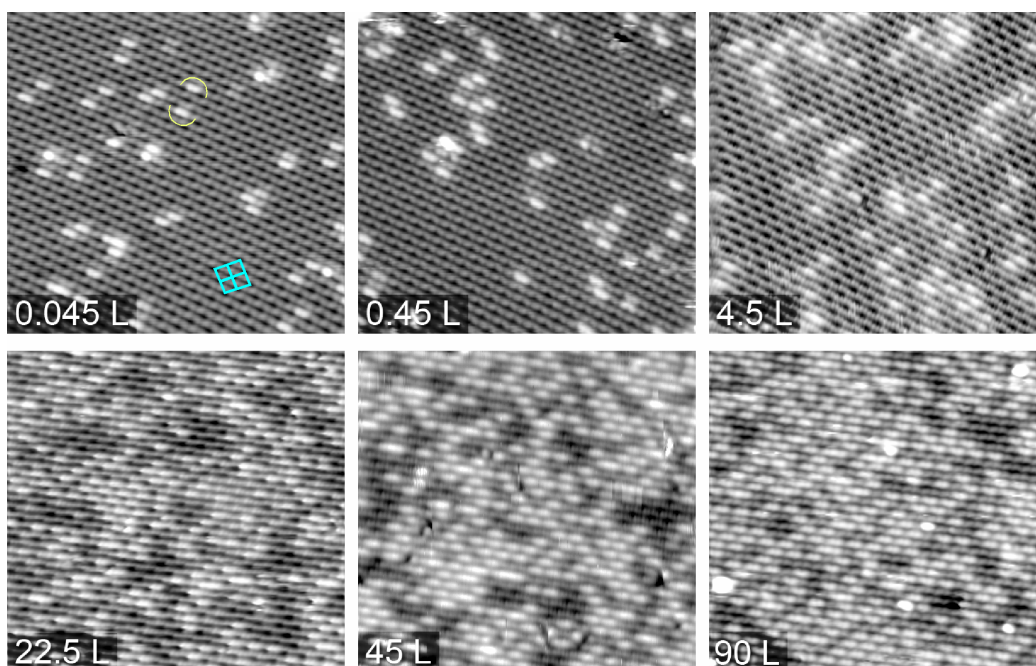


Figure 5.3: Different coverages of water adsorbed onto a clean B layer surface at RT. The water dose (0.045 – 90) L is indicated in the left bottom corner of each image. Scanning details: $(20 \times 19) \text{ nm}^2$, $V_s = +(0.9 - 1.2) \text{ V}$, $I_t = (0.28 - 0.34) \text{ nA}$.

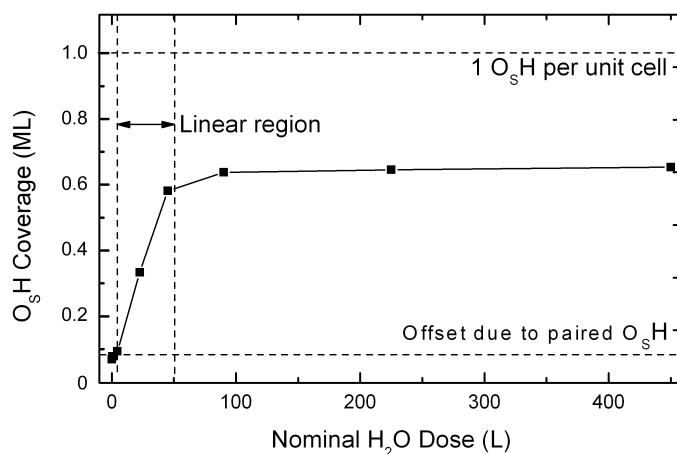


Figure 5.4: Density of the surface OH groups observed in STM images versus the nominal water coverage.

an offset of 0.08 ML is marked. This offset is caused by the paired OH groups, formed by dissociation of water at V_O 's. After the onset of isolated OH adsorption, the increase in coverage is linear until a dose of ~ 50 L is reached.

STM images showed no evidence of the presence of O_WH groups during dissociation in the absence of V_O 's, as would be expected on the basis of equation 5.1. To identify whether the O_WH

species are present on the surface, we used low energy ion spectroscopy (LEIS), together with isotopically labeled water (H₂¹⁸O). As mentioned in section 3.3, LEIS is a very surface-sensitive technique when low energy He⁺ ions are used. The use of isotopically labeled water allows easy identification of O_S (mass 16) and O_W (mass 18).

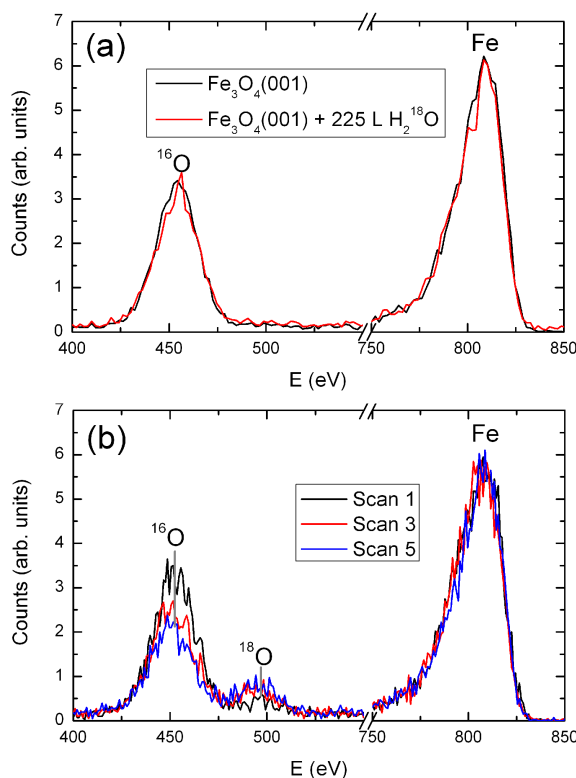


Figure 5.5: LEIS spectra on a clean and a water-dosed surface. (a) LEIS spectra on clean surface (black) and after dosing of 225 L of H₂¹⁸O at RT (red), with no water in the background. (b) Consecutive LEIS scans on the clean B layer surface in a H₂¹⁸O background pressure of 1×10^{-8} mbar at RT. All measurements done with 1 keV He⁺, scattering angle = 120°.

Initially, the LEIS experiments were not conclusive: in some cases, we were able to observe O_W (mass 18), and sometimes not, even when the experiment was performed in the same way. We have identified that this irreproducibility is linked to the beam induced damage caused by the measurement [59]. On oxide surfaces, oxygen is preferentially sputtered by the He⁺ ions. Once the V_O's are formed, they readily dissociate water according to equation 5.1, as was shown previously. This is demonstrated in figure 5.5b. The LEIS measurement (1 keV He⁺, scattering angle = 120°) was done in 1×10^{-8} mbar H₂¹⁸O backpressure during LEIS spectra acquisition. While in the first scan the ¹⁸O is hardly observable, it is growing at the expense of the ¹⁶O peak in later scans.

To eliminate this unintentional dosing of water during measurement, we cooled down the TSP cryoshroud with a LN₂. This resulted in almost no water molecules present in the background pressure. The LEIS measurement (1 keV He⁺, scattering angle = 120°) then shows no difference between a clean B layer before (black), and after dosing 225 L of H₂¹⁸O at RT (red). This result

was obtained reproducibly. Based on the results of LEIS measurements, we conclude that O_WH is not present on the surface.

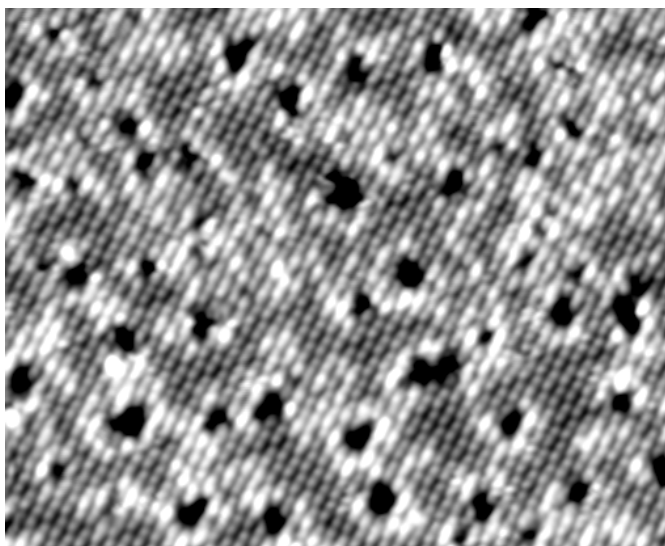


Figure 5.6: STM image of an OH saturated surface, annealed to 520 K. Dark areas cover 3.25% of the surface. Scanning details: $(30 \times 25) \text{ nm}^2$, $V_s = +0.94 \text{ V}$, $I_t = 0.3 \text{ nA}$.

Both STM and LEIS indicate that at RT and pressures under 10^{-5} mbar, water adsorption results only in the increase of surface O_SH, until a saturation coverage is reached. With this knowledge, we will now investigate the origin of the broad desorption peak of molecular water, centered at 520 K in figure 5.2. We performed a series of experiments, starting with a fully O_SH saturated surface, followed by a flash anneal to a selected temperature and an immediate cooling down to RT. For temperatures below 500 K, the density of surface O_SH was unchanged. Flash annealing to 520 K results in dark holes in the surface (see figure 5.6). These dark holes cover approximately 3.25% (equivalent of 0.26 ML of V_O's) of the surface area, while 0.16 ML of OH is still present on the surface. Further annealing to 550 K and above results in the disappearance of the dark patches and the recovery of a clean B layer surface. The formation of these dark holes is extremely sensitive to the annealing temperature and the dark holes can be observed only in an extremely narrow temperature range around 520 K. This is due to the experimental setup used and due to a small window between the extraction of water and refilling the V_O's with O from the bulk. In our experimental setup, annealing is done using a manipulator with an electron beam heating stage. Once we reached the desired temperature and switched off the annealing, the manipulator acted as a thermal reservoir, and the sample stayed at temperature within the desorption peak for prolonged time. Despite these experimental difficulties, the experiment was reproduced with D₂O.

5.2.2 Discussion

Our STM data demonstrate dissociative adsorption of water on the clean reconstructed B layer surface. This result is consistent with an XPS study [60], as well as with DFT+U calculations [38, 57]. The small saturation coverage we observe is linked to the availability of narrow sites, which are apparently necessary for the dissociation process. Surprisingly, both STM and LEIS indicate that, after water dissociation, O_WH is not present on the surface.

When the surface is saturated with O_SH and annealed to 520 K, dark patches appear. Under normal conditions, heating of the oxide surface with dissociated water molecules results in recombinative desorption of H and O_WH. Since O_WH is not present at the surface, an abstraction of O_S takes place via a Mars–van–Krevelen mechanism, according to equation 5.3:



According to equation 5.3, each desorbed water molecule removes two H atoms and creates one V_O. The dark patches in figure 5.6 cover the area corresponding to 0.26 ML of V_O's. Twice this value plus the coverage of remaining surface O_SH (0.16 ML) yields the initial coverage of surface O_SH of 0.68 ML. The surface of the B layer is thus reduced following exposure to water. This reduction is metastable, because the oxygen vacancies are reoxidized through O transfer from the bulk at temperature above 550 K, or by further reaction with water molecules at lower temperatures, forming a surface O_SH according to equation 5.1.

So far, we were unable to identify the fate of the O_WH species, created after water dissociation in the absence of V_O's. With the experimental techniques we have available, we can only conclude that O_WH species are not present on the surface. The possible scenarios for O_WH species are either diffusion into the bulk, or desorption to the gas phase. Diffusion into the bulk is not probable. The diffusion will have to be facilitated via site exchange, i. e. hopping of V_O's. Our sample preparation procedure includes significant annealing in O₂, resulting in an extremely low V_O density observed on the surface. The other possibility is desorption from the surface: either as an O_WH radical, or via a recombinative reaction between two O_WH radicals and desorption of O₂, H₂ + O₂, or H₂O₂. To fully understand this process, molecular beam scattering, currently not available in our group, would be necessary.

6 $\text{Fe}_3\text{O}_4(001)$ B layer: Typical defects

In this chapter, we will present the typical surface defects regularly observed on the reconstructed B layer surface. These include Fe adatoms, oxygen vacancies, and surface OH. We will introduce surface anti-phase domain boundaries (APDB), which are formed when reconstructed areas, out of phase by half a unit cell, meet. Finally, for an easy identification of the surface defects by the reader, we illustrate the presence of all these defects on an example STM image.

6.1 Surface anti-phase domain boundaries

The reconstructed B layer adapts a $(\sqrt{2} \times \sqrt{2}) R45^\circ$ symmetry, linked to a subtle lateral relaxation of the surface FeB and O rows. The reconstructed surface forms a narrow and wide site within the surface unit cell. When a new terrace is nucleated, the phase of the FeB row undulation is determined.

In STM images, we often see bright lines, running 45° with respect to the FeB row direction, and frequently turning by 90° . One of them is shown in image 6.1a (highlighted by yellow arrows). Interestingly, these lines always stop at the step edge; they never continue over the neighboring terrace. In figure 6.1b, we drew lines intersecting the wide adsorption sites on both areas separated by the boundary. Interestingly, the undulation of the FeB rows in these two areas is half of a unit cell out of phase. Therefore, the bright line is an anti-phase domain boundary (APDB). In figure 6.1c, we show a high resolution STM image of an APDB. The image contains an overlay highlighting the position of narrow and wide sites on a line crossing at the APDB. We also show the position of sub-surface ($S - 1$) FeA atoms. There is no discontinuity of the subsurface lattice. This observation, together with the observed termination of the APDB at step edges, proves that these APDB are different from the structural domain boundaries observed in $\text{Fe}_3\text{O}_4(001)$ thin films [52]. In figure 6.1d, we show a DFT+U derived model of APDB. The calculations were performed by Thomas A. Manz and David Sholl as a part of a joint publication [52]. This model shows the undulating FeB rows as gray and the number indicates the charge state of the sub-surface ($S - 1$) FeB atoms. This model is consistent with previous DFT+U calculations, where a narrow site is above Fe^{2+} cations in the ($S - 1$) FeB layer, while the wide site has Fe^{3+} in the ($S - 1$) FeB layer [40, 41].

APDB are typically decorated by bright double protrusions on top of the FeB rows. These look similar to surface OH, but have a slightly larger apparent height (by $\sim 5\%$). In the atomically

resolved image 6.1c, we observe areas on APDB absent of these bright protrusions; two neighboring narrow sites (n–n) are observed in the STM image. DTF+U calculations with a fixed (S – 1) charge order on the two different phases of B layer predicts that below the APDB in the (S – 1) layer, two pairs of Fe²⁺ are present [52]. This DFT+U calculation assumes a non-equilibrium situation¹, and is based on our experimental STM observation and the model calculated by Lodziana in ref. [40]. APDB parallel to the FeB row direction were never observed experimentally. This will correspond to two pairs of Fe³⁺ cations in the (S – 1) layer. Therefore, this scenario is crossed out in red in figure 6.1d.

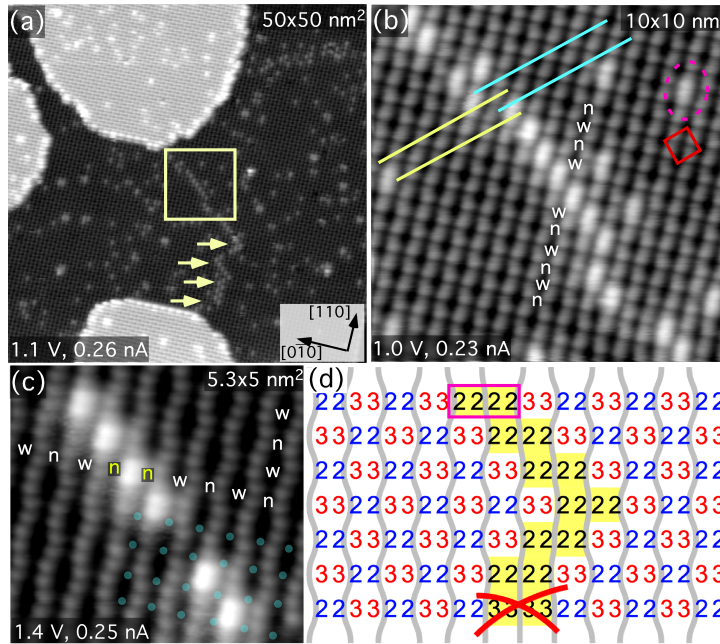


Figure 6.1: STM images of surface with anti-phase domain boundaries (APDB). (a) A large scale image with four terraces. Bright protrusion (indicated by yellow arrows) run across the lower terrace. These bright protrusions are terminated at the step edge; they do not continue on the neighboring terraces. (b) Zoom-in image of the area encompassed with the yellow square in (a). Yellow and cyan lines are centered in wide sites. FeB rows are out of phase by half a unit cell; the bright protrusions represent an APDB. (c) High resolution image of the APDB, with an overlay displaying subsurface FeA atoms, and narrow and wide sites labeled on a line across the boundary. (d) DFT+U derived schematic model of the APDB. Undulating FeB rows are gray, the numbers indicate the charge state of the subsurface (S – 1) FeB atoms (calculated by T. Manz and D. S. Sholl).

An example of the presence of two terraces with a different phase of the FeB row undulation is shown in figure 6.2. Part (a) shows a large scale STM image, obtained after a typical sputtering dose, but annealed at a low temperature (573 K, 20 minutes) in 2×10^{-10} mbar O₂ backpressure. Because of the low annealing temperature, the density of terraces is very large. In part (b), a zoom-in image with lines drawn above the wide sites demonstrates that the two neighboring terraces have half a unit cell phase shift in the undulation of FeB rows.

¹If the (S – 1) charge order will be not fixed for the two different phases of B layer, the APDB will be not created due to a small simulated unit cell.

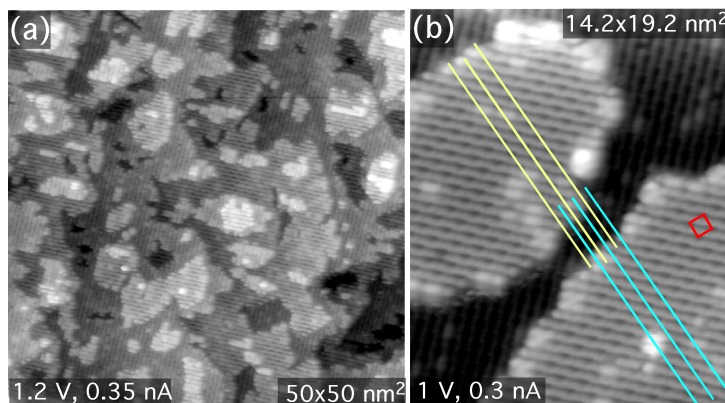


Figure 6.2: Formation of APDB during terrace growth. STM image of the $\text{Fe}_3\text{O}_4(001)$ sputtered and annealed to a low temperature (573 K). Many small terraces are formed, compared to annealing above 873 K. (b) Example of two neighboring terraces with the FeB rows out of phase.

6.1.1 Discussion

We found that APBD are commonly decorated by bright double protrusions on top of the FeB rows. We speculate that these are surface OH. We are able to increase the number of these bright protrusions by dosing water. DFT+U simulated images of the APDB show no bright protrusion at the APBD without OH, but with OH the bright pair of FeB atoms in the STM image can be simulated[52], with a preference for OH adsorption between the two narrow sites perpendicular to the FeB row direction (see image 6.1c). The slightly larger apparent height ($\sim 5\%$) measured in STM images may be explained by differences in the electronic structure at the APDB. Because we are imaging the surface at RT, we have never seen the nucleation of APDB directly. However, two possible explanations for the formation of APDB can be deduced from the RT STM images. The first case involves two terraces with an opposite phase (see figure 6.2b) merging together. Secondly, for temperatures above 723 K, the surface undergoes a phase transition and the $(\sqrt{2} \times \sqrt{2}) R45^\circ$ reconstruction disappears (private communication with Juan de la Figuera). APDB should thus be removed after annealing above 723 K, and they should be formed again when the crystal is cooled down below 723 K. If this assumption is correct, it should be possible to tune the density of the APDB by controlling the cooling rate around 723 K.

6.2 Other typical defects

As an example for the typical defects on the $\text{Fe}_3\text{O}_4(001)$ B layer, figure 6.3 shows an STM image of a clean surface. Highlighted are the crystallographic directions (left bottom corner), a unit cell (cyan), and the typical defects: surface OH, FeA adatom, $\text{H}_2\text{O} + \text{V}_\text{O}$ and V_O .

As discussed, OH groups appear as a bright double protrusion on top of two FeB atoms. OH can be easily identified in STM movies at RT, because of its characteristic hopping between two

Chapter 6. Fe₃O₄(001) B layer: Typical defects

positions within the narrow site. Due to this hopping, it is possible to identify the position of the relevant narrow site from STM movies, even in cases where the resolution is not good and the undulation of the FeB rows is not resolved.

Surface FeA adatoms appear as a single bright protrusion between the FeB rows. This defect was first identified by Stanka in ref. [32]. A detailed analysis of FeA adatoms is presented in section 7.1.1. The FeA are always located in the narrow site. We label these adatoms FeA, because they adapt the bulk continuation site of the FeA atoms. The apparent height of FeA is 80 pm (for imaging conditions: $V_s = +1$ V, $I_t = 0.3$ nA). FeA adatoms are only rarely mobile. Whenever the mobility of FeA adatoms was observed, they always moved along the FeB row direction.

We assume that dark holes in the surface are surface oxygen vacancies (V_O). We were unable to create V_O 's artificially by means of electron stimulated desorption. From LEIS measurements performed during H₂O experiments, we know that V_O 's strongly reacts with water (see figure 5.5). This mechanism explains why OH are frequently observed in pairs: a water molecule is dissociated, oxygen fills the V_O and two H atoms adsorb in the vicinity. More evidence that surface V_O 's look like a dark hole in the surface comes from experiment involving annealing the O_sH saturated surface to 520 K (see figure 5.6). We observed dark holes in the surface, which we linked to reduction of the surface.

Together with the APDB (see section 6.1), these are the typical defects present on a clean, reconstructed B layer surface.

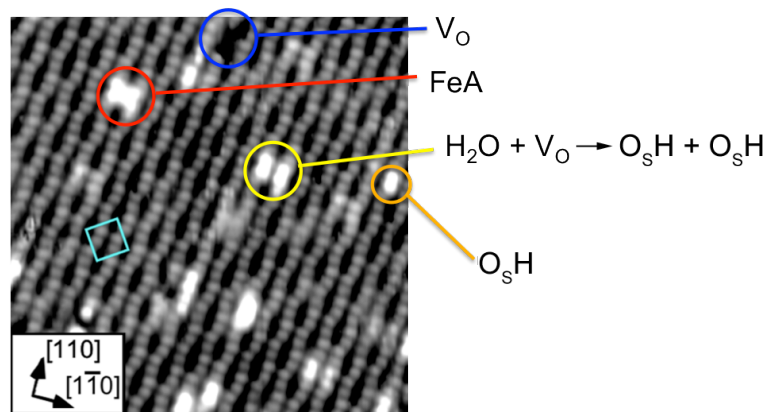


Figure 6.3: STM image of a clean B layer surface with typical defects highlighted in the image. These include an FeA adatom, a surface OH, an oxygen vacancy (V_O) and a H₂O molecule dissociated in V_O . The $(\sqrt{2} \times \sqrt{2}) R45^\circ$ unit cell is marked with cyan square. Scanning details: (20×20) nm², $V_s = +1$ V, $I_t = 0.3$ nA.

7 Fe-rich (001) surface terminations

In the literature, there is a general agreement about the $(\sqrt{2} \times \sqrt{2}) R45^\circ$ symmetry of the (001) terminated surface [61, 33, 32, 62, 35]. In section 2.2, a reconstructed, octahedrally terminated B layer of the $\text{Fe}_3\text{O}_4(001)$ surface was described. This model explains the change in symmetry as a consequence of lateral relaxation of the rows of surface FeB and O atoms. However, several different surface terminations were proposed, both theoretically and experimentally, in order to explain the $(\sqrt{2} \times \sqrt{2}) R45^\circ$ symmetry and to satisfy requirements for compensating the polarity of this surface. The proposed models include an ordered array of oxygen vacancies in the B layer (B + V_O) [63], sub-surface Fe dimers [33], 0.5 ML Fe dimers [62], and a theoretically predicted 1 ML FeA terminated surface [35, 40].

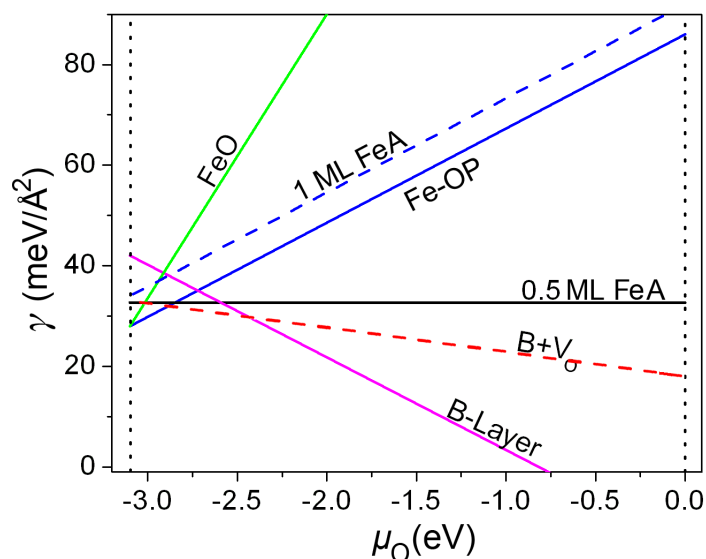


Figure 7.1: DFT+U derived surface phase diagram [39]. The surface free energy is plotted as a function of oxygen chemical potential for several different surface terminations. The broken line to the left corresponds to formation of metallic Fe, and to the right to condensation of oxygen. Terminations B + V_O and 1 ML FeA are shown with dashed lines because they were not observed experimentally so far.

Figure 7.1 shows a surface phase diagram of the (001) surface, as obtained within the framework of ab initio atomistic thermodynamics [39, 64]. The surface free energy is plotted as a function of oxygen chemical potential for several different surface terminations. The surface with the lowest surface energy should be the favorable one. This phase diagram shows that a reconstructed B layer is the preferred termination over a wide range of the oxygen chemical potential. On the other hand, at low oxygen chemical potential, a variety of Fe rich surface terminations are favorable according to these DFT+U calculations.

In this chapter, we will demonstrate two different routes to produce various Fe rich surface terminations. The first approach includes deposition of Fe onto a well defined, reconstructed B layer surface. The second approach utilizes reduction of the surface region via sputtering and controlling the temperature and oxygen chemical potential.

In this chapter, we will use a different definition for 1 ML, also adapted in later chapters. Here, (1 ML*) is defined as two extra atoms per reconstructed ($\sqrt{2} \times \sqrt{2}$) $R45^\circ$ surface unit cell. This corresponds to 2.84×10^{14} atoms/cm². We will use the asterisk symbol to distinguish between these two monolayer definitions.

7.1 Deposition of Fe onto the B layer surface

The aim of this section is to probe the surface phase diagram (see figure 7.1) towards the Fe-rich limit by depositing Fe onto the reconstructed B layer. We will vary the temperature and amount of deposited Fe. This approach has the advantage that large, flat terraces of the B layer substrate are maintained. The experiments are easily reproducible because of the well defined substrate. All STM images shown in this section were acquired at RT. Experimental data are supported by DFT calculations¹, revealing more insights into the electronic structure of these Fe-rich terminations.

7.1.1 Fe deposition at RT: adatoms and clusters

Figure 7.2a shows an STM image after deposition of 0.025 ML* of Fe onto a clean reconstructed B layer at RT. The deposited Fe appears as bright protrusions, marked by yellow circles in figure 7.2a. The inset shows a high resolution image of one Fe adatom. The position of the narrow (n) and wide (w) site is highlighted along the row where the Fe adatom is adsorbed. We observe the Fe adatom in the centre of the narrow site, occupying the two fold coordinated bridging oxygen site. The apparent height of FeA is 80 pm.

The adsorption site can be identified only with the help of surrounding clean surface. Once an Fe atom is adsorbed, the narrow site is not strictly narrow anymore (from a geometrical point of view). Since the Fe adatoms adopt bulk continuation FeA sites, we call them FeA adatoms. In all STM images, the FeA adatoms were always observed in the narrow site; occupation of a wide site was never observed.

For Fe coverage in excess of ~ 0.5 ML* (i.e., 1 atom per surface unit cell), we observe clusters on the surface. These are shown in the STM image in figure 7.2b following deposition of 0.8 ML* Fe at RT. The Fe clusters are bright, line-shaped features. They grow perpendicular to the FeB row direction, and both ends of these line-shaped clusters are typically located on top of a narrow site. The zoom-in image (see inset in figure 7.2b) shows an area with a low

¹DFT + U calculations were performed by M. Mulakaluri and R. Pentcheva as a part of a joint publication [39].

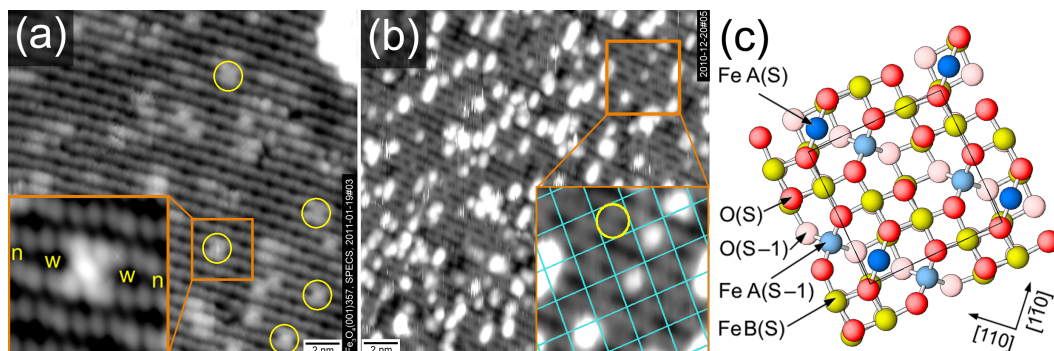


Figure 7.2: Fe deposition onto the B layer at RT: (a) STM image after deposition of 0.025 ML* Fe at RT. Fe adsorbs as adatoms (marked with yellow circles) in the narrow adsorption site (see high resolution inset). (b) STM image after deposition of 0.8 ML* Fe at RT. Fe adsorbs in the form of FeA adatoms and Fe clusters. FeA adatoms occupy positions consistent with the $(\sqrt{2} \times \sqrt{2}) R45^\circ$ symmetry of the reconstructed surface, as is highlighted in the high resolution inset with a cyan grid overlay, together with one FeA adatom marked with a yellow circle. (c) Structural model of the 0.5 ML FeA termination (see also figure 7.1), as determined by DFT+U calculations. Scanning details: $(20 \times 20) \text{ nm}^2$, $V_s = 1 \text{ V}$, $I_t = 0.3 \text{ nA}$ (both STM images).

local density of clusters. In this image, a cyan grid shows the $(\sqrt{2} \times \sqrt{2}) R45^\circ$ symmetry of the substrate, with the nodes centered at wide sites. A vast majority of narrow sites is filled with FeA adatoms, forming a 0.5 ML FeA termination (see phase diagram in figure 7.1). In part (c), we show the DFT+U derived model for the 0.5 ML FeA termination. The calculations reveal that the FeA atoms relax strongly inward relative to the bulk Fe(A) position: their relative height with respects to the surface oxygen is only 0.45 Å (compared to 1.07 Å in a truncated bulk). As a consequence, the neighboring oxygen atoms relax away to a separation of 3.63 Å (bulk separation is 2.85 Å). The neighboring FeB rows also relax away to separation of 6.21 Å (bulk separation is 5.94 Å). We note that the same result was obtained, irrespectively whether the FeA was initially placed into narrow or wide sites.

7.1.2 Fe octahedral pairs

The phase diagram shown in figure 7.1 indicates that the reconstructed B layer is favorable over a broad range of chemical potentials. With decreasing μ_O , $B + V_O$ was theoretically predicted, but never observed experimentally. However, we observe a 0.5 ML FeA termination at low μ_O . At even more reducing conditions, a termination with octahedral pairs² of Fe (Fe–OP, see model in figure 7.3) is predicted by the phase diagram. The Fe–OP termination consists of a B layer with two extra Fe atoms in the octahedral position within the narrow site (see figure 2.3). We will show that a temperature above RT is necessary to transform the reconstructed B layer to the Fe–OP termination.

In the previous section, when 0.8 ML* Fe was deposited at RT, we observed 0.5 ML FeA layer and clusters (see figure 7.2b). Figure 7.3a shows this surface after flash–annealing to 423 K. After flash–annealing, the number of clusters is significantly reduced, but the size of the clus-

² In literature, Fe–OP's are often called Fe dimers [53, 62]. As will be shown later, there is no bond between the additional Fe atoms. For this reason, the nomenclature Fe–OP seems to be more reasonable.

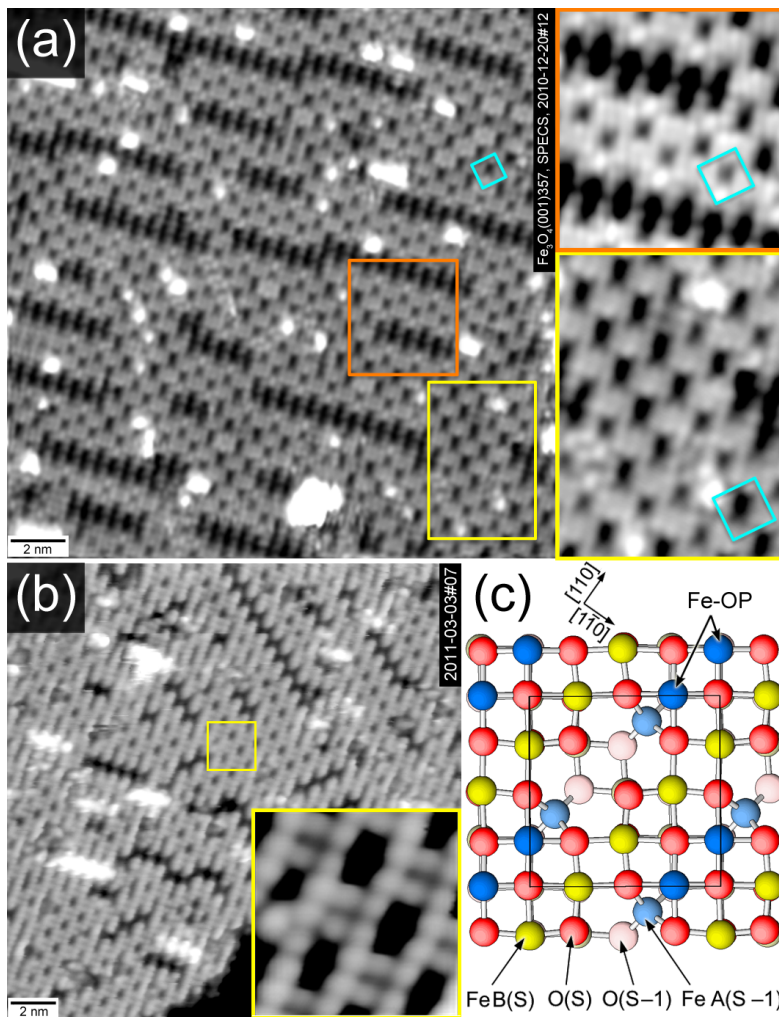


Figure 7.3: Formation of Fe octahedral pairs (Fe-OP). (a) STM image following post-deposition annealing of 0.8 ML* Fe (shown in figure 7.2b) to 423 K. Two insets show an area with a low local Fe coverage (orange frame, right top), and with a high coverage of Fe (yellow frame, right bottom), respectively. For a low coverage, isolated Fe atoms coexist with Fe-OP at the boundaries between clean surface and Fe-rich areas. At areas with a high Fe coverage only Fe-OP are observed. Scanning details: $(20 \times 20) \text{ nm}^2$, $V_s = +0.91 \text{ V}$, $I_t = 0.34 \text{ nA}$. (b) STM image after deposition of 0.7 ML* Fe onto a reconstructed B layer at RT, post-deposition annealed to 573 K. The surface contains only Fe-OP. The inset shows a high-resolution image of the Fe-OP. Scanning details: $(20 \times 20) \text{ nm}^2$, $V_s = +1.03 \text{ V}$, $I_t = 0.32 \text{ nA}$. (c) Top view of the Fe-OP model, as determined by DFT+U calculations.

ters does not increase. Instead, Fe is redistributed across the surface, and a large number of Fe-OP's with the $(\sqrt{2} \times \sqrt{2})R45^\circ$ symmetry are formed. In Fe-rich areas, Fe-OP's cover the surface completely (see area encompassed with a yellow rectangle and the corresponding inset). Areas with locally less Fe exist, leading to boundaries between the B layer and the Fe-OP phase (see area encompassed with an orange square and the corresponding inset). These boundaries are perpendicular to the FeB row direction, and are formed by an alternating

7.1. Deposition of Fe onto the B layer surface

sequence of Fe monomers and Fe–OP. Similar to the FeA adatoms, Fe monomers occupy the tetrahedral position, not the octahedral one.

The mixture of two phases (FeA and Fe–OP) can be prevented by annealing the surface to a higher temperature. This is shown in figure 7.3b, where 0.7 ML* Fe was deposited at RT and annealed to 573 K for 15 minutes after deposition. Only Fe–OP's with the $(\sqrt{2} \times \sqrt{2}) R45^\circ$ symmetry are observed. The line-shaped boundaries between the B layer (dark in the terrace, because of the chosen brightness/contrast) and Fe–OP phase are oriented 45° with respect to the FeB row direction. In the inset, we show an atomically resolved image.

The DFT+U derived structural model of the Fe–OP termination is shown in figure 7.3c. The extra Fe atoms adopt the octahedral positions within the narrow region of the reconstructed unit cell. These Fe atoms are five-fold coordinated to the neighboring oxygen atoms, 0.54 Å above the fourfold hollow site, with Fe–O bond lengths of 2.04 Å. Within the narrow site, the bonds between O(S)–FeB(S) and O(S)–FeB(S – 1) are elongated to 2.27 Å, because of the presence of the Fe–OP. In a wide site, the bond lengths for the under-coordinated O atoms are reduced to 1.96 Å. DFT+U indicates no bond between the Fe–OP; it is therefore inaccurate to term these Fe dimer (see footnote 2).

Both STM and DFT+U calculations indicate that, upon Fe adsorption, strong relaxations within the surface occur. From a geometrical point of view, the formally narrow site is not longer narrow after extra Fe is incorporated. We observe the $(\sqrt{2} \times \sqrt{2}) R45^\circ$ symmetry for both 0.5 ML FeA and Fe–OP termination. However, images with a near full coverage of both of these terminations do not contain areas of B layer that are large enough to allow determination of the adsorption site unambiguously. Moreover, DFT+U calculations converge to the same results irrespectively of placing Fe–OP initially into the narrow or wide region of the reconstructed unit cell.

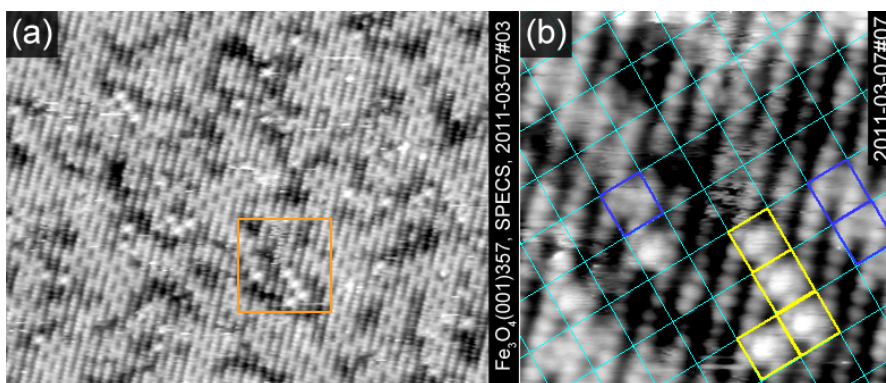


Figure 7.4: Proof that Fe–OP adsorb in the narrow site. (a) STM image following deposition of 0.3 ML* Fe at a slightly elevated temperature (real temperature is unknown: between RT and ~373 K) onto a clean surface. We observe both Fe monomers and Fe–OP. The orange frame highlights an area shown in (b). In this zoom-in image, the $(\sqrt{2} \times \sqrt{2}) R45^\circ$ symmetry is highlighted with a cyan grid; Fe monomers are highlighted with yellow color and Fe dimers with blue color. Scanning details: (a) $(30 \times 20) \text{ nm}^2$ and (b) $(6.5 \times 6.5) \text{ nm}^2$. $V_s = +1 \text{ V}$, $I_t = 0.3 \text{ nA}$ (both images).

To clarify whether Fe–OP adsorb within the narrow or wide site, we show in figure 7.4 an STM image following deposition of 0.3 ML* Fe at an unknown temperature (between RT and 373 K).

Because of the low coverage of deposited Fe, large areas of clean surface are observed. We also observe a large number of isolated FeA and Fe-OP in the image. The apparent height of FeA adatoms agrees with the previously measured value of 80 pm. The zoom-in inset into the area marked by an orange square is shown in figure 7.4b. Here, a $(\sqrt{2} \times \sqrt{2}) R45^\circ$ grid overlay has its nodes centered in the wide sites. The cells with FeA are highlighted with yellow color, while the unit cells with Fe-OP are highlighted with blue. From previous work, we know that FeA adatoms always adsorb in the narrow site. Since we can observe both FeA and Fe-OP, they both adsorb in the same site in image 7.4.

The results of this section suggest that there is a thermal barrier for formation of Fe-OP; we were unable to form Fe-OP at RT. For a perfectly ordered Fe-OP termination, higher annealing temperature is necessary (~ 573 K), while at lower annealing temperature (~ 423 K), a mixture of two phases is observed.

7.1.3 High Fe coverage

With further deposition of Fe, the competition between Fe-OP termination and FeO is predicted by the surface phase diagram (see figure 7.1). We also observed this experimentally, as we show with an STM image in figure 7.5. The image was acquired following deposition of 2 ML* of Fe onto reconstructed B layer at ~ 573 K. The majority of the surface is covered with Fe-OP, but areas with a square lattice can be found on the surface. This FeO-like structure is usually observed at a lower terraces, but a direct transition from Fe-OP to FeO on the same terrace was also observed. The FeO-like structure suggests occupation of the octahedral sites within both narrow and wide sites. The FeO termination contains a large number of defects,

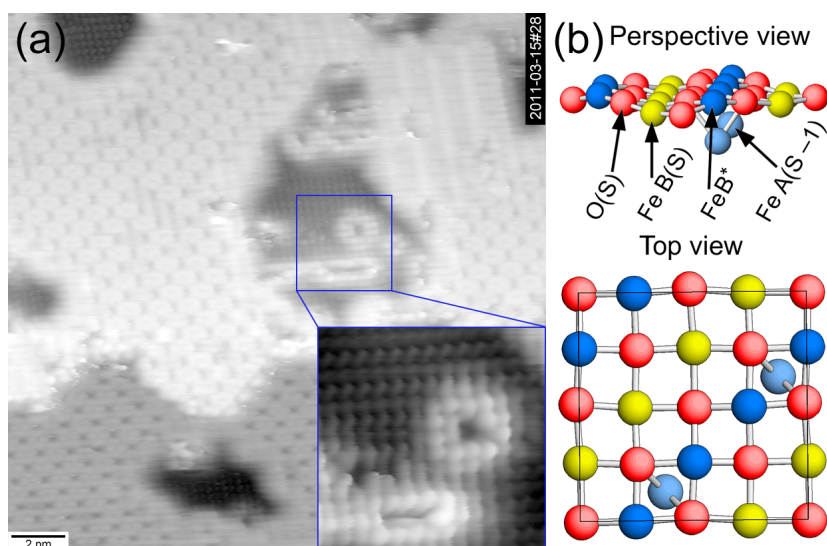


Figure 7.5: (a) STM image following deposition of 2 ML* Fe at 573 K. The Fe-OP termination coexist with an FeO-like termination with (1×1) symmetry. (b) DFT+U structural model of the FeO-like termination. All octahedral sites are filled with Fe. Note the additional FeB*(S) row is slightly elevated above FeB rows. Scanning details: (20×20) nm², $V_s = +0.65$ V, $I_t = 0.32$ nA.

possibly caused by the mismatch between the Fe-O bond length in FeO (2.17 Å) and Fe₃O₄ (2.14 Å). Since the number of the atoms visible on the surface is visibly smaller than 2 ML*,

7.1. Deposition of Fe onto the B layer surface

some of the Fe apparently has diffused into the sub-surface region. The DFT+U determined structure of the FeO-like termination is shown in figure 7.5c. The calculations reveal a strong buckling (0.48 \AA) between the original FeB rows and the newly created FeB* (S) rows. Along the FeB (S) rows, a modulation of the FeB-FeB distance occurs for both the original FeB (S) and new FeB* (S) rows, with alternating shorter (2.87 \AA) and longer ($3.08 - 3.10 \text{ \AA}$) bonds. Because of the FeB* (S) rows, the sub-surface FeA (S-1) are pushed toward the (S-1) FeB layer, resulting in shorted FeA(S-1)-O(S-1) bond lengths of 1.81 \AA , and significantly longer ones to the surface oxygen (2.36 \AA). The O(S)-FeB(S-1) bond lengths are also elongated to $\sim 2.38-2.41 \text{ \AA}$, compared to bulk value of 2.06 \AA .

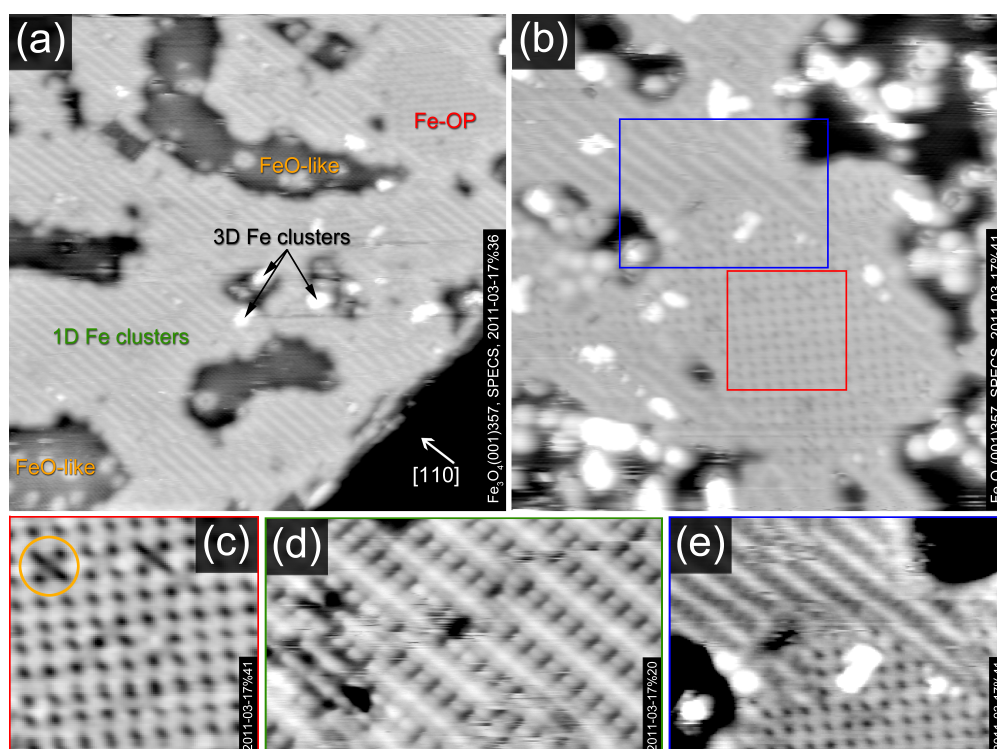


Figure 7.6: High Fe coverage. STM images following deposition of 6 ML^* of Fe at 573 K onto a clean B layer surface. (a) A large scale image ($50 \times 50 \text{ nm}^2$) shows four competing phases of Fe: 3D Fe clusters (oversaturated in the image), Fe-OP, FeO-like areas (two areas highlighted in the image, but not well resolved due to the chosen brightness/contrast settings), and 1D Fe clusters. (b) Smaller scale ($30 \times 30 \text{ nm}^2$) image centered in the top-right corner of (a). The image shows a boundary between Fe-OP area and 1D Fe clusters. A zoom-in image of the Fe-OP area is shown in (c), with one Fe-OP vacancy highlighted with an orange circle. A high resolution ($10 \times 6 \text{ nm}^2$) image of 1D Fe clusters show that they are perpendicular to the underlying FeB rows, as is shown in (d). (e) a high-resolution image of the boundary between Fe-OP and 1D Fe clusters shows that at the surface, FeB rows and 1D Fe clusters are both parallel to the $[110]$ direction (blue frame in part (b)). Image details: (a) $V_s = +0.63 \text{ V}$, $I_t = 0.24 \text{ nA}$, (b) $V_s = +1.2 \text{ V}$, $I_t = 0.26 \text{ nA}$, (c). $V_s = +0.65 \text{ V}$, $I_t = 0.29 \text{ nA}$.

An extreme case of surface reduction is shown STM in figure 7.6. Here, 6 ML^* of Fe was deposited onto B layer surface at 573 K . This coverage leads to several distinct phases existing

concurrently. Small areas on the surface adapt the already described FeO-like structure, as highlighted in figure 7.6a (although not well resolved due to the chosen brightness/contrast settings). We observe the FeO termination always in the lower layers. Second, we observe Fe clusters (oversaturated features in figure 7.6a). Third, Fe-OP are present on the surface (top right area in figure 7.6a). Finally, we observe a new type of a 1D row-like termination covering a large portion of the surface. These rows have a separation of 11.8\AA . This value corresponds to a $\sqrt{2}$ multiple of the size of a surface unit cell, or the distance between two narrow sites in a direction perpendicular to FeB rows. Later in the text, we will term this termination 1D Fe rows.

In figure 7.6b, we show an image of a boundary between Fe-OP and 1D Fe rows. A high resolution image of 1D Fe rows is shown in (d), the boundary between Fe-OP and 1D Fe rows is shown in (e), and the Fe-OP area in (c). As the high resolution image in (d) shows, the 1D Fe rows are perpendicular to the underlying $(S - 1)$ FeB rows. These $(S - 1)$ FeB rows have a typical inter-row distance of $\sim 6\text{\AA}$. Surprisingly, at the boundary to between Fe-OP and 1D Fe rows (e), we observe a smooth transition within the same terrace. A high resolution image of the Fe-OP termination (c) shows one defect highlighted by an orange circle, possibly caused by a missing pair of Fe atoms.

This surface termination has to involve a substantial rearrangement of atoms in at least the surface (S) and subsurface $(S - 1)$ layer. Due to the uncertainty of the number of atoms diffusing into the bulk, we do not have a suitable model for the 1D Fe rows phase. As the surface is not well defined anymore, we stopped investigation and did not increase of the amount of deposited Fe any further.

7.1.4 Fe-rich terminations of $\text{Fe}_3\text{O}_4(001)$: electronic structure

The electronic structure of the Fe-rich phases was investigated by DFT+U and XPS. The calculations were done by M. Mulakaluri and R. Pentcheva as a part of a joint publication [39]. In figure 7.7a, we show the projected (first two rows) and total (3rd row) local DOS for the B layer, 0.5 ML FeA, Fe-OP, and FeO termination. The DOS is plotted separately for a majority (up) and a minority (down) spin component. Part b of figure 7.7 shows a perspective view model of each configuration. Here, red and blue constant density contours represent the two opposite spin orientations of the FeB and FeA sub-lattice, respectively. A spherical spin density distribution represents sites with Fe^{3+} , while deviation from the spherical distribution is characteristic for Fe^{2+} cations.

For a B layer termination, all atoms in the surface FeB (S) and subsurface FeA $(S - 1)$ layer are Fe^{3+} . The subsurface FeB $(S - 1)$ layer contains alternating pairs of Fe^{2+} and Fe^{3+} cations, ordered with the $(\sqrt{2} \times \sqrt{2}) R45^\circ$ symmetry. A similar charge ordering (CO) of the FeB $(S - 1)$ cations was observed previously [40, 41]. The CO in the sub-surface layers leads to a half-metal to insulator transition in the surface.

The 0.5 ML FeA termination shows a transition to half-metallic surface, as shown in the total DOS. While the FeB (S) and FeA $(S - 1)$ are still Fe^{3+} , the additional FeA (S) atoms are Fe^{2+} .

For Fe-OP and FeO, we call the extra Fe atoms FeB* in the DOS. In case of these two terminations, all Fe atoms in the (S) layer, as well as FeA in the $(S - 1)$ layer, are reduced to Fe^{2+} . Moreover, the additional FeB* atoms in the Fe-OP and FeO termination align their spin antiparallel to the original FeB (S) rows. The reduction of the surface is visible in the XPS. Figure 7.8 shows Fe $2p$ and O $1s$ core level spectra for B layer and Fe-OP termination.

7.1. Deposition of Fe onto the B layer surface

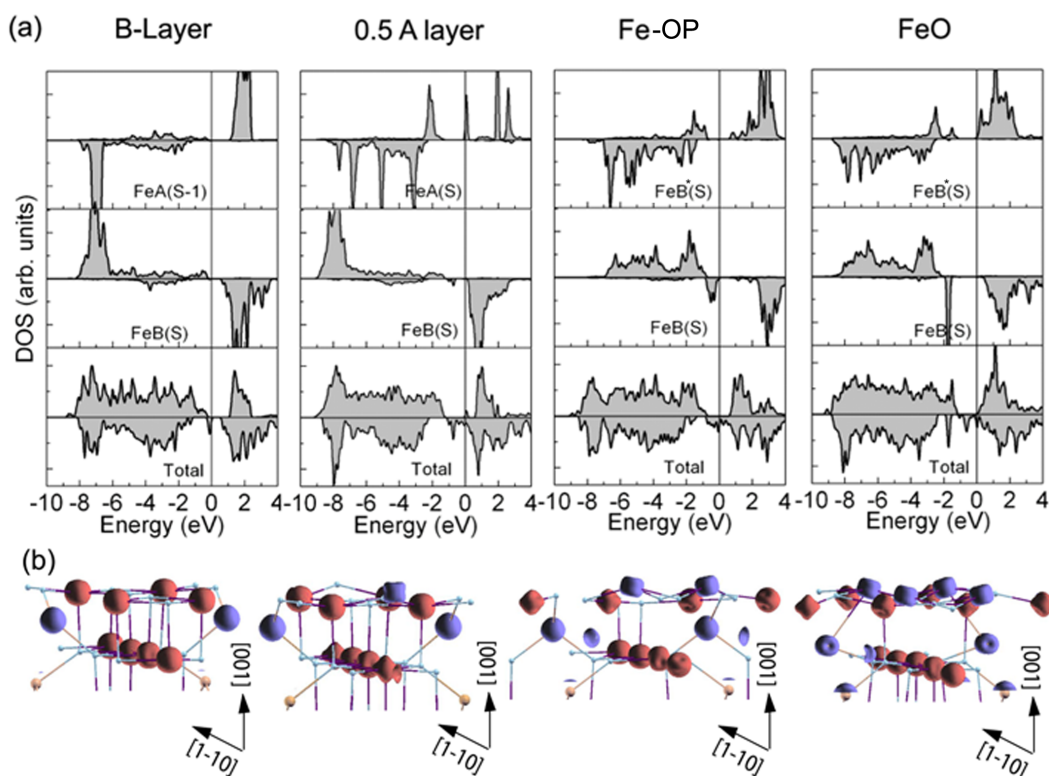


Figure 7.7: Density of states (DOS) and spin density for the surface terminations shown in figure 7.1. (a) Top and middle row shows a projected DOS of the surface (S) and subsurface (S-1) FeA and FeB 3d states, respectively. FeB* denotes additional FeB atoms forming Fe-OP and FeO termination. The bottom row shows the total DOS. (b) Blue and red represents two different spin orientations. A spherical spin distribution indicates Fe³⁺ cation and deviation from the spherical shape indicates an Fe²⁺ cation. Small light blue spheres represent oxygen atoms. The DFT+U calculations were performed by M. Mulakaluri and R. Pentcheva as a part of a joint publication [39]

The data were acquired at normal and grazing emission angle (60° from the surface normal). For a B layer, the O 1s peak appears as previously [34], located at 530 eV [25]. For the Fe-OP surface, the O 1s has a same shape, but is shifted slightly towards lower BE. The energy range in the presented figure was not calibrated, and the observed BE shift could be partially caused by the change in the analyzer's work function. The Fe 2p_{3/2} peak is located at 711.4 eV, and shows contributions from Fe²⁺ and Fe³⁺. On the B layer, the Fe 2p_{3/2} peak is dominated by the Fe³⁺ component. The Fe enrichment of the Fe-OP as compared to a B layer termination is confirmed by a higher intensity of Fe 2p, while the intensity of O 1s is slightly lower. In the spectra for the Fe-OP termination, the Fe²⁺ component is more prominent, especially in grazing emission. The Fe²⁺ nature of the Fe-OP surface is also demonstrated by the shake-up features observed at 717 eV.

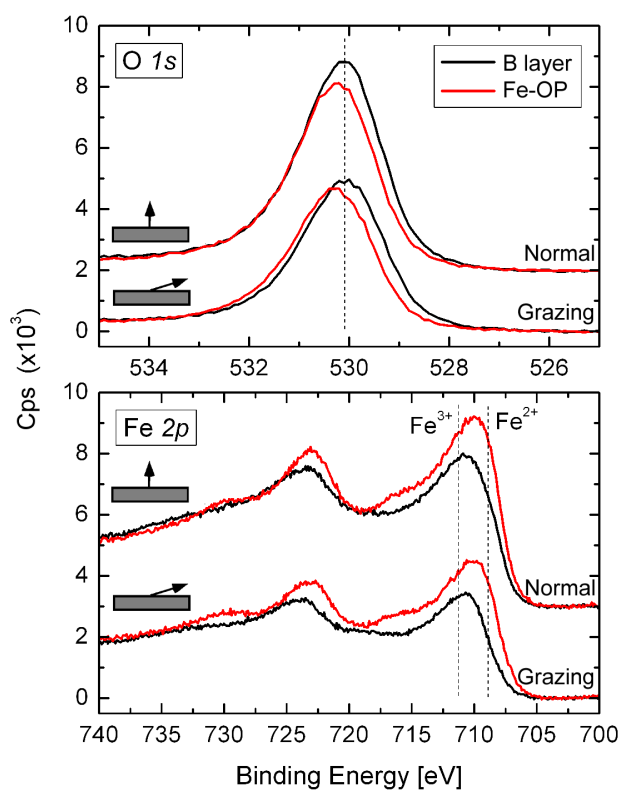


Figure 7.8: XPS spectra for a reconstructed B layer and an Fe-rich surface terminated with Fe-OP's. Spectra were obtained for normal and grazing take-off angle. For an Fe-rich surface, the O 1s is reduced in intensity and slightly shifted by 0.2 eV towards higher BE. For Fe $2p_{3/2}$, a shoulder at the lower BE side of the peak and a satellite peak at 717 eV indicates the presence of Fe⁺² cations. Comparison between the normal and grazing spectra shows that the Fe⁺² cations are present at or near the surface.

7.1.5 Discussion

Our results suggest that Fe forms only single adatoms and clusters at RT. Not a single Fe octahedral pair was ever observed when Fe was deposited at RT. The energy barrier for Fe-OP formation was not determined, but is higher than RT and lower than 423 K. Nevertheless, at 423 K we observe a mixed phase between 0.5 ML FeA and Fe-OP. In order to obtain a surface terminated with only Fe-OP, a higher annealing temperature of 573 K is necessary. We speculate that the difference between the mixed phase (0.5 ML FeA and Fe-OP), and Fe-OP phase is linked to the mobility of single FeA adatoms.

Diffusion of FeA adatoms is very rare at RT. The mobility of FeA adatoms was always observed between neighboring narrow sites along the FeB row direction. Cross row diffusion was never observed. We speculate that, at elevated temperature (between RT and 423 K), FeA adatoms increase their mobility along the row direction, but do not have enough energy for cross-row

7.2. Influence of sample preparation on the surface termination

diffusion. When two FeA meet, an Fe–OP is formed. This can lead to a situation when a FeA monomer is trapped between two Fe–OP's. In contrast, we observe only Fe–OP after annealing to 573 K, irrespective of the Fe coverage. This could indicate that at this energy, cross-row diffusion of FeA adatoms is not longer hindered.

The B layer, 0.5 ML FeA and Fe–OP termination have the same symmetry. Only by means of (qualitative) LEED are these terminations indistinguishable. In order to determine the surface termination unambiguously, the surface has to be imaged by STM, eventually measured by another surface sensitive technique (LEIS, XPS). In agreement with the surface phase diagram (see figure 7.1), we found all the Fe–rich terminations to be metastable. They can be transformed to the B layer by annealing at elevated temperatures. Two surface terminations predicted by DFT+U (B + V_O, 1 ML FeA) were never observed experimentally, despite extensive attempts.

Fe–OP is often called Fe dimer [62, 53], although DFT+U calculations do not predict any bond between Fe atoms (see footnote 2). In contrast, when mobility of Fe–OP was observed, both atoms forming Fe–OP moved together. As in the case of FeA adatoms, Fe–OP move along the FeB rows.

With a higher amount of deposited Fe, an FeO–like phase was observed together with Fe–OP. A further increase in the amount of deposited Fe resulted in several concurrently occurring phases of Fe, and large areas of the surface became disordered.

7.2 Influence of sample preparation on the surface termination

An alternative way of producing the Fe–rich terminations uses the opposite approach to the one discussed so far: an initially reduced surface is oxidized in a controlled manner. This was demonstrated in ref. [62], where a Fe₃O₄(001) thin film was grown on Fe(001) buffer layer and Fe–OP were observed. We will introduce an alternative approach to ref. [62]: a B layer surface will be reduced by 1 keV Ar⁺ sputtering for 15 minutes (ion current ~1 μA). According to TRIM simulations [65] for our preparation conditions, oxygen is preferentially sputtered by a factor of ~2.5, leading to an Fe–rich surface. After sputtering, the surface becomes disordered, with no observable LEED pattern (data not shown). The results for annealing at different temperature and oxygen conditions are demonstrated in the surface phase diagram shown in figure 7.9.

When the reduced surface is annealed to 623 K and imaged with STM at RT, we observe FeA adatoms together with Fe–OP. This temperature is high enough to facilitate oxygen diffusion from the bulk, but the surface non–stoichiometry is preserved. If the annealing temperature is higher (773 K), only FeA adatoms are observed on the B layer terminated surface. Annealing the reduced surface to 973 K restores the B layer termination with flat terraces. The B layer termination can be restored at even lower anneal temperatures with the addition of oxygen (623 K, $p = 2 \times 10^{-6}$ mbar), but in this case, the terraces are typically small, even after a prolonged annealing time.

In this section, we presented an alternative route to produce Fe–rich Fe₃O₄(001) surface terminations by only one sputter–anneal cycle. It should be noted, however, that results of this section are fully applicable only to SSC No. 357. As shown in appendix B.1, the UHV annealing of magnetite single crystals depends on their stoichiometry.

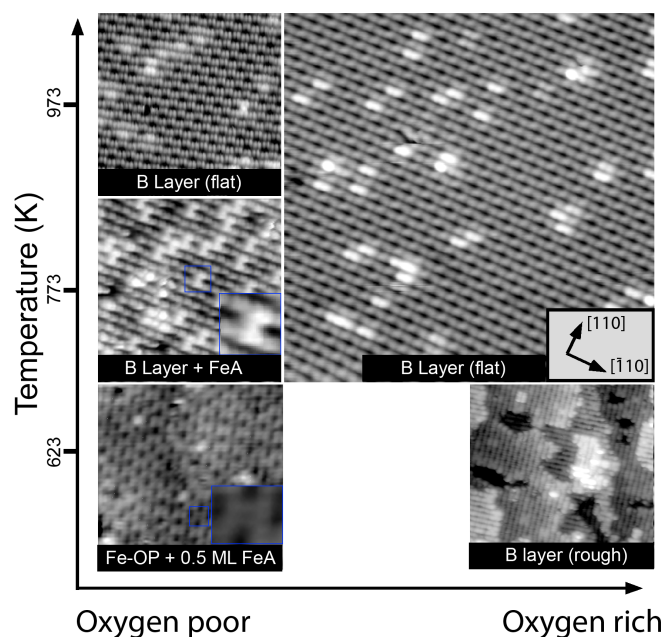


Figure 7.9: Surface phase diagram for SSC No. 357, showing the surface termination as a function of temperature and oxygen chemical potential. The B layer surface was initially reduced by sputtering (1 keV Ar⁺, ~1 μA, 15 minutes), and annealed to the stated temperature either in UHV, or in O₂ ($p = 2 \times 10^{-6}$ mbar).

7.3 Outlook

The ability to create Fe-rich Fe₃O₄(001) surface terminations allows us to tune the surface properties. Under-coordinated Fe cations of the FeA (S) and Fe-OP terminations could be active sites for dissociation of molecules. For example, on the Fe₃O₄(111), the surface terminated with O anions is inert, while the surface terminated with Fe cations introduces active sites for molecule dissociation [66]. Analogously, Fe-rich terminations could increase the reactivity compared to a relatively inert B layer surface.

No reactivity studies of the (001) Fe rich surfaces (0.5 ML FeA, Fe-OP termination) were reported so far. We conducted only one experiment involving water dosing onto Fe-OP terminated surface at RT. The STM image before water dosing is shown in figure 7.10a (1.2 ML* Fe deposited at ~373 K). STM shows a full coverage of Fe-OP, and a few linear 1D clusters perpendicular to the FeB rows. After dosing 160 L of H₂O at RT, many bright protrusions, located atop of the Fe-OP appear as a consequence of water exposure. This preliminary result indicates the Fe-OP termination reacts with water, and possibly with other molecules as well.

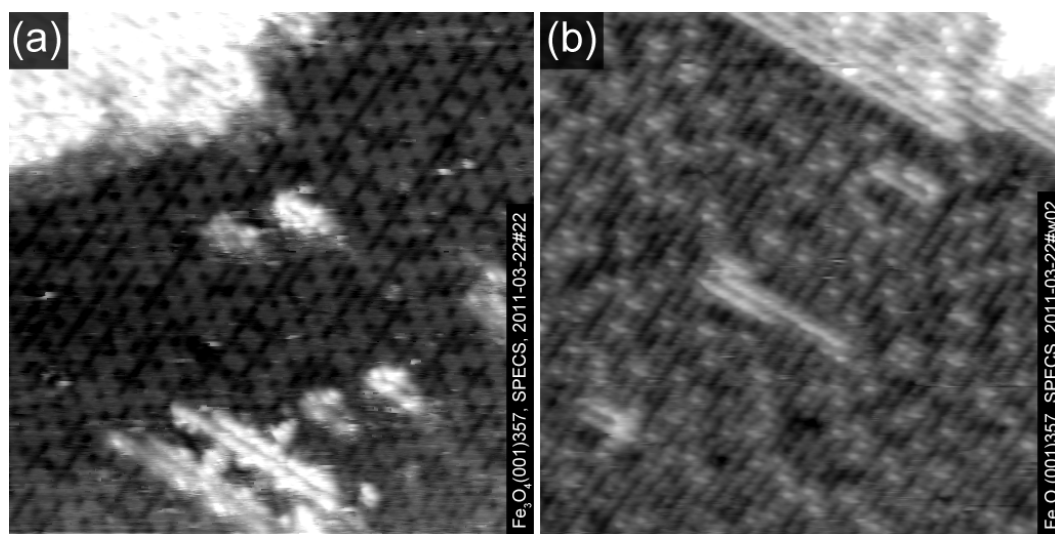


Figure 7.10: (a) STM image of 1.2 ML* Fe deposited at ~ 373 K, and imaged at RT. The surface contains a high coverage of Fe-OP and linear clusters perpendicular to the Fe_{oct} row direction (similar feature better resolved in (b)). Image (b) shows the surface in (a) after dosing 160 L of H_2O at RT. Scanning details: (a) $(20 \times 20) \text{ nm}^2$, $V_s = +0.73 \text{ V}$, $I_t = 0.27 \text{ nA}$. (b) $(20 \times 20) \text{ nm}^2$, $V_s = +0.59 \text{ V}$, $I_t = 0.28 \text{ nA}$.

8 Template-induced adsorption

The understanding of typical surface defects allows us to identify the majority of features typically present on the reconstructed B layer surface. Moreover, we found that all adsorbates probed so far show a strong preference for adsorption in narrow region of the reconstructed unit cell. This is true for atomic H, dissociated H₂O and D₂O, Fe adatoms and Fe-OP. In this chapter, we will demonstrate on two examples (Au and Pd), that the reconstructed Fe₃O₄(001) surface acts as a template for adsorption of metals at RT.

8.1 Au-Fe₃O₄(001)

Prior to this work, there were already two studies of Au adsorption on the Fe₃O₄(001) surface. Using STM, XPS and Mössbauer spectroscopy, Spiridis and co-workers [67] reported that clusters form when Au is deposited onto a Fe₃O₄(001)/MgO(001) substrate at RT. For small Au coverages, they observe small, three-dimensional and positively charged clusters. With increasing Au coverage, the clusters grew in size and became metallic. It should be noted that, in ref. [67], the Fe₃O₄(001) thin film substrate contained a large amount of defects (small terraces, large density of single Fe adatoms), making difficult to interpret data when Au was subsequently deposited. A second published work from Shvets and co-workers [68] reported that the smallest features originating from Au deposition were two-dimensional Au clusters with a diameter of ~0.9 nm and an apparent height of ~100 pm, which adsorbed with the ($\sqrt{2} \times \sqrt{2}$) R45° periodicity on the (001) surface. Moreover, this study showed that these 2D clusters can reside in close proximity, still occupying a single nucleation site.

Motivated by our previous results in which we found that H, H₂O and Fe adsorbed on the reconstructed B layer surface with a strong preference for the narrow site of the reconstructed surface, we decided to reproduce this experiment focussing on the initial adsorption of Au. We use a similar Au coverage as deposited by the Shvets's group in ref. [68], and our largest coverage is similar to the smallest coverage deposited by Spiridis and co-workers in ref. [67]. In our study, we take advantage of our high-resolution STM and our extensive knowledge of the typical surface defects on the (001) surface of magnetite. We observe highly stable, isolated Au adatoms.

8.1.1 Initial Au adsorption

A clean, reconstructed B layer surface with large terraces and a low density of surface defects (OH, APDB's, and, rarely, Fe adatoms; see section 6.2) was used as a starting point. The substrate was always characterized with STM prior to Au deposition.

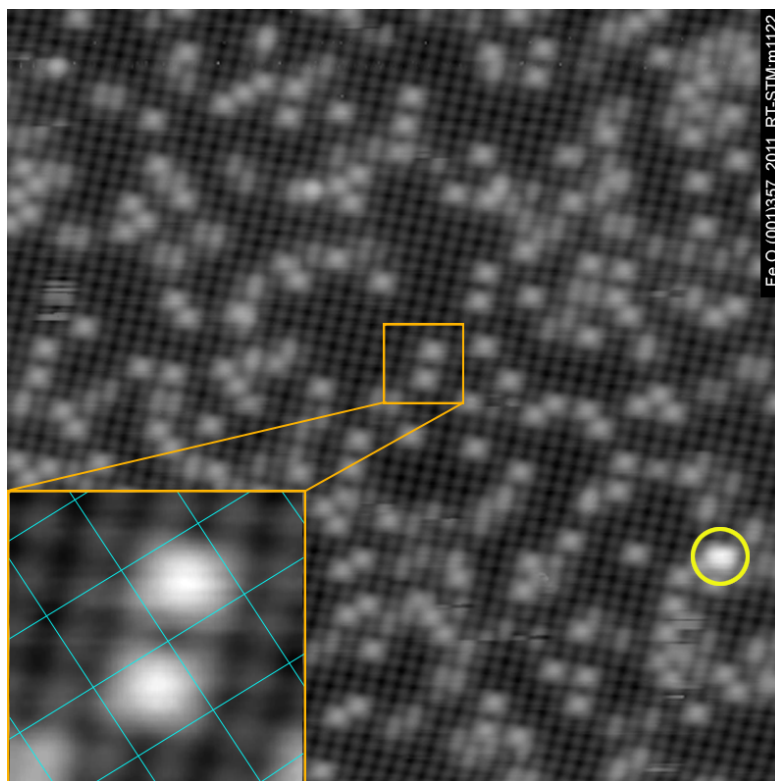


Figure 8.1: 0.12 ML Au deposited at RT. The surface is terminated predominantly with Au adatoms. The density of large clusters is extremely low (the only cluster in this image is encompassed by a yellow oval). The inset shows two Au adatoms in high resolution. The overlay grid in the inset represents the periodicity of the reconstructed surface, with nodes in the center of the wide site. Scanning details: $(30 \times 30) \text{ nm}^2$, $V_s = +1.0 \text{ V}$, $I_t = 0.38 \text{ nA}$.

Figure 8.1 depicts the Fe₃O₄(001) surface after deposition of 0.12 ML of Au at RT. Two types of bright protrusions can be observed on the surface. One of them is the surface OH, as described previously (see section 5.2). This was checked by acquiring time resolved STM movies, where H hopping between two equivalent adsorption positions in the narrow site was regularly observed [34, 51]. After Au deposition the OH concentration is the same as on a clean surface. The second type are bright protrusions with an apparent height of $\sim 100 \text{ pm}$. Two of these are shown in the high resolution inset in figure 8.1. These are ascribed to Au adatoms. There is a good agreement between the density of adatoms obtained by analysis of the STM images (0.12 ML) and a value determined by QCM calibration (0.133 ML). All Au adatoms are located between Fe(B) rows in the narrow site, no Au adatom was ever observed in a wide site. Narrow site occupation is illustrated in the inset of figure 8.1, where the grid overlay, representing the symmetry of the reconstructed surface, has nodes centered in wide sites. Au adatoms are always present in the middle of the cell, therefore they are most probably twofold coordinated

to surface O atoms. Occasional Au clusters are observed on the surface at this coverage (in figure 8.1 one cluster is highlighted by a yellow oval).

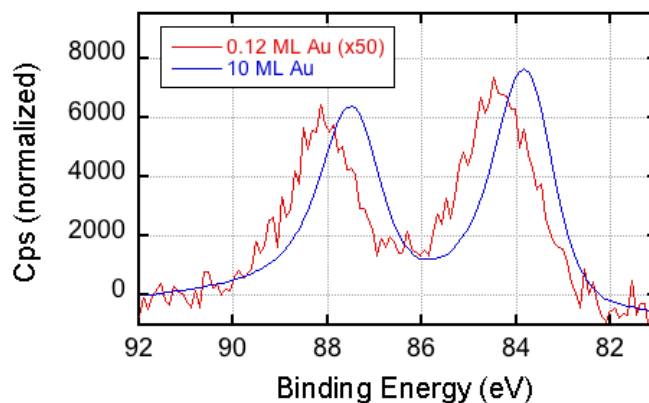


Figure 8.2: Au 4*f* XPS spectra of a surface containing Au adatoms (0.12 ML, red) and for a thick Au film (10 ML, blue). A spectrum of the clean surface was subtracted as a background.

An important point to address is the charge state of gold adatoms. For example, cationic Au nanoparticles are essential for high CO oxidation activity [5] on an Fe₂O₃ catalyst. Therefore, a Au 4*f* XPS spectrum was measured on a surface containing only Au adatoms (0.12 ML Au coverage, red spectrum in figure 8.2). As a reference, an XPS spectrum was also acquired from a thick Au film (10 ML Au, blue spectrum in figure 8.2). A spectrum taken on the clean reconstructed surface was subtracted as a background in figure 8.2, to account for the overlap of the Au 4*f* and Fe 3*s* photoelectron peaks. For the thick Au film, the position of the Au 4*f*_{7/2} peak is consistent with the value of metallic Au (83.85 ± 0.01 eV, FWHM = 1.43 eV) [69]. For the adatom covered surface the peak is shifted towards a higher binding energy to 84.34 ± 0.02 eV (FWHM = 1.69 eV). The spectra in figure 8.2 do not show any significant peak broadening. This confirms that for 0.12 ML Au and also for Au multilayers (representing properties of the bulk Au) most atoms have an equivalent coordination. This is consistent with the STM image of 0.12 ML Au (see figure 8.1), where the majority of Au is adsorbed as adatoms. We will address the charge state of the Au adatoms in the later discussion.

8.1.2 Chemical stability of Au adatoms

The possibility to utilize Au adatoms in heterogenous catalysis requires stability of the adatoms against agglomeration upon exposure to reactive gases. Therefore, exposure to simple gas molecules were tested. We dosed molecular oxygen (600 L dosed at 1.33 × 10⁻⁶ mbar at RT¹). Comparing the before-and-after images does not reveal any change of the surface. We conclude that at low pressures used, O₂ does not change the surface. The second molecule tested was CO. Prior to CO dosing, the surface² consisted of Au adatoms and Au clusters. Dosing 100 L

¹The surface prior to dosing is shown in figure 8.1. After O₂ dosing (image files m1131–m1143) no clear change was observed. Note that the density of Au clusters varied locally, but no measurable loss of the number of adatoms was observed in the STM images.

²0.2 ML Au deposited at RT, post-deposition annealed to 723 K. See image m1417 for reference.

Chapter 8. Template-induced adsorption

at 6.7×10^{-7} mbar at RT and comparing before-and-after images showed again no change. To probe this system at higher pressure conditions, experiments were performed in collaboration with Hao Li, Harald Helmuth Holzzapfel, Christian Weilach, and Guenther Rupprechter³. High pressure (HP) CO exposures were performed on a vacuum system equipped with an XPS and HP cell. A detailed description of the vacuum system can be found in reference [70].

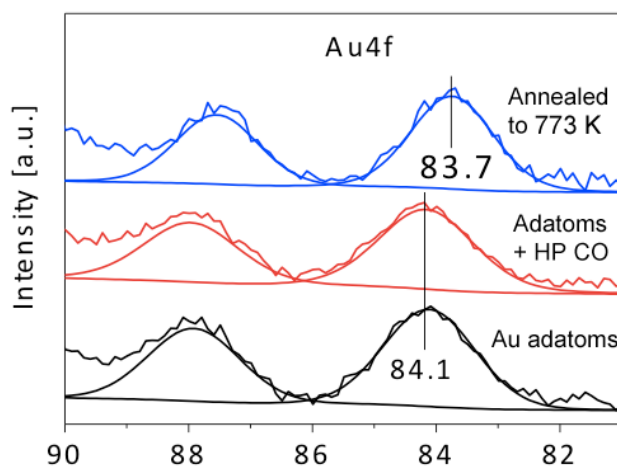


Figure 8.3: Core level Au $4f$ peak after RT deposition of 0.17 ML Au (black). The spectrum shows no change when exposing the system to 1×10^{-4} mbar CO at 96 K for 13 minutes (red). Annealing at 773 K for 5 minutes causes a shift of the core level peak towards lower BE and decrease of the FWHM. The peak positions and FWHM for Au $4f_{7/2}$ are shown in table 8.1. Measurements done by Li Hao, Holzzapfel Harald Helmuth, Weilach Christian, and Rupprechter Guenther.

A coverage of 0.17 ML Au was deposited onto the clean, reconstructed surface at RT and the Au $4f$ core level spectrum was monitored. Figure 8.3 (black) shows the Au $4f$ core level peak after deposition. Compared to figure 8.2, the Au $4f_{7/2}$ peak is located at 84.13 eV (for the surface with Au adatoms only the peak is at 84.34 ± 0.02 eV). Also the FWHM is slightly larger than in figure 8.2; 1.73 eV compared to 1.69 eV. This is caused by a fraction of the Au having a different coordination than Au adatoms, which results in peak broadening and a shift in the core level BE[67]. The vast majority of the Au, however, is in the form of adatoms. After exposing this system to 1×10^{-4} mbar CO at 96 K for 13 minutes and measuring the XPS again (red in figure 8.3), there is no apparent change in the position and shape of the core level peak (see table 8.1). Thus the coordination of Au was not changed after high pressure CO exposure. Since these experiments were performed in an UHV system with no STM, a simple test was performed. This consisted of the annealing at 773 K for 5 minutes. It was found during the investigation of adatom thermal stability shown in figure 8.4, adatom sintering occurs already at 773 K. Extending the annealing time from flash anneal to longer duration⁴ should sinter the vast majority of adatoms and a narrow peak consistent with metallic gold should appear. This was observed and the result is shown in figure 8.3 (blue), where the Au $4f_{7/2}$ peak position is 83.78 eV, indicative of a metallic Au clusters[67].

³Institute of Materials Chemistry, TU Wien.

⁴The UHV system used for HP experiments did not allow for annealing above 773 K, therefore a longer annealing time was used instead of a higher annealing temperature of 873 K.

	BE (eV)	FWHM (eV)
After Au deposition	84.13 ± 0.01	1.73
After HP CO exposure	84.19 ± 0.02	1.72
After annealing	83.78 ± 0.02	1.54

Table 8.1: Results of peak fitting of the XP spectra in figure 8.3(b-d). The table shows the BE and FWHM for the Au 4f_{7/2} photoelectron peak.

8.1.3 Thermal stability of Au adatoms

The surprising observation of stable Au adatoms begs the question at which temperature thermal sintering of adatoms will occur. Therefore the change in the number density of Au adatoms during post-deposition annealing was systematically monitored. Before annealing, the surface contained 0.1 ML of Au adatoms⁵. The result is shown in figure 8.4. The density was monitored by counting the number of adatoms in STM images. Each data point corresponds to a flash-anneal to the selected temperature. After the desired annealing temperature was reached, the sample was immediately cooled down to RT left under UHV conditions.

Up to 673 K (see chart shown in figure 8.4 and corresponding STM image shown in figure 8.5a) the coverage is constant within the statistical error. After annealing at 773 K (figure 8.5b) the number of adatoms drops by 50% of the initial value, and larger clusters appear in the images. Annealing at 873 K (figure 8.5c) leads to sintering of all Au adatoms. Note that the small area (30 × 30) nm² shown in figure 8.5c is not representative of the cluster distribution. Therefore, large scale images following annealing the surface to 773 K and 873 K are shown in figure 8.6.

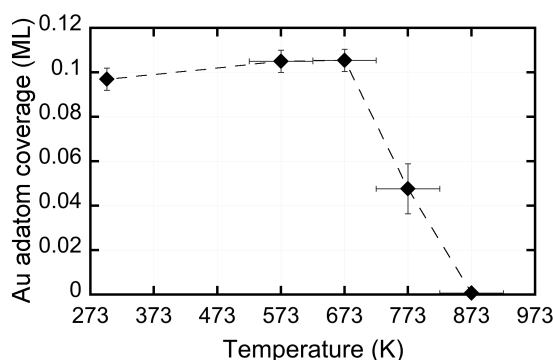


Figure 8.4: Density of Au adatoms as a function of flash-anneal temperature. An initial adatom density of 0.1 ML remains unchanged until 673 K; at higher temperatures sintering occurs.

Up to 673 K, the adatoms are randomly distributed across the surface (see figure 8.5a). After annealing to 773 K (see figure 8.5b), we do not observe any place with high local density of adatoms. When the surface is annealed to 873 K, all Au is clustered, as is shown in figure 8.5c. Large scale images are needed to follow the distribution of clusters. While only a few large

⁵This experiment was done two days after Au deposition. The sample was left under UHV conditions during this time period. Initially the coverage of Au was 0.12 ML deposited at RT (surface shown in image 8.1). The number of adatoms decreased by 0.02 ML.

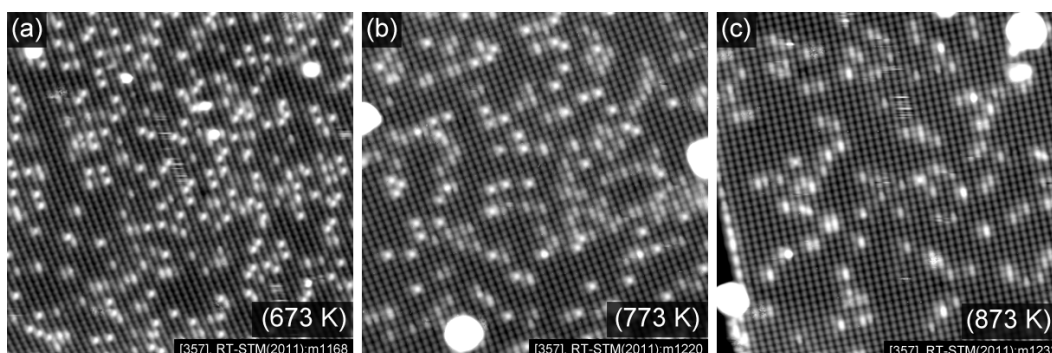


Figure 8.5: STM images showing Au adatoms after annealing to (a) 673 K, (b) 773 K and (c) 873 K. The images highlight the decrease of Au adatoms in favor of clusters; the distribution of clusters is not representative in this small scale area. Scanning details: $(30 \times 30) \text{ nm}^2$, $V_s = +1.2 \text{ V}$, $I_t = 0.3 \text{ nA}$ (all images).

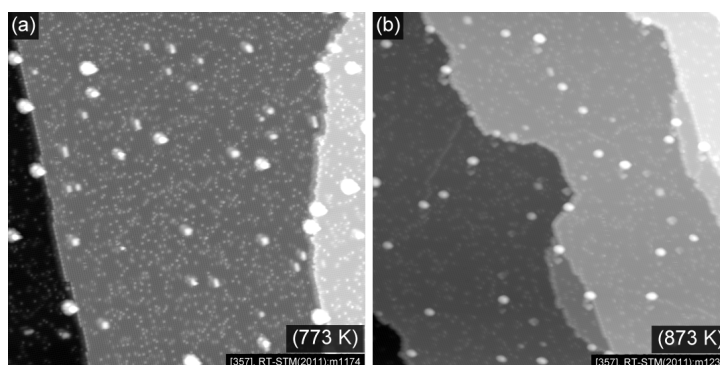


Figure 8.6: Large scale STM images showing 0.1 ML of Au adatoms after annealing to (a) 773 K and (b) 873 K. Three dimensional Au clusters are formed at the expense of Au adatoms. No preferred site for cluster is observed: clusters reside on terraces, as well as on step edges. Scanning details: $(100 \times 100) \text{ nm}^2$, $V_s = +1.2 \text{ V}$, $I_t = 0.3 \text{ nA}$ (both images).

scale images were acquired, the available data for surfaces annealed to 773 K and 873 K (shown in figure 8.6) show that the clusters do not have any preference for adsorption any particular site and are found on terraces and also at step edges.

8.1.4 Higher Au coverage: adatoms and clusters

Figure 8.7 shows a large scale image of a $\text{Fe}_3\text{O}_4(001)$ surface following deposition of 0.4 ML Au at RT. In this image a step edge is present. Au clusters of various sizes are observed immediately after deposition⁶. We observe clusters on terrace, as well as on step edges, with no clear preference for adsorption position. Clusters at step edges are observed on the upper as well as on the lower terrace. In figure 8.7, clusters are divided into three categories based on their apparent height: 300 – 400 pm (green dots), 400 – 600 pm (red dots) and 600 – 780 pm (blue dots). A few of the largest clusters in the image lie out of range (apparent height above

⁶Adatoms are not visible in the image because of the chosen brightness/contrast settings.

780 pm). Since the apparent height of clusters is similar for positive and negative sample bias, we assume that the apparent height represents the real height. A Au fcc bulk interlayer distance is 235.5 pm. The smallest clusters have an apparent height much larger than this value (see figure 8.7), and are also much higher than the Au adatom (100 pm). We conclude that only three dimensional clusters form. An analysis assuming truncated spheres[50] indicates a minimum size of a cluster to be 5 ± 1 atoms[71], with a wetting angle to the oxide substrate of $(51 \pm 0.4)^\circ$ [71].

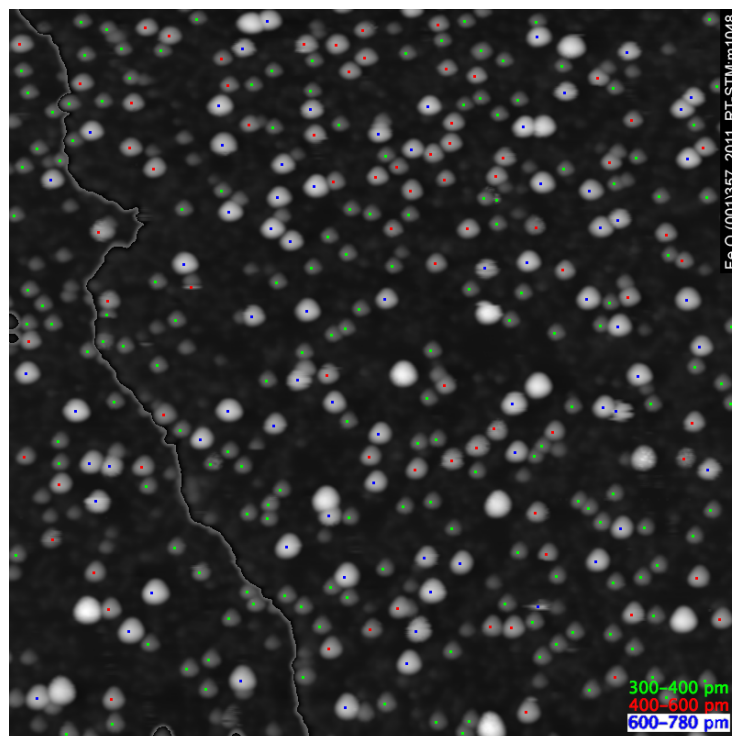


Figure 8.7: Cluster analysis on 0.4 ML Au deposited at RT. A step edge is running from left-top to middle-bottom, the terrace height is subtracted for a clearer visualization of the clusters. The brightness/contrast of the image is set so that clusters are highlighted. Scanning details: $(50 \times 50) \text{ nm}^2$, $V_s = +0.99 \text{ V}$, $I_t = 0.33 \text{ nA}$.

Figure 8.8 shows a smaller area image of the same experiment (0.4 ML Au deposited at RT). The atomically resolved image reveals that out of the total coverage of 0.4 ML Au, 0.16 ML Au is present in the form of Au adatoms. Adatoms are regularly observed in the close proximity to the clusters and form ordered patches on the surface. Smaller clusters occasionally show mobility at RT. This is demonstrated by in figure 8.8, where three selected clusters (highlighted by yellow ovals) moved during acquisition of the image.

The mobility of clusters is expected to be higher at elevated temperatures. This has consequences for the temperature stability of Au adatoms. In the absence of clusters, Au adatoms are thermally stable and do not cluster upon annealing up to 673 K (see figure 8.4). When the surface contains Au adatoms and clusters at the same time, the density of adatoms decreases more quickly, as is demonstrated in figure 8.9. The left part of the chart shows the density

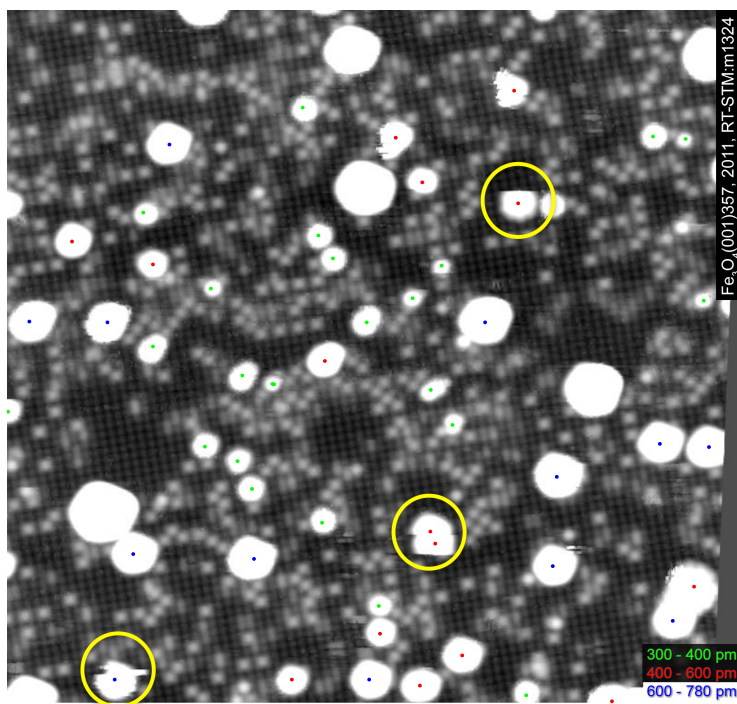


Figure 8.8: 0.4 ML Au deposited at RT. Clusters occasionally exhibited mobility or tip induced interaction during STM acquisition. Three examples in the image are encompassed by yellow ovals. Scanning details: $(50 \times 50) \text{ nm}^2$, $V_s = +1.2 \text{ V}$, $I_t = 0.29 \text{ nA}$.

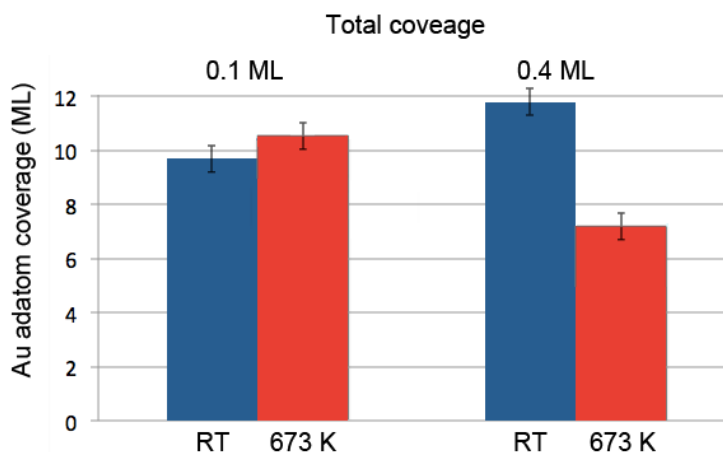


Figure 8.9: Bar chart showing the change in density of Au adatoms after annealing to 673 K. At surface with only Au adatoms and a negligible amount of Au clusters (left, 0.1 ML Au, same dataset as shown in figure 8.4), no sintering occurs up to 673 K. When both, adatoms and clusters, are present on the surface (right, total coverage 0.4 ML Au, where 0.12 ML is in form of adatoms and 0.28 ML in clusters), a significant sintering of Au adatoms is observed upon annealing to 673 K.

of Au adatoms at RT and after a flash-anneal to 673 K for 0.1 ML Au⁷ – a system that was composed mainly of isolated adatoms with almost no Au clusters (another visualization of the same data as shown in figure 8.4). The right side of figure 8.9 shows the density of adatoms before–and–after flash–annealing of 0.4 ML Au deposited at RT. After deposition, 0.12 ML of Au was in the form of adatoms, and the remainder in clusters. We observe a significant drop of the density of Au adatoms after flash-anneal to 673 K. Since no cluster nucleation should occur up to 673 K, the drop in the adatom coverage must be linked to the presence of clusters already at RT. The analysis of before–and–after images reveals that the number of clusters after annealing drops by ~ 30%. As shown below, the mobility of Au clusters plays an important role in the Au adatom sintering, which happens through diffusion and coalescence of the clusters.

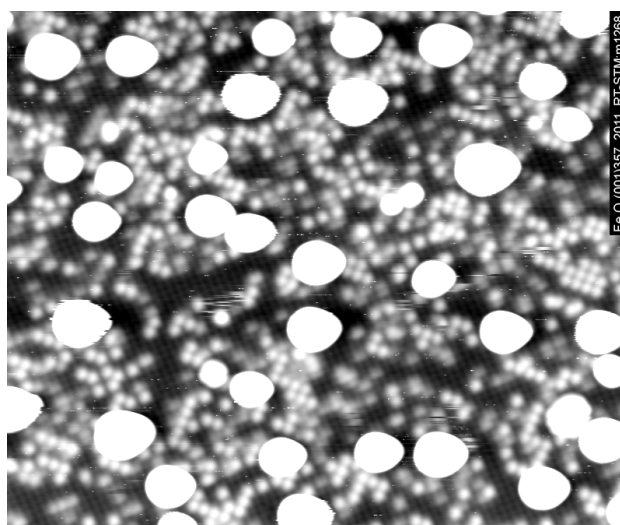


Figure 8.10: STM image of Au deposited at elevated temperature: 0.8 ML Au deposited at 553 K. Scanning details: $(50 \times 41.5) \text{ nm}^2$, $V_s = 1.07 \text{ V}$, $I_t = 0.15 \text{ nA}$.

Up to this point, all Au depositions were performed at RT. We found that Au adsorbs as single adatoms for coverages up to 0.12 ML, at higher coverage Au clusters are formed. To probe the role of temperature during deposition, we have deposited 0.8 ML Au at 553 K (see figure 8.10). Immediately after deposition the sample was cooled down and imaged at RT. The surface contains adatoms and large clusters. Interestingly, the density of Au adatoms is 0.16 ML. When taking into account that a portion of the surface is already occupied by Au clusters, this experiment shows that a slightly larger local density of adatoms compared to deposition at RT was achieved.

⁷As was already mentioned, this system of 0.1 ML Au was composed mainly by adatoms. The density of clusters was negligibly low compared to Au adatoms. This system is resistant against adatom sintering for temperatures up to 673 K. The experiment was performed 48 hours after Au deposition. The sample was left at RT under UHV conditions all the time, and during this 48 hours period the adatom density dropped from initial value of $(0.120 \pm 0.005) \text{ ML}$ to $(0.097 \pm 0.005) \text{ ML}$. Although the role of adsorbates cannot be completely excluded in the sintering process, there is a clear trend that the density of Au adatoms is lower and the remaining clusters are larger in size.

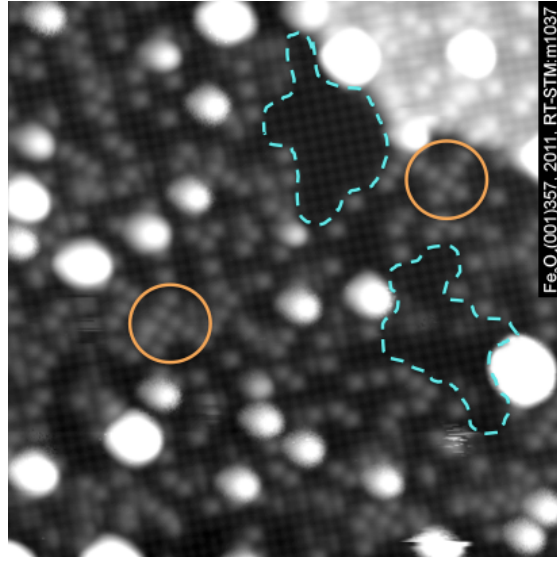


Figure 8.11: 0.4 ML Au deposited at RT. Areas with high local density of adatoms are highlighted by orange circles, areas devoid of adatoms are encompassed by broken cyan lines. Scanning details: $(30 \times 30) \text{ nm}^2$, $V_s = +1.0 \text{ V}$, $I_t = 0.2 \text{ nA}$.

8.1.5 Spectroscopic measurements

Scanning tunneling spectroscopy (STS) is an extension of STM, allowing spectroscopy measurements of the density of states (DOS) for energies close to the Fermi level. The measurement is typically performed at constant tip height, and the tunneling current is measured as a function of bias voltage. It was proposed in ref. [72] that the local DOS (LDOS) of the surface atoms is proportional to I and V following equation (8.1):

$$\text{LDOS} \propto \frac{dI/dV}{I/V}. \quad (8.1)$$

However, in practice the calculation of LDOS according to equation (8.1) is complicated, for reasons discussed in ref. [73]. In point, the tunneling current and its derivative have values close to zero around E_F , and dividing by a value close to zero introduces a large noise in this region. Therefore, equation (8.1) was extended to form (8.2) by introducing a noise factor ϵ , which is caused by the STM electronics.

$$\text{LDOS} \propto \frac{dI/dV}{\sqrt{I^2 + \epsilon^2}/|V|} \quad (8.2)$$

Spectroscopic measurements were performed within the framework of the SCALA software package, provided by the manufacturer of the microscope. dI/dV was obtained by a numerical derivative of the tunneling current by using equation (8.2), with $\epsilon = 4 \text{ pA}$ (a typical noise value in RT-STM system). The calculated LDOS for a clean, reconstructed surface and Au adatoms is shown in figure 8.12.

Figure 8.12 shows the LDOS of the clean surface and Au adatoms acquired with two different tips. The numbers in square brackets in the figure legend indicate the filename of the analyzed

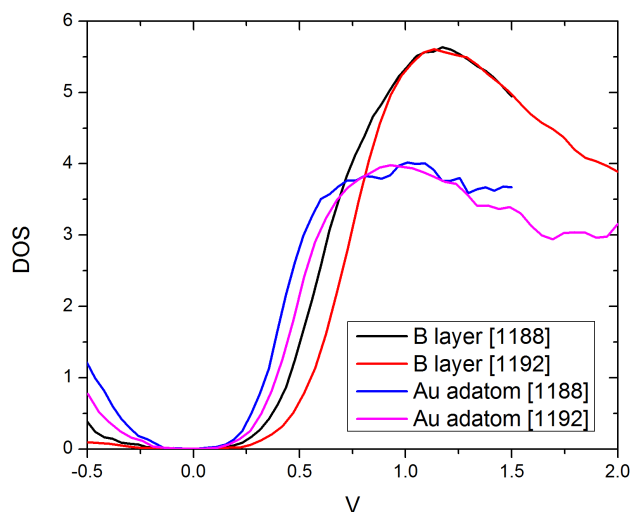


Figure 8.12: LDOS for a clean B layer and for Au adatoms, calculated using equation (8.2), and obtained with two different STM tips. In the legend, the filename of the image (RT–STM, sample 357, 2011) is indicated. In case of picture m1188 STS spectra over 3 Au adatoms were averaged, for image m1192, nine were averaged.

image (RT–STM, sample 357, 2011). I–V spectra (80×80 points) were acquired together with a topographical image. In image m1188 STS spectra over 3 Au adatoms were averaged and in case of image m1192 STS I–V spectra from 9 Au adatoms were averaged. In case of empty states the calculated LDOS is similar to a reported LDOS determined the DFT [39]. In case of Au adatoms, there is an additional state at $\sim +0.6$ eV.

8.1.6 Discussion

An important question is the determination of the state of Au adatoms. In figure 8.2, we showed an XPS spectrum for a surface covered with Au adatoms. Compared to bulk gold, we observed a Au $4f_{7/2}$ core level peak shift towards higher BE. This shift can have its origin in either an initial state or final state effect. In case of an initial state effect, the charge of the atom prior photoemission plays the main role in the magnitude of the BE shift. The amount of the shift is dictated by the number of bonds with more electronegative atoms. In STM, we see the Au adatoms in the center of the narrow site. Therefore, the atom has to be bound to two oxygen atoms. O has a larger electronegativity than Au (3.44 and 2.54, respectively). Therefore, the initial state arguments support the observed BE shift. However, a final state effect [69] can also influence the BE peak position. The work done by Giordano and co-workers [74] showed that the orientation of the surface dipole may be an additional factor influencing the direction of charge transfer. Using STM, STS and DFT calculations, they demonstrated that a metal substrate with a high work function, a reducible oxide, and the oxide surface dipole moment that favors charge flow into the support are requirements for positively charged adatoms. All these requirements are fully met by the reconstructed B layer surface. DFT+U

calculations indicate e^- transfer from Au adatom to the surface (private communication with Peter Blaha and Rukan Kosak). Based on this evidence, we conclude that Au adatoms are positively charged.

We never observed Au dimers, trimers or tetramers at RT. Therefore, these features are unstable configurations at RT. On the other hand, we do observe small Au clusters. This is indicative that a critical number of Au atoms is needed to form a stable, small cluster. Note that areas of clean surface, devoid of Au adatoms, are regularly observed right next to large clusters (see figure 8.11). Based on this observation we propose a model of cluster nucleation when Au is deposited on the $\text{Fe}_3\text{O}_4(001)$ surface at RT.

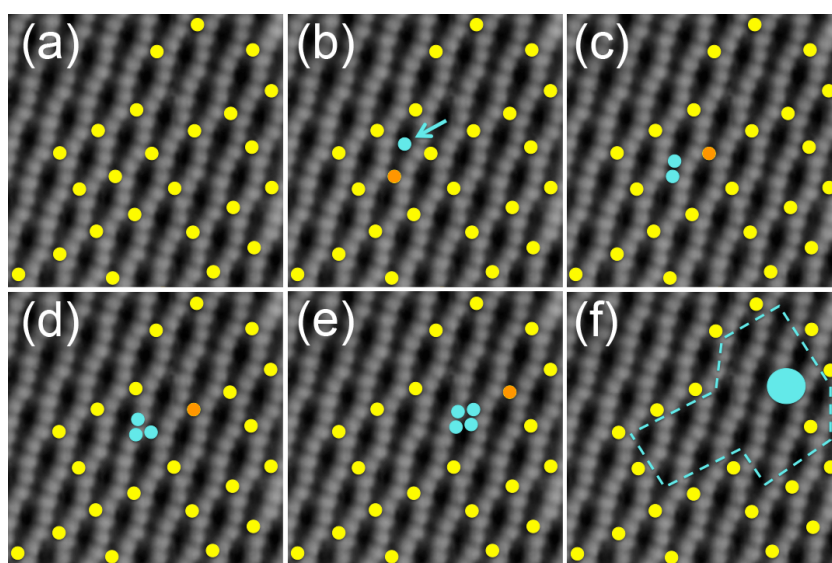


Figure 8.13: Proposed model of Au cluster nucleation: Au adsorbs on the surface and is stabilized on a narrow site. A high local density of stable adatoms is eventually formed. This is represented by filled yellow circles in part (a). The atom drawn in orange is important in the next step. When additional Au adsorbs in a place with no available narrow site (filled cyan circle in part (b)), then a mobile Au dimer (between cyan and orange atom) is formed (c). The Au dimer diffuses on the surface, forming a trimer (d), a tetramer (e), and this process continues until a critical size is reached and a stable cluster is formed on the surface, surrounded with an area free of adatoms, as highlighted by broken cyan line in part (f).

During Au deposition, a Au atom arrives from the gas phase, lands on the surface, and diffuses a short distance, before it is trapped in a neighboring narrow site. Octahedral pairs of Au were never observed, in contrast to octahedral pairs of Fe (see section 7.1.2). With increasing coverage, ordered patches with a high local density of adatoms are created (see areas highlighted with orange ovals in figure 8.11, where the local coverage approaches a full narrow site occupancy). Such an area is also shown in a schematic model in figure 8.13a. Stable adatoms are represented by filled yellow circles. From the experiments, it is known that Au adatoms are strongly bound within the narrow site, as is demonstrated by the lack of mobility at RT and the high stability of adatoms against thermally-induced sintering. As the coverage is increased, a Au atom must eventually arrive on an area with a high local density of adatoms, where there is no available free narrow site. This situation is represented by a filled cyan circle in figure 8.13b. The Au atom, rather than adsorbing in a wide site, interacts with one of the

adsorbed adatoms and forms a Au dimer (figure 8.13c). Since Au dimers were never observed at RT, we propose that the Au-(Au adatom) complex destabilizes the Au adatom (orange in the model) and a mobile Au–dimer is created. This dimer diffuses, and grows through encounters with more Au adatoms, forming a Au trimer (d), tetramer (e) etc., until the stable cluster size of 5 ± 1 atoms^[71] is reached. This is schematically shown in figure 8.13f. This model, termed a “rolling snowball” mechanism, explains the asymmetric trails of adatom free areas close to Au clusters (areas highlighted by cyan color in figure 8.11).

We propose that formation of Au clusters during Au deposition differs from cluster nucleation when the surface was annealed above 673 K. The cluster formation could possibly be linked to the loss of surface reconstruction when the surface undergoes the surface Verwey transition. The surface Verwey transition for the single crystal used is 723 K (private communication with Juan de la Figuera), which is in good agreement with figure 8.4. Once the reconstruction disappears, Au adatoms are no longer stabilized by the surface and they cluster, as is typical for Au on most oxide surfaces. A sintering of adatoms at high temperatures is driven by two processes: cluster nucleation and cluster growth.

8.1.7 Conclusion

The initial adsorption of Au was systematically investigated. We have found that Au adsorbs as single adatoms when deposited at RT. We propose that the clusters are formed during deposition when a Au atom lands in an area with a high local density of adatoms and no neighboring narrow site is available. This leads to formation of a mobile Au–dimer, which diffuses rapidly along the surface, picking up other adatoms, until a critical size necessary for the smallest stable cluster is reached. From the size of the smallest cluster observed, we estimated the critical nucleus size as 5 ± 1 atoms. Clusters can be also formed by annealing the surface above 673 K. Once a cluster is formed, it is mobile even at room temperature. Likely, sintering of the Au adatoms occurs through migration and coalescence of clusters. At elevated temperature the mobility of clusters is enhanced and the sintering process is accelerated.

8.2 Pd-Fe₃O₄(001)

Palladium (Pd) belongs to the group of elements referred to as a platinum group metals (palladium, platinum, rhodium, ruthenium, iridium, and osmium). Together with its related chemical element platinum, these are heavily used in automotive three way converters, where they are used for converting hydrocarbons, CO and NO_x into less harmful substances. Clusters of Pt group metals on selected metal–oxide support are used in other heterogeneous catalysts as well: for example in the CO oxidation with O₂ and NO [75] or the catalytic combustion of methane [76]. Recently, it was reported that large metallic Pt–group clusters act as a spectator in the ceria–based WGS catalysts [21], and only small non–metallic nanoparticles and adatoms are the active sites [20, 21]. If the active species in a catalytic reactor were only single adatoms of the Pt–group elements, then the amount of the metal needed would decrease considerably, resulting in substantial cost savings.

Motivated by the observation of single and thermally stable Au adatoms on the clean reconstructed Fe₃O₄(001) surface, the adsorption of small amounts of Pd at RT was investigated. Pd adsorbs also as adatoms for sub-monolayer coverages. In contrast to Au adatoms, which are inert towards CO, Pd adatoms react strongly with CO. The adsorbed molecule makes the adatom mobile and facilitates agglomeration into clusters.

Typically, single adatoms in a catalyst are studied with an aberration–corrected scanning transmission electron microscope (STEM) using a high electron energy to achieve a high lateral resolution. Many experimental and theoretical reports demonstrate that a high–energy electron beam is capable to induce adatom mobility and electron–induced sputtering [77, 78, 79, 15]. From this reason, most of the results related to single adatoms are highly controversial in the community using STEM microscopes. On the other hand, we used STM to study Pd adsorption on an atomic level and saw no signs of a measurement–induced adatom mobility. To the author, STM seems to be an ideal tool to study single adatoms.

8.2.1 Sub–monolayer Pd coverage: Pd adatoms

As with Au experiments, a clean reconstructed B layer surface was used as a starting point and the substrate was always characterized with STM prior to the deposition. Figure 8.14 shows nominally 0.2 ML of Pd deposited at RT. In addition to the typical surface defects already described (surface OH [51] and APDB [52]), four features can be identified on the surface. First, there are single protrusions, which correspond to Pd adatoms (three of them highlighted by an orange oval) are observed. The Pd adatoms have apparent height of ~120 pm. This value is ~50 percent larger than the height of occasionally–present Fe adatoms⁸. Pd adatoms prefer the narrow adsorption sites. Similarly to Au they form ordered arrays on the surface. Second, we observe three dimensional Pd clusters (one highlighted with yellow circle in figure 8.14) with varying sizes, with a density⁹ of 0.019 clusters per nm². Third, features with an apparent height of 270 pm (one of them is marked with a red cross) can be observed. These features have an apparent height larger than a Pd(111) fcc interlayer distance (224.6 pm), but as will be experimentally shown below, these are not Pd clusters, but a Pd atom that is trapped at a surface OH. Finally, we observe a small number of “fuzzy” features (blue circle, an Pd–carbonyl trapped at Pd adatom, as identified later in the text).

⁸The apparent height of Fe adatom is ~80 pm.

⁹Analysis of image Fe₃O₄(001)357, 2012, RT-STM:m10049.

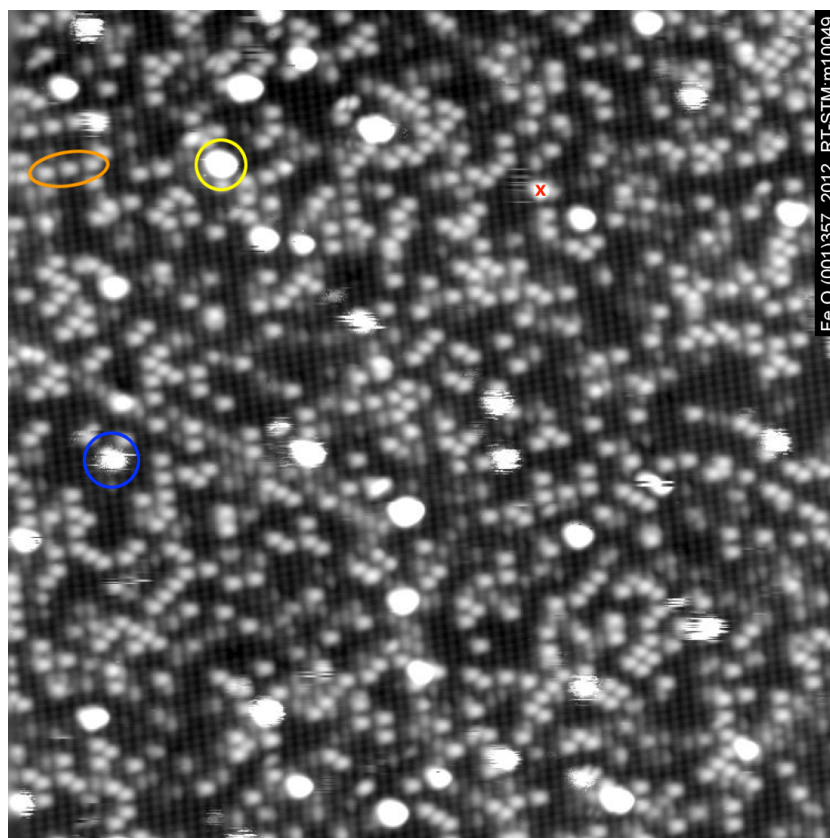


Figure 8.14: Nominally 0.2 ML of Pd deposited at RT. In the image, four kinds of features resulting from Pd deposition are present: Pd adatoms (three of them highlighted by an orange oval), Pd clusters (yellow circle), and two features that will be identified later in this chapter. These include a “fuzzy” appearing feature (one encompassed by a blue circle), the other one is a cluster-like feature with an apparent height of 270 pm, highlighted by a red cross in the figure. Scanning details: $(50 \times 50) \text{ nm}^2$, $V_s = +1.2 \text{ V}$, $I_t = 0.3 \text{ nA}$.

This first Pd deposition was performed when the e-beam evaporator was not properly out-gassed. The maximum pressure during deposition was 1×10^{-9} mbar. Therefore, the experiment was repeated by depositing 0.2 ML Pd at RT (maximum pressure during deposition was in the low 10^{-10} mbar range). The sample was left under UHV conditions (pressure under 6×10^{-11} mbar) at RT and a series of images was acquired. These are displayed in a time resolved STM movie (available online [80]). The same area on the surface was monitored for a time period of 5 hours and 20 minutes. Surprisingly, the density of clusters immediately after the second Pd deposition¹⁰ was 0.015 clusters per nm^2 , a value lower than found for the first Pd deposition (0.019 clusters per nm^2 , see figure 8.14). 12 hours after deposition the density of clusters had doubled¹¹ to 0.03 clusters per nm^2 . Although the Pd adatoms are strongly bound within the narrow sites of the clean reconstructed Fe₃O₄(001) surface, some mobility is observed at RT. Figure 8.15 shows four selected frames from movie [80], where a small region of interest (highlighted with a white frame in movie [80]) was selected from the $(50 \times 50) \text{ nm}^2$

¹⁰Analysis of image Fe₃O₄(001)357, 2012, RT-STM:m10215.

¹¹Analysis of image Fe₃O₄(001)357, 2012, RT-STM:m10335.

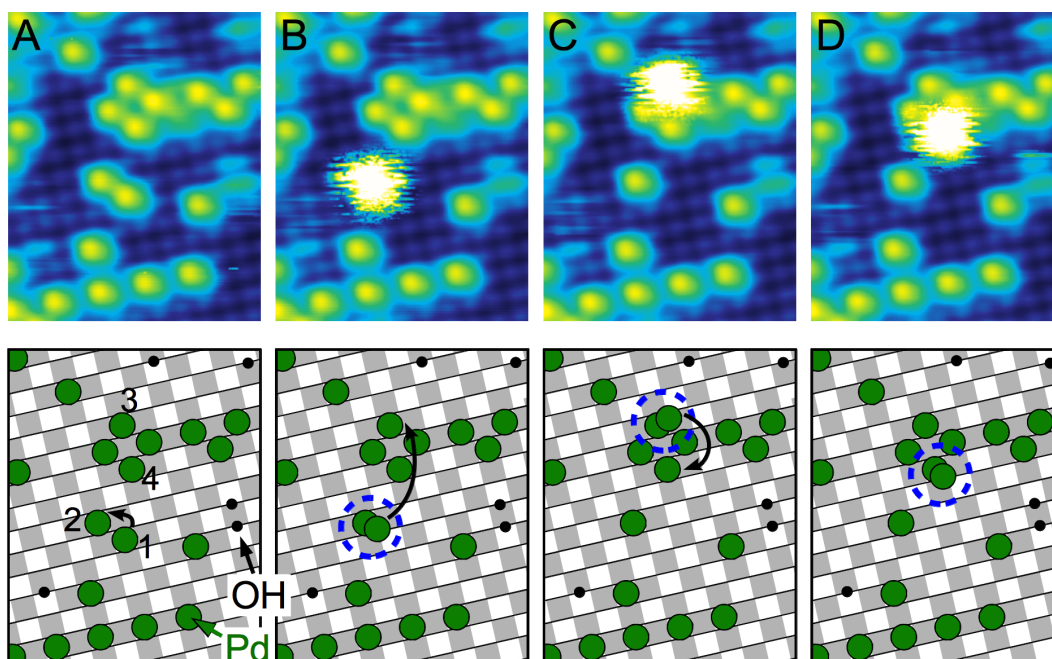


Figure 8.15: Adsorbate induced mobility of one Pd adatom. Four frames (a–d) are selected from an STM movie [80]. The schematic below each frame shows the motion of adatoms on the surface. Between frame (a) and (b), a CO molecule adsorbs on Pd(1). Pd–CO becomes mobile and moves on top of Pd(2), forming a “fuzzy” feature. Between frames (b–c), Pd(1) moves from Pd(2) onto Pd(3), leaving the Pd(2) behind at its initial position. The same process happens between frames (c–d), when Pd(1) moves from Pd(3) onto Pd(4). (Scanning details: $(6.5 \times 8.5) \text{ nm}^2$, $V_s = 1 \text{ V}$, $I_t = 0.2 \text{ nA}$. Image details: $\text{Fe}_3\text{O}_4(001)357$, 2012, RT-STM:m10299, m10304, m10308, m10310). Acquisition time of one image is ~ 4 minutes.

area of the STM movie. The schematic model below each frame highlights what happened between the STM images. For the first 50 frames of the movie (corresponding to a time span of 3 hours and 20 minutes), the surface looks identical to figure 8.15a. Then, in frame 51 (figure 8.15b), adatom Pd(2) is replaced with a bright “fuzzy” feature with an apparent height of $\sim 230 \text{ pm}$, while Pd(1) disappears. Since there is no other change in the vicinity (tens of nanometers), the new “fuzzy” feature must contain both Pd(1) and Pd(2). The appearance of this feature is a consequence of its mobility while it is scanned with STM tip. This is also an indication of weak binding to the surface. More evidence will be provided later that this “fuzzy” feature (see also figure 8.14, blue circle) is linked to a CO molecule adsorbed on Pd(1) and subsequent formation of a Pd–carbonyl complex. The Pd–Pd–CO entity is not a stable feature; a few frames later (frame 55, figure 8.15c) the Pd–carbonyl jumps to Pd(3), leaving Pd(2) behind. Finally, figure 8.15d shows a similar event, where the Pd–carbonyl hops from Pd(3) to Pd(4).

The region selected in figure 8.15 represents an event where adsorption of one CO molecule takes place within 5 hours and 20 minutes. Several other events of CO adsorption on Pd adatom were observed in movie [80]. With the low pressure in the UHV chamber (below $6 \times 10^{-11} \text{ mbar}$) CO adsorption on Pd adatoms was an extremely rare event. Only one adatom

becomes mobile as a consequence of CO adsorption in the selected region [80]. This indicates that only one CO molecule is necessary to initiate the process. The Pd–Pd–CO entity decays within several minutes, a long enough to image it as the “fuzzy” Pd–CO. After the decay, Pd–CO can travel over large distances, before it gets trapped by another Pd adatom, as observed in figure 8.15.

The concept of adsorbate induced mobility of adatoms is not new. A similar process was observed previously by Horch et al.[81]: the adsorption of H on a Pt adatom on Pt(110) resulted in a complex species with a very low barrier for diffusion. In case of Pd/Fe₃O₄(001), the mobility and cluster formation is linked to CO, as evidenced by: a) worse vacuum results in more clusters and less adatoms with the same coverage, and (b) occasionally induced mobility happened very rarely in UHV and was always linked to a “fuzzy” appearance of a mobile Pd atom.

To test this hypothesis a surface with nominally 0.2 ML of Pd adatoms was exposed to > 100 L of CO at RT. The surface prior oxygen dosing is shown in figure 8.16a (another area of the same experiment already shown in figure 8.14). Prior to CO exposure, four features were present

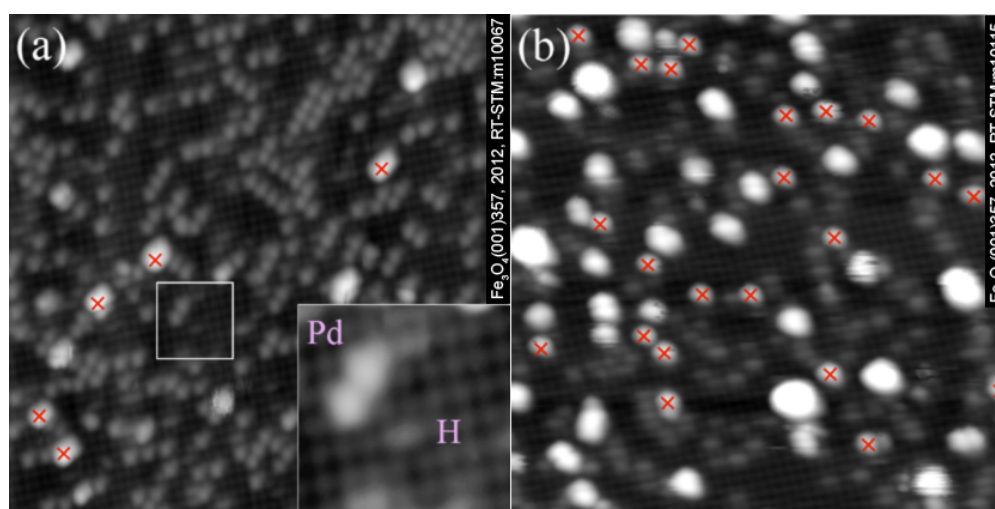


Figure 8.16: The effect of CO exposure on Pd adatoms. (a) STM image after deposition of nominally 0.2 ML Pd at RT (another area of the same experiment as shown in figure 8.14, with the same features present on the surface). After exposure to 100 L of CO at RT, all Pd adatoms have disappeared. Many large clusters have formed, as well as features marked with a red cross, which are identified later in figure 8.18. Scanning details (both images): (30 × 30) nm², V_s = +1.2 V, I_t = 0.3 nA.

in figure 8.16a: Pd adatoms, “fuzzy” appearing Pd–carbonyls, Pd clusters and features marked with red cross. After dosing CO (> 100 L), not a single Pd adatom or Pd–carbonyl remained on the surface (see figure 8.16b). The only remaining species are Pd clusters of varying sizes and the features labeled with the red cross. Their number density increased ~4×. The experiment presented in movie [80], together with experiment shown in figure 8.16 provide strong evidence that CO, the major constituent of the UHV residual gas, leads to cluster formation and growth in the Pd/Fe₃O₄(001) system.

To follow the CO–induced growth of clusters, an STM movie was recorded. After a few frames acquired the initially low CO partial pressure is increased from below 5 × 10⁻¹¹ mbar

Chapter 8. Template-induced adsorption

to 5×10^{-10} mbar¹². The first frame of the movie (0.2 ML Pd deposited at RT, containing the typical features already described) is shown in figure 8.17a. The time duration of the movie is 1 hour 55 minutes. The movie is available online [82]. Two regions of interest are

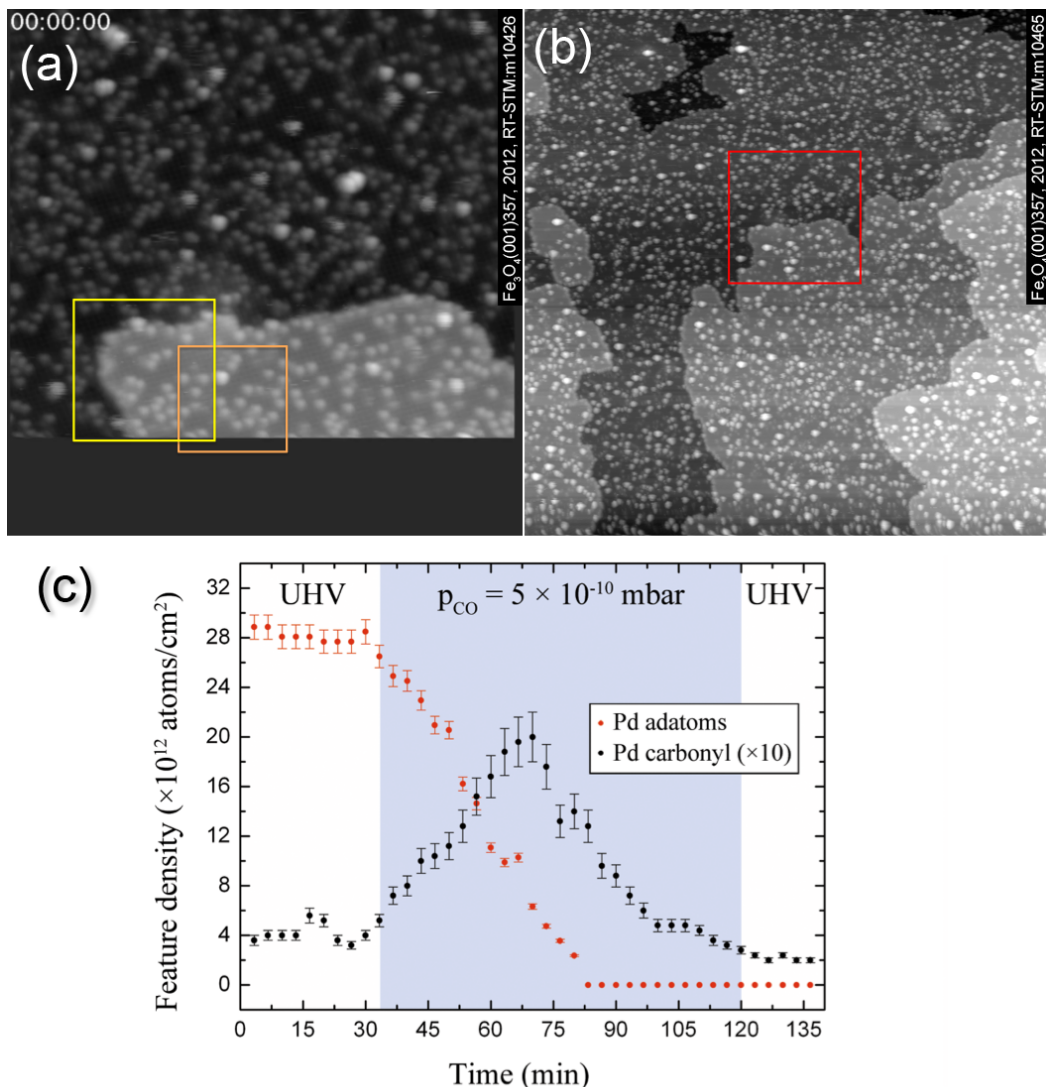


Figure 8.17: Overview of an STM movie [82]. (a) The first frame of the movie (0.2 ML Pd deposited at RT prior to the CO dosing) is shown. Two regions of interest are highlighted. (b) A large area STM image showing the surface directly after acquisition of movie [82]. The area scanned during the acquisition of the movie [82] is highlighted with a red frame. Scanning details: (200×200) nm², $V_s = +1$ V, $I_t = 0.3$ nA. (c) The chart shows the number of adatoms and of Pd-carbonyls throughout the movie.

¹²CO dosing was done via the preparation chamber in the RT STM system using a high precision leak valve. Pressure reading in the STM chamber during experiment will result in noise in STM, therefore a calibration was done prior to experiment with QMS and pressure gauges, which are present in both chambers, with the open gate valve between the chambers. During the experiment, the pressure gauge and QMS in STM chamber were switched off. The pressure was set up using the QMS and pressure gauge in preparation chamber.

highlighted with yellow and orange frames, respectively, and will be subsequently analyzed in detail. The possibility of a tip-induced interaction have to be considered. For example, on TiO₂ an interaction between the STM tip and Au nanoparticles was observed at elevated temperatures [83]. In case of agglomeration Pd adatoms into clusters, the observed “sintering” process is clearly not affected by the measurement. This argument is based on figure 8.17b, which shows a large scale image with an area highlighted by yellow color, representing the area where STM movie [82] was acquired. Pd cluster density, size and distribution do not differ between areas measured for extended period of time and the surrounding.

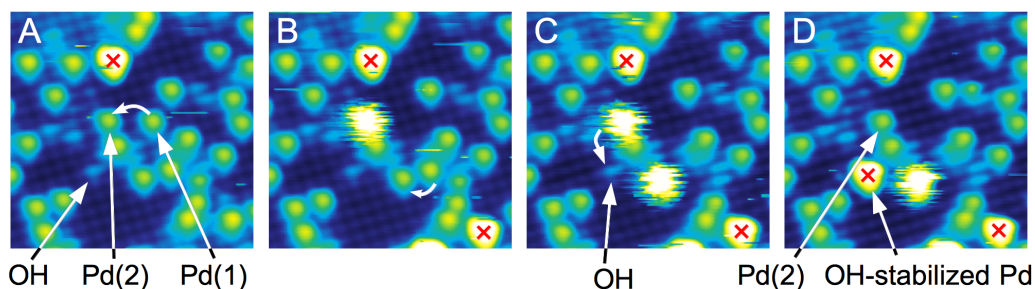


Figure 8.18: Formation of a mobile Pd carbonyl group and a stable Pd adatom at a surface OH. Consecutive STM images selected from movie [82] (orange area in figure 8.17). Frame (a) shows the surface after 0.2 ML Pd deposition at RT. Then, the CO partial pressure was increased to 5×10^{-10} mbar and left at this value for the rest of the movie. In frame (b), adatom Pd(1) forms a Pd-carbonyl group and hops to Pd(2), forming a bright fuzzy feature. In frame (c), a second mobile Pd carbonyl group was formed. Finally, in frame (d), the Pd(1) carbonyl group hops to a surface OH and forms H-stabilized Pd, marked with a red cross in the image. (Scanning details: $(10 \times 10) \text{ nm}^2$, $V_s = +1 \text{ V}$, $I_t = 0.2 \text{ nA}$. Image details: Fe₃O₄(001)357, 2012, RT-STM:m10426-m10460, movie duration 1 hour 50 minutes.)

The movie allows us to identify and understand two of the features frequently seen after deposition of Pd: the mobile “fuzzy” appearing Pd and the feature that has been hitherto marked with a red cross. Figure 8.18 shows four selected frames from the orange area of interest (see figure 8.17 and corresponding movie [82]). Frame (a) was acquired immediately before CO exposure. The surface contains mainly Pd adatoms, surface OH’s and one feature marked with a red cross. After CO is introduced to the background pressure (b), a Pd(1) disappears and a Pd-carbonyl is observed on top of a Pd(2) adatom. In frame (c), another Pd-carbonyl is formed. In (d) a Pd(1)-Carbonyl, which was atop of Pd(2) in frame (c) interacts with a surface OH and forms a feature till now marked with a red cross (Pd-OH). The same behavior was observed also outside the selected area and the analysis of both STM movies [80, 82] reveals that the Pd-OH is immobile at RT. OH has therefore the opposite effect than CO and can freeze the mobility of a Pd-carbonyl.

The interaction of CO with Pd was simulated with DFT using GGA+U calculations¹³. Simulation details are found in [55]. The results of DFT calculations are shown in figure 8.19. In (a), a Pd adatom was placed into the oxygen bridging site (narrow site), as observed experimentally. The Pd adatom adsorbs with a high adsorption energy of 2.5 eV, a formal charge of $+0.6 e^-$ and

¹³Simulations were performed by Prof. Peter Blaha and Rukan Kosak, as part of a collaboration on the joint publication [55].

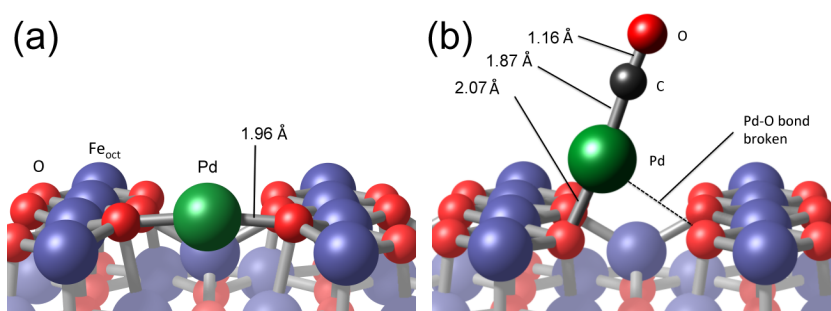


Figure 8.19: Relaxed geometry obtained from *ab-initio* GGA+U calculations showing (a) a structural model of a Pd adatom added to the bridging oxygen site within the (initially) narrow region of the reconstructed surface unit cell (see figure 2.3a). (b) Pd adatom after adsorption of a CO molecule.

magnetic moment of $0.07 \mu_B$. According to DFT, when a CO molecule approaches a Pd adatom (figure 8.19b), one Pd–O bond is broken and the other one weakens and increases its length to 2.07 \AA . CO attaches strongly to Pd, but weakens its internal bonding as the C–O distance increases to 1.16 \AA . The energy gain from this process is 1.5 eV . The DFT+U calculations show that, upon CO adsorption, the Pd atom keeps its initial magnetic moment, but reaches a neutral charge state.

8.2.2 Formation of Pd clusters

The formation of Pd clusters was directly observed in an STM movie [82] during CO exposure. In Figure 8.20 we show four selected frames from this movie (yellow area of interest highlighted in figure 8.17). Initially, the surface contained predominantly isolated Pd adatoms and surface OH, where one of the OH resulted into a Pd–OH species in frame (a). Then the surface shown in (a) was exposed to CO and an image recorded after 15 minutes of a CO exposure (b). As a result of a CO exposure, seven Pd–carbonyl species have formed. Five of them reside on another Pd adatom (“fuzzy” appearance), the remaining two have diffused to surface OH groups. Note that three Pd–carbonyl species are in close proximity to each other in the left side of frame (b). In the next frame (c), a cluster has formed at the expense of these three previously mentioned Pd–carbonyl species (including their host Pd adatoms) and four of the nearby Pd adatoms. In frame (d), the large cluster has diffused by a distance of 6 nm to an Pd–OH, picking up a Pd–carbonyl and its host adatom along the way. Since we can track almost all adatoms over the course of the movie, it is possible to determine the size of the large Pd cluster in the end of the movie to contain between 15 and 19 Pd atoms. The uncertainty is caused by adatoms close to step edges, whose final destination is harder to determine unambiguously.

On oxide surfaces, clusters typically nucleate at nucleation sites on the surface. These are typically oxygen vacancies, step edges, domain boundaries and other defects [10, 11, 12]. This is called heterogeneous nucleation. In case of Pd clusters, nucleation of clusters has no preferential nucleation sites, as is demonstrated in figure 8.20. In contrast to what is expected for oxide surfaces, we report an example of homogeneous nucleation of clusters. A cluster is formed when at least 3 Pd–CO species meet at close proximity to each other. Moreover, cluster

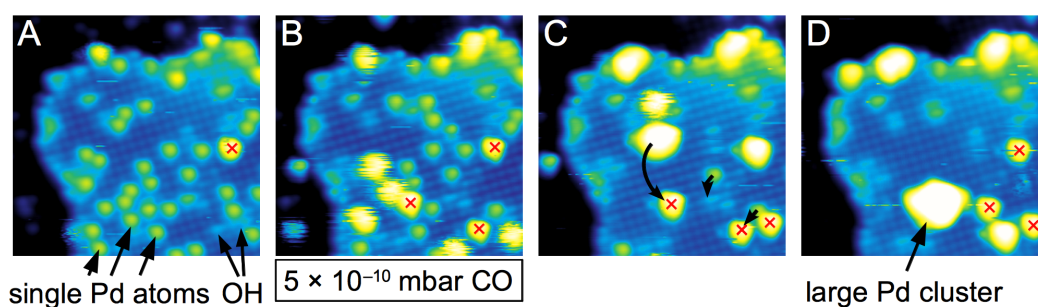


Figure 8.20: CO induced formation of a large Pd cluster. Consecutive STM images selected from movie [82] (yellow area in figure 8.17). After deposition of 0.2 ML Pd at RT, as shown in frame (a), only Pd adatoms, surface OH's and one H-stabilized Pd atom are present. Then the CO partial pressure was increased to 5×10^{-10} mbar and left at this value for the rest of the movie. Frame (b) shows the surface after 15 minutes of CO exposure; several mobile Pd carbonyl groups and H-stabilized Pd have formed. Shortly afterwards, three mobile Pd carbonyl groups and four Pd adatoms form a large cluster, shown in frame (c). Frame (d) shows the surface 25 minutes later; the cluster has captured another mobile Pd carbonyl group and diffused to merge with a H-stabilized Pd atom. Scanning details: $(14 \times 14) \text{ nm}^2$, $V_s = +1 \text{ V}$, $I_t = 0.2 \text{ nA}$. Image details: Fe₃O₄(001)357, 2012, RT-STM:m10426-m10460 (movie duration 1 hour 55 minutes).

growth is facilitated through cluster mobility in movie [82], not via Ostwald ripening, as is commonly believed [14].

8.2.3 Additional considerations

In the Master's thesis of G. Argentero [71] it was mentioned that a small percentage of "Pd" adatoms occupy also a wide site. However, this wide site occupancy was more frequent in the very first experiment (5% of adatoms¹⁴), and the adatoms in the wide sites had an apparent height in the range between 60 and 140 pm. With further experiments, when the e-beam evaporator was better outgassed, the number of adatoms observed in wide adsorption sites dropped down to zero¹⁵. The adatoms occupying wide sites were probably caused by impurities of unknown origin, originating from the not properly outgassed evaporator. We conclude that for submonolayer Pd coverages, Pd adsorbs on the reconstructed B layer surface in form of adatoms, where the strongly preferred adsorption site is the narrow site of the reconstructed surface unit cell.

Second, in ref. [71], hopping of Pd adatoms between neighboring narrow sites was occasionally observed. This process can be caused by two possible mechanism: either the adatom was released from its hosting narrow site by thermal excitation, or the adatom was lifted by an adsorbed CO molecule, which was shortly afterwards desorbed from the adatom.

In contrast to Au, the investigation of thermal stability of Pd adatoms will be strongly affected by the fact that heating the sample will be inevitably linked to formation of CO. Nevertheless, a preliminary test of heating of the sample with Pd adatoms was done and despite a bad STM

¹⁴Analysis of image 2012, RT-STM, m10046.

¹⁵Analysis of image 2012, RT-STM, m10313.

tip and therefore poor lateral resolution, there is an indication that a Pd ferrite structure can be created by heating the surface to temperature ~ 573 K (STM images of post-deposition annealed surface can be found on page 82 in [71]).

Finally, the reactivity of Pd adatoms with gases other than CO was also conducted. O₂ dosing included two experiments (100 L and 1000 L at RT performed on 28. May and 6. June 2012, respectively). Unfortunately, these two experiments gave no clear result because of the ill defined surface (100 L experiment) and a bad STM tip (1000 L experiment). Interaction with H₂ was performed with a surface containing small Pd clusters only (no adatoms). After dosing 10 L H₂ at RT no clear change of the surface was observed.

8.2.4 Outlook

The investigation of Pd adsorption in this study [55] was limited to sub-monolayer coverage: a fixed coverage of 0.2 ML was chosen. Agglomeration of Pd adatoms into clusters was linked to the presence of CO molecules. Whereas CO induces mobility of Pd adatoms, surface OH has the opposite effect, pinning the Pd adatom on the surface and blocking any further mobility, even in the presence of CO. In the light of these findings, two further experiments should be conducted in the future.

First, higher coverages of Pd deposited on the surface should, in principle, yield a high coverage of Pd adatoms, if the presence of CO molecules in the backpressure will be minimized (in case of our RT STM vacuum system, this can be accomplished by cooling down the cryostat in the analysis chamber and switching off all the filaments including pressure gauges, and properly outgassing the e-beam evaporator). Second, Pd should be deposited on a surface with a high density of surface OH. Surface OH prevents the mobility of Pd adatoms. Potentially, a chemically stable model catalyst system could be created in this way. Additionally, it will be interesting if the mobility of small Pd clusters can be also induced by CO, in accordance with a recently-reported study demonstrating that of CO molecules induce Smoluchowski ripening of Pt cluster arrays on the Graphene/Ir(111) moiré pattern [16].

8.3 Monte Carlo simulation of metal adsorption at RT

We found experimentally that metals (Au, Pd and Fe) adsorb on the reconstructed $\text{Fe}_3\text{O}_4(001)$ surface as adatoms. In case of Au and Fe, this statement is valid for sub-monolayer coverage; at higher coverage, clusters are formed. For Au, we proposed a "rolling snowball" model (see section 8.1.6), based on a formation of a Au dimer, which is created when a Au atom lands on the surface with high local coverage of Au adatoms. According to the proposed "rolling snowball" model, the Au dimer does not decay into two Au adatoms on a clean surface. In case of Pd, we identified cluster formation as a consequence of CO-induced mobility. Contrary to Au, a Pd dimer is unstable and readily decays into a Pd adatom and a Pd-carbonyl. Unpublished results done by R. Bliem suggest that, in case of Pd/ Fe_3O , a near-full monolayer of adatoms can be created at RT.

The adatoms are often found in ordered arrays for sub-monolayer coverage. Using a Monte Carlo simulation, we will show that in case of Au adatoms, there is no strong interaction between a Au atom landing from the gas phase and the adatoms. From the knowledge that Au clusters starts to form at a coverage of ~ 0.12 ML (see section 8.1.4), we can estimate a distance the Au atom can travel from its landing position.

Monte Carlo simulations were performed with the numerical software package MATLAB R2010b, using its dedicated random number generator. Several assumptions were made in these calculations. These include:

- atoms land on the surface at a random position,
- atoms adsorb only in the narrow site,
- a narrow site can be occupied only by a maximum of 1 atom,
- no interaction exists between adsorbed atom and adatoms.

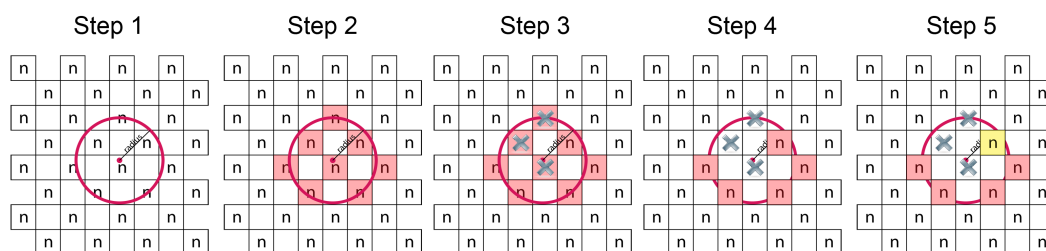


Figure 8.21: Schematic model of each iteration of a Monte Carlo simulation. In step 1, an atom is randomly placed on the surface (uniform distribution). The atom probes the narrow sites within the radial travel distance (step 2). In step 3, an analysis of already occupied narrow sites is performed and, the occupied narrow sites are excluded (step 4). Finally, the atom is placed into the closes available narrow site to the landing position. Then, a next iteration is started. When is no available narrow site present, a cluster is created and the simulation is interrupted.

To model where an atom lands on the surface, a uniform distribution was used. One iteration of the simulation cycle is shown in figure 8.21. The surface potential energy landscape is approximated by squares, representing the narrow sites; the wide sites are shown as empty

Chapter 8. Template-induced adsorption

squares. In step 1, an atom is placed into a random position on the simulation area. The radial travel distance (r) determines the radial distance the atom can travel from the landing position. In step 2, the adsorption sites within, or intersecting, the circle defined by r are found. Step 3 analyzes the already filled narrow sites and these are excluded from the available ones, as is shown in step 4. Finally, the adatom is placed into the nearest available narrow site, marked by yellow color in step 5 in figure 8.22. In case there is no available narrow site (step 4), a cluster is formed according to the "rolling snowball" model (see section 8.1.6). Since these simulations were done in order to reproduce the Au/Fe₃O₄(001) STM images, we allowed the simulation to create one cluster per 30 × 30 nm². A typical simulation area was 120 × 120 nm², corresponding to 16 clusters created in the image. When a cluster formation event occurred, the atom was deleted from the simulation. The simulation was finished when a pre-set number of clusters is formed.

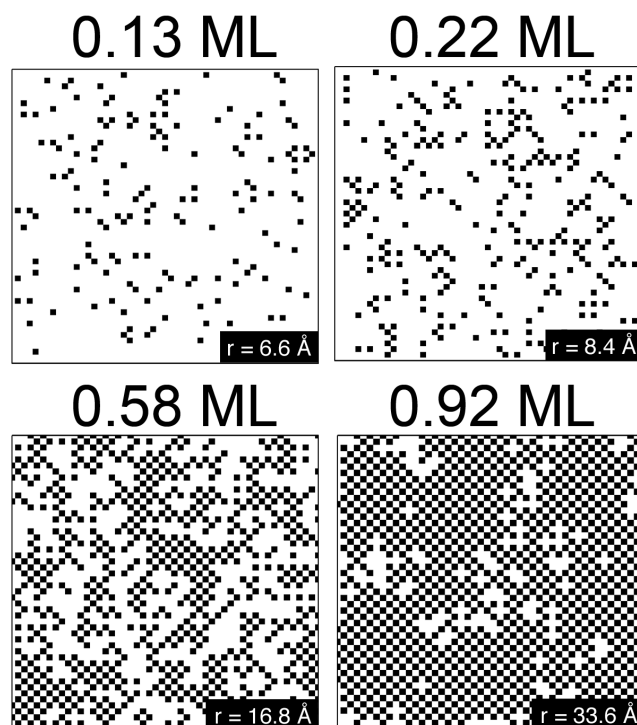


Figure 8.22: Monte Carlo simulations of STM images with adatoms. The adatom coverage is indicated above the image, the used radial travel distance is shown in right bottom corner of the image.

Figure 8.22 shows simulated STM images with a different density of adatoms; a consequence of an increased radial travel distance. Interestingly, the adatoms form ordered arrays with a large number of pairs. To simulate a coverage obtained for 0.12 ML Au (see figure 8.1), the radial travel distance has to be set to $\sim 6.6 \text{ \AA}$ (radial distance shown in the right bottom corner of each simulated STM image). Such a small value means that the adsorbed Au atom could probe only the nearest neighbor narrow sites and, in most cases, not even all four nearest narrow sites could be reached by the atom: typically only 2–3 are available at this radial travel

8.3. Monte Carlo simulation of metal adsorption at RT

distance. If the radial travel distance is set equal to the size of an unit cell, an adatom coverage of ~ 0.22 ML is formed. If r is twice of the value of unit cell, ~ 0.58 ML is formed and four times the value of unit cell leads to a near full coverage of adatoms (~ 0.92 ML).

The presented Monte Carlo simulation does not assume any interaction between the adsorbed atoms and adatoms; the only constraint is a given by the reconstruction-induced adsorption template. In figure 8.22 (0.13 ML), we obtained a large number of adatoms sitting next to each other, forming pairs and ordered patches. Comparing this simulated image with experimentally acquired image of Au/Fe₃O₄(001) (0.12 ML Au adatoms, previously shown in figure 8.1), we get a similar number of pairs of atoms in close vicinity. However, the position of adatoms is still random. This is demonstrated by a radial distribution function (RDF) of adatoms for a simulated (0.13 ML) and experimental image (0.12 ML Au adatoms, previously shown in figure 8.1). In both cases, the distribution was acquired by integrating the power spectrum. The RDF is shown in figure 8.23. The simulated spectrum shows a completely random distribution of adatoms (i.e., RDF $\equiv 1$). This result is expected, because no constraint causing a non-random adsorption of atoms is present in the simulation code. For the experimental data (0.12 ML Au), we do observe a slightly higher occurrence of the second nearest neighbor distance ($r = 11.8$ Å, an analysis of a $\sqrt{2}$ spot), but due to the high error value, there is no indication that the position of adatoms is non-random.

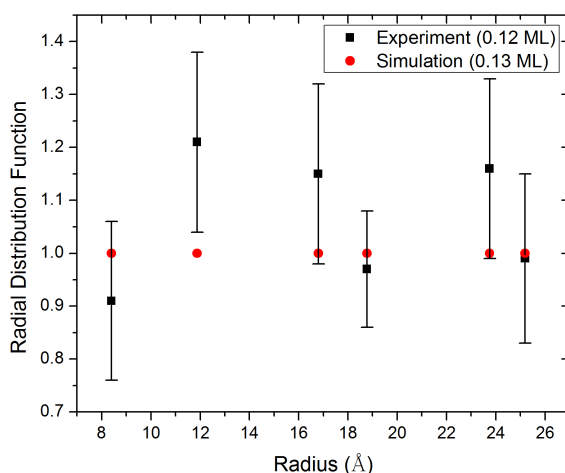


Figure 8.23: Radial distribution function (RDF) for a Fe₃O₄(001) surface with adatoms. The red dots show the RDF for an experiment with 0.12 ML Au adatoms (previously shown in figure 8.1). The black dots show an RDF for a simulated image with 0.13 ML of adatoms. A RDF value of one corresponds to a random distribution.

Figure 8.24 plots the density of adatoms as a function of a radial travel distance. The results are shown for two different sizes of a simulation area: 60×60 nm² and 120×120 nm². The error bar was calculated from 20 independent runs. A simulation of a smaller area was also performed and yields the same results, but the error is bigger. The density of adatoms as a function of radial travel distance shows a logarithmic behavior.

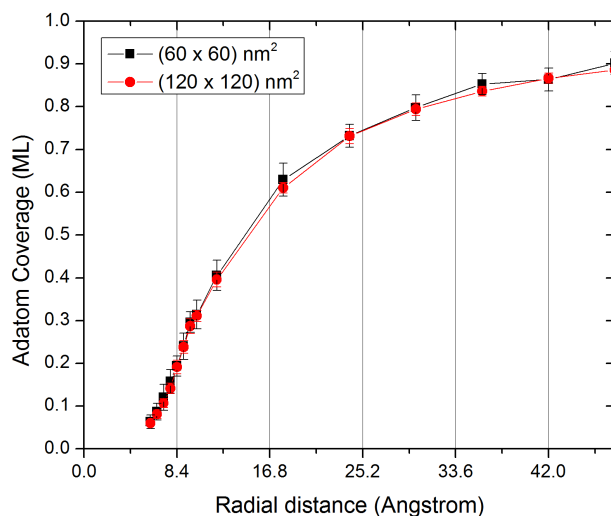


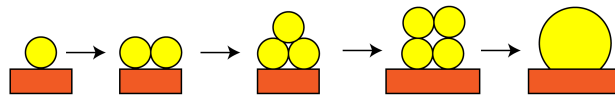
Figure 8.24: Coverage of adatoms as a function of radial travel distance in Monte Carlo simulations. Curves for two sizes of simulation area are shown.

8.3.1 Discussion

The presented Monte Carlo simulations were performed in order to obtain insights into the behavior of atoms after landing from the gas phase. In case of Au/Fe₃O₄(001), simulations can reproduce the experiment. Unpublished results done by R. Bliem suggest that in case of Pd/Fe₃O₄(001), a near-full monolayer of adatoms can be created at RT. According to the results shown in figure 8.24, this will correspond to an atom moving over the distance of several unit cells. It seems not probable that the atom will be able to do so without interaction with other adatoms.

We propose that the maximum achievable coverage of adatoms is linked to the stability of a dimer. As we proposed in the “rolling snowball” model (see section 8.1.6), the Au dimer is stable against decaying into two monomers. Since the Au dimer was not a stable feature at RT, it grew until a critical size of the smallest stable cluster was reached. This is illustrated in figure 8.25a. In case of Pd, we showed that the Pd dimer (more exactly Pd–Pd–CO) is not stable, and can decay back into two monomers at RT. This is illustrated in figure 8.25b. If such a dimer will form, move to another area of a clean B layer surface, and decay into two monomers, a near full coverage of adatoms will be achievable.

(a) Stable dimer



(b) Unstable dimer

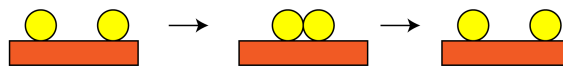


Figure 8.25: Schematic diagram showing stability of a dimer. (a) Dimer is stable against decaying into two monomers. Since this dimer is not a stable feature, it grows until a critical size for a stable cluster is reached. (b) Dimer is formed from two monomers. Later, the dimer can decay back into two monomers.

9 Conclusion

In this thesis, we investigated the defects and adsorption properties of the $\text{Fe}_3\text{O}_4(001)$ surface. The majority of the work was done on the reconstructed B layer surface. This surface forms a $(\sqrt{2} \times \sqrt{2}) R45^\circ$ reconstruction, caused by pairs of FeB and neighboring O ions slightly displaced laterally, forming undulating rows of atoms with two inequivalent FeA bulk continuation sites. We termed these sites narrow and wide, respectively.

We identified the common defects at the reconstructed B layer surface. The most common defect is V_O . V_O is very reactive with water. Therefore, we do not observe the V_O 's directly. Instead, we regularly observe pairs of surface OH groups, originating from a water molecule dissociated on an V_O . Another typical defect is FeA adatom, as observed previously [32]. We identified another commonly observed surface defect: APDBs. These are formed on the surface because the $(\sqrt{2} \times \sqrt{2}) R45^\circ$ reconstruction has two equivalent domains with respect to the bulk structure. These two domains have a phase shift in the undulation of the FeB rows, which results in a narrow site being transformed into a wide one, and vice versa. Where these two inequivalent domains meet, an APDB is formed. APDBs are often decorated with adsorbed molecules. Simulated STM images reproduce the appearance of the APDBs in the experimental data and reveal that they are preferential adsorption sites for hydroxyl groups.

We found that the reconstructed B layer surface is inert against adsorption of H_2 , CO and CO_2 for pressure up to 10^{-5} mbar at RT. As mentioned above, on a B layer, water readily dissociates in the presence of V_O 's. At RT, water can be dissociated also on the same surface in the absence of V_O 's, up to a saturation coverage of 0.0825 ML with respect to the surface O atoms. However, high-resolution STM images of the water-exposed $\text{Fe}_3\text{O}_4(001)$ surface appear identical to those obtained following deposition of atomic H [34]. There is no evidence for the presence of the water hydroxyl (OH) species on the surface. The absence of the OH is confirmed by low energy He^+ ion scattering utilizing isotopically-labeled H_2^{18}O . Annealing of the hydrogenated surface leads to the abstraction of lattice O atoms and desorption of water. Consequently, water can reduce the $\text{Fe}_3\text{O}_4(001)$ B layer surface under UHV conditions.

We successfully created a variety of Fe-rich surface terminations, which were predicted by DFT+U calculations [39]. At RT, Fe adsorbs as single adatoms for a low Fe coverage, and as adatoms and clusters for a higher Fe coverage. Mild annealing of the sample leads to a surface containing Fe monomers and Fe octahedral pairs (Fe-OP's). Two-fold coordinated FeA and five-fold coordinated Fe-OP's form at 423 K, while only Fe-OP's are observed at 573 K. For higher Fe coverage the surface exhibits an FeO-like structure with all surface octahedral sites

filled with Fe cations. We found an alternative route to create Fe-rich terminated surfaces (0.5 ML FeA and Fe-OP termination). This is based on a reduction of the B layer surface via Ar⁺ sputtering, and a controlled anneal temperature at low oxygen chemical potential. Moreover, we have found that the Fe-rich terminations can be formed as a consequence of a non-stoichiometry of the used single crystal. Angle-resolved X-ray photoelectron spectroscopy indicates that all Fe-rich surfaces contain mainly Fe²⁺. All these Fe-rich terminations are metastable; at high oxygen chemical potential, they are transformed into the reconstructed B layer surface.

We later focused on the ($\sqrt{2} \times \sqrt{2}$) R45° reconstructed B layer surface. At fractional monolayer coverages, and at RT, H, H₂O, Fe, Au, and Pd adsorb as single adatoms in the narrow site of the surface unit cell, forming ordered structures on the surface. This revealed an unique property of the reconstructed B layer surface; this surface acts as a rather robust adsorption-temple. The same behavior was later observed for Sr, Ni and Ag (unpublished data acquired by R. Bliem, O. Gamba, and G. S. Parkinson).

We discovered a remarkable stability of Au adatoms, both chemically in up to 10⁻⁴ mbar of CO, and thermally up to 673 K. At higher annealing temperatures, different sizes of three-dimensional Au clusters were observed. For coverage below 0.12 ML, we observed only Au adatoms on the surface. For higher Au coverages, we observed Au adatoms and 3D clusters. We proposed a model of cluster nucleation, which is based on a stable Au dimer that does not decay into two adatoms. We also found that Au adatoms sinter if adatoms and clusters are present at the same time, even for temperatures below 673 K. This suggests that sintering of adatoms is caused by the cluster mobility. XPS measurements are consistent with a positive charge state of the single adatoms.

Finally, we identified the mechanism of sintering of Pd/Fe₃O₄(001). For Pd adatoms, CO induces mobility via formation of a Pd-CO complex. When at least three Pd-CO meet on the surface, homogeneous nucleation of a cluster takes place. Clusters grow through cluster migration and coalescence. Surface OH groups have the opposite effect to CO, immobilizing the Pd-CO group and stabilizing the Pd adatom on the surface.

The present thesis suggest that the reconstruction-induced adsorption templating property of the (001) B layer surface is rather universal. Single atoms anchored to metal oxide surfaces offer a great potential for achieving a high activity and selectivity in heterogeneous catalysis. Fe₃O₄(001) is, therefore, a promising candidate for a substrate in single atom catalysts systems.

A List of known features on the $\text{Fe}_3\text{O}_4(001)$ surface

The aim of this appendix is to summarize the known features on the $\text{Fe}_3\text{O}_4(001)$ surface.

Feature	Apparent height in STM (pm)	Described in:
OH	70	Section 5.1
FeA	80	Section 7.1.1
Au adatom	100	Section 8.1.1
Pd adatom	120	Section 8.2.1
Pd-CO	230	Section 8.2.1
Pd-OH	270	Section 8.2.1

Table A.1: Apparent height of known features on the $\text{Fe}_3\text{O}_4(001)$ surface. The value is always measured with respect to the average height of the neighboring FeB atoms, at a bias voltage of +1 V and tunneling current 0.3 nA.

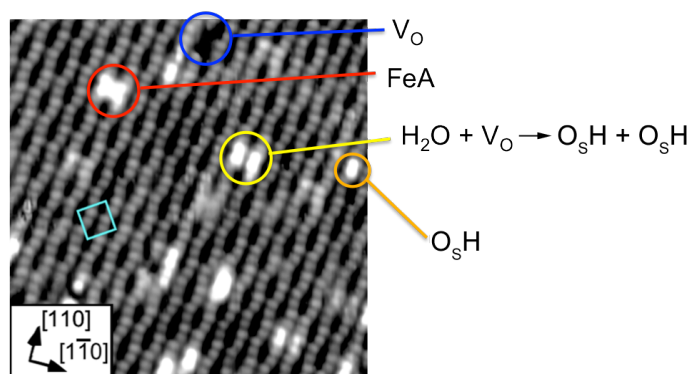


Figure A.1: STM image of a clean B layer surface with typical defects highlighted in the image. These include an FeA adatom, a surface OH, an oxygen vacancy (V_O) and a H_2O molecule dissociated in V_O . Same image as shown in figure 6.3. Scanning details: $(20 \times 20) \text{ nm}^2$, $V_s = +1 \text{ V}$, $I_t = 0.3 \text{ nA}$.

Appendix A. List of known features on the $\text{Fe}_3\text{O}_4(001)$ surface

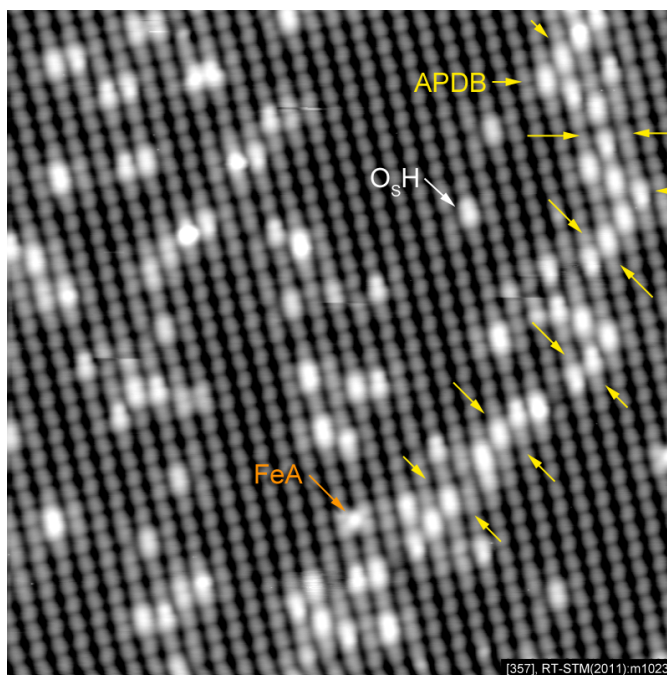


Figure A.2: STM image of a flat terrace, containing an APDB (highlighted by yellow arrows). The image also contains one FeA adatom and several surface O_sH groups. Scanning details: $(20 \times 20) \text{ nm}^2$, $V_s = +1.2 \text{ V}$, $I_t = 0.23 \text{ nA}$.

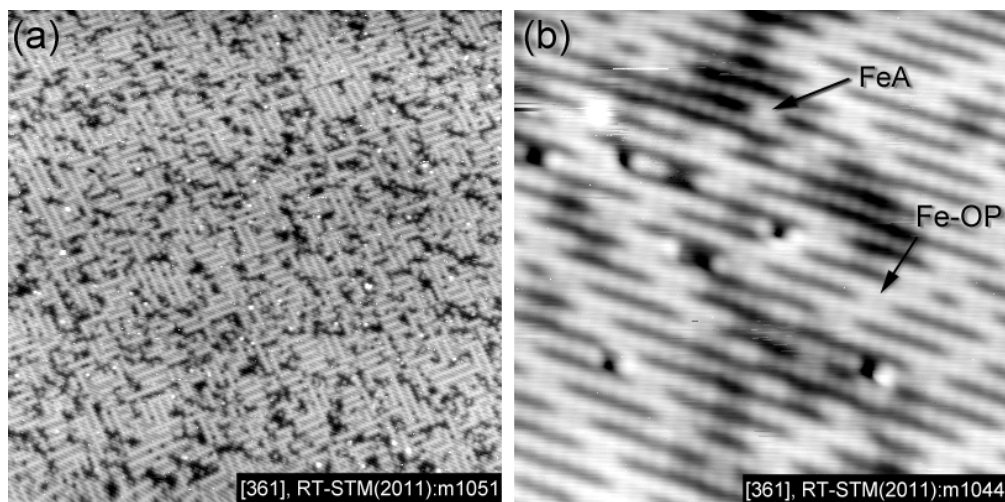


Figure A.3: STM image of an Fe-OP tetraminated surface. Dark areas indicate the underlying B layer surface. The presence of Fe-OP brightens the surrounding FeB atoms. This is caused by the transformation of these atoms to Fe^{2+} . Scanning details: (a) $(100 \times 100) \text{ nm}^2$, $V_s = +1.1 \text{ V}$, $I_t = 0.32 \text{ nA}$, (b) $(10 \times 10) \text{ nm}^2$, $V_s = +1.4 \text{ V}$, $I_t = 0.44 \text{ nA}$.

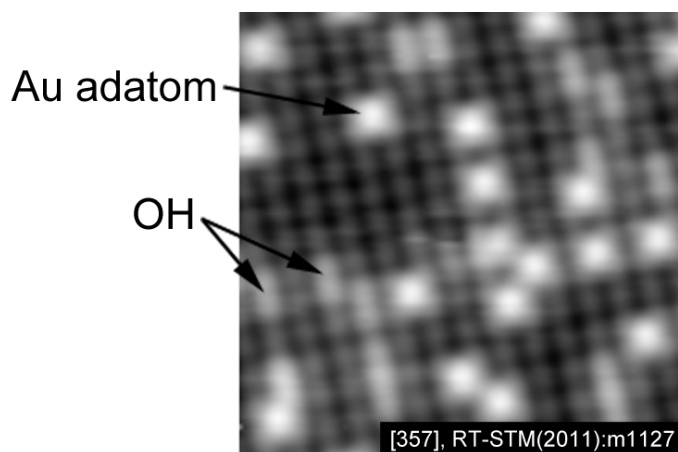


Figure A.4: STM image of a single Au adatoms. Scanning details: $(9 \times 9) \text{ nm}^2$, $V_s = +1 \text{ V}$, $I_t = 0.38 \text{ nA}$

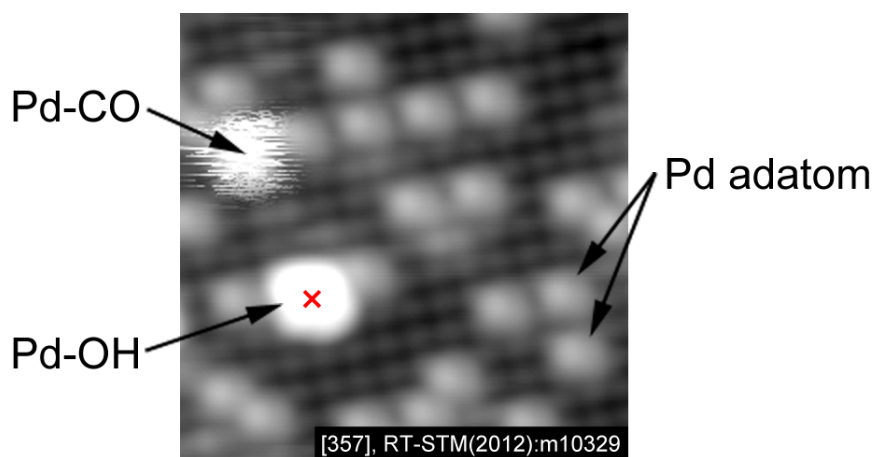


Figure A.5: STM image containing single Pd adatoms, one Pd-CO group and one Pd-OH group. Scanning details: $(9 \times 9) \text{ nm}^2$, $V_s = +1.2 \text{ V}$, $I_t = 0.3 \text{ nA}$

B List of samples

Table B.1 and B.2 lists all the magnetite (001) samples acquired between 2010 and 2012. The table contains information about the experimental work done on each given crystal, its dimensions, impurities, stoichiometry, and a few other general remarks.

Appendix B. List of samples

Crystal No.	Experiments done	Source, dimensions	Impurities	Comments
349	Atomic H[34]	Commercial Crystal labs 5 × 5 mm ² (originally 10 × 10 mm ² , sample cut into 4 pieces).	Natural crystal, Na, K, Mg as inclusions, and Si distributed across the surface (EDAX).	No clear Verwey transition was visible (using PPMS, Solid State Physics group TU Wien).
356	ISS (H ₂ O, H ₂ ¹⁸ O) [51], SMOKE (unpublished)	Synthetic single crystal rod (Lot.No. 10050613) grown by Prof. Mao and co-workers (Tulane University), cut and polished by Mateck GmbH, irregular shape ~ (10 × 6) mm ² .	Stoichiometric (based on the sharpness of the Verwey transition).	Sharp Verwey transition (observed by Mao, see fig. 4.1b). Crystal became defective and finally was broken when mounting for TPD.
357	H ₂ O and D ₂ O adsorption [51], Sample preparation study [53], APDB [52], Fe deposition [39], Self-assembly of rubrene (unpublished), Surface Verwey transition (submitted 2013), Au deposition [54], Pd deposition [55], Ni deposition (unpublished), SIMS (unpublished), All synchrotron experiments.	Synthetic single crystal rod (Lot.No. 10050613) grown by Prof. Mao and co-workers (Tulane University), cut and polished by Mateck GmbH, ~5 mm diameter, 1 mm thick.	Stoichiometric (based on the sharpness of the Verwey transition, and SIMS).	Sharp Verwey transition (observed by Mao, see fig. 4.1b). Surface became rough and was re-polished in 2012 (SP-PES and Ni deposition done after re-polishing).

Table B.1: List of (001) oriented Fe₃O₄ samples used during the PhD work (1 of 2).

Crystal No.	Experiments done	Source, dimensions	Impurities	Comments
361	STM of clean surface, Surface Verwey transition	Synthetic single crystal rod (Lot.No. 11072701) grown by Prof. Mao and co-workers (Tulane University), cut and polished by MaTeck GmbH, oval shape $\sim(8.5 \times 4.5) \text{ mm}^2$.	Stoichiometric (central area), FeO-like grains on the edge of the crystal (SIMS).	Sample is Fe-OP terminated after UHV annealing at 893 K Ordered surface couldn't be obtained in PINUP (May 2013).
365	STM of clean surface.	SurfaceNet GmbH, $(10 \times 10 \times 1) \text{ mm}^3$.	Unknown	UHV anneal not tested.
366	STM of clean surface.	SurfaceNet GmbH, $(10 \times 10 \times 1.5) \text{ mm}^3$.	Unknown	UHV anneal not tested.
370	STM of clean surface, Ni deposition (unpublished).	SurfaceNet GmbH, $(10 \times 10 \times 1.5) \text{ mm}^3$.	Unknown	Fe-OP terminated when not annealed in O_2 .

Table B.2: List of (001) oriented Fe_3O_4 samples used during the PhD work (2 of 2).

B.1 Sample-dependent surface terminations

The scientific community has investigated the properties of magnetite using various types of samples: natural single crystals (NSC), synthetic single crystals (SSC), and thin films grown on suitable substrates. In the past, there was a belief that the ideal material to investigate the properties of magnetite are natural single crystals. This popularly held belief was proven to be wrong during the studies of Verwey transition [27, 28]. Natural single crystals cannot be representative of magnetite properties because of the variations in structure, stoichiometry, impurity content and stored stress, which is often dependent on the origin of the natural single crystal. The same general problem holds also for magnetite thin films. Nowadays, there is general agreement that only stoichiometric Fe_3O_4 samples show a sharp Verwey transition at Verwey temperature of about 125 K (during warming). A deviation of the Verwey temperature, or missing Verwey transition, points to the fact that the probed sample is non-stoichiometric. Nevertheless, SSC are not commercially available. Therefore natural single crystals or magnetite thin films are often used. In this section we will demonstrate the role surface stoichiometry on the appearance of the (001) surface termination. Using the SSC No. 357 as a reference, we will compare this crystal with another SSC, two NSC and a thin film grown on $\text{MgO}(001)$. From our experience, sample preparation finished with annealing in O_2 produces reproducibly a reconstructed B layer surface, irrespective of the single crystal used (both NSC and SSC). In contrast, when the sample preparation is finished by annealing in UHV, either a B layer, or various types of Fe-rich terminations are possible. This will be demonstrated on several selected cases.

B.1.1 $\text{Fe}_3\text{O}_4(001)361$ SSC

Following the sample preparation procedure mentioned in section 4.3, this $\text{Fe}_3\text{O}_4(001)361$ SSC produced the same surface termination as SSC No. 357, if the crystal was annealed in O_2 in the final step. SSC No. 357 is B layer terminated also when annealed in UHV. However, sample No. 361 shows a different behavior. This is demonstrated in figure B.1, where in part (a) a surface is terminated with a reconstructed B layer after annealing in oxygen (5×10^7 mbar for 45 minutes), while in part (b) the surface is terminated with Fe-OP after annealing in UHV at 893 K for 45 minutes. Moreover, the Fe-OP termination can be switched back to a reconstructed B layer by annealing in oxygen, or in the opposite direction by annealing in UHV. From the resistivity measurement, we know that the crystal No. 361 is stoichiometric with a sharp Verwey transition.

To understand this behavior, Secondary Ion Mass Spectroscopy (SIMS) measurements were performed, in order to find where the extra Fe comes from during UHV annealing. The SIMS measurements were also performed on crystal No. 357, which was taken as a reference. The ratio between the intensity of the ^{56}Fe peak and the intensity of the ^{16}O peak was recorded.

On crystal No. 357, the Fe/O ratio is 0.00315 ± 0.00038 and this value is uniform across the entire crystal area (value acquired over area of (0.5×0.5) mm^2 , where no crystallographic defects were present). On the other hand, crystal No. 361 appears visually defective. It is clearly not one single crystal, but composed of several grains. The picture of sample No. 361, taken with an optical microscope Olympus SZX12, is shown in figure B.2a. The central part, which visually looks like one single crystal grain (shown in red color in the scheme in part b) is surrounded

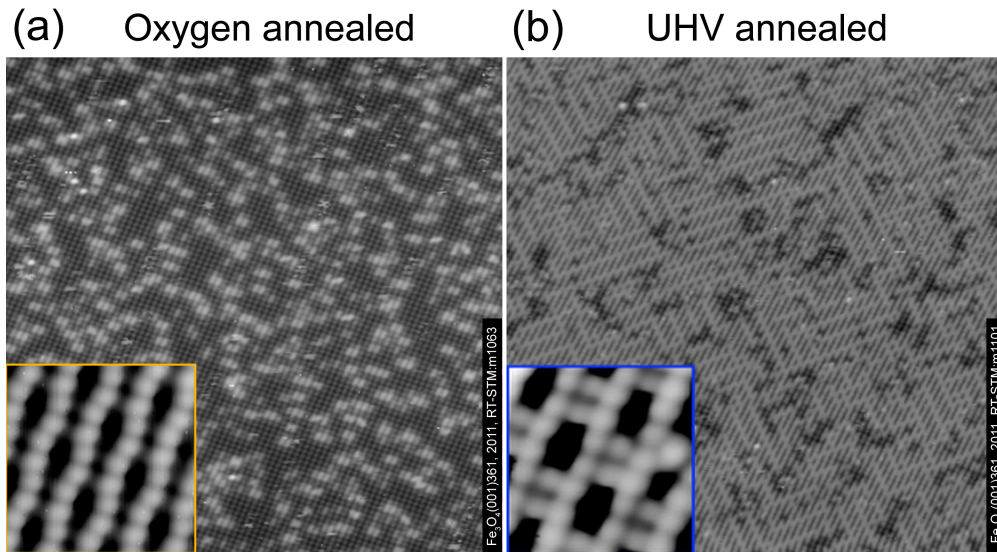


Figure B.1: Part (a) shows a reconstructed B layer, resulting from annealing on oxygen. Scanning details: $(50 \times 50) \text{ nm}^2$, $V_s = 1.16 \text{ V}$, $I_t = 0.29 \text{ nA}$. Part (b) shows the surface of the same sample, but after annealing in UHV. The surface is terminated with Fe OP. Scanning details: $(50 \times 50) \text{ nm}^2$, $V_s = 0.87 \text{ V}$, $I_t = 0.31 \text{ nA}$.

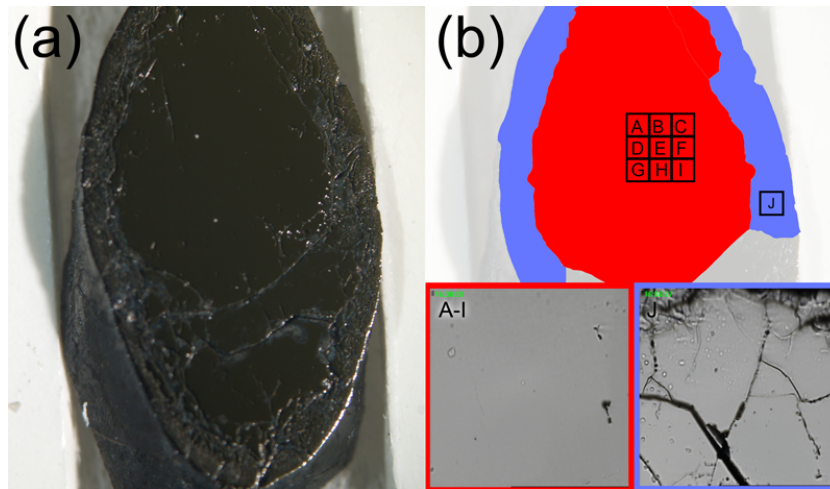


Figure B.2: (a) Image of the $\text{Fe}_3\text{O}_4(001)361$ synthetic single crystal taken with an optical microscope (Olympus SZX12). Part (b) shows a color coded scheme of the optical image, distinguishing two different areas on the polished surface. Red color maps the single crystalline area, blue represents a polycrystalline area. The rectangular overlay shows areas where SIMS measurements were performed (dimensions of the overlay are exaggerated). The left inset with the red frame in part (b) shows real space images from area A-I $(1.2 \times 1.2) \text{ mm}^2$, the right inset with the blue frame shows area J $(0.25 \times 0.25) \text{ mm}^2$.

by disordered areas (blue in color scheme in part b). The obvious questions is: does the central part of the crystal have the same stoichiometry as crystal No. 357, and, is there any

Appendix B. List of samples

difference in the stoichiometry between the parts of the crystal highlighted with red color and with blue color? To address these questions, SIMS measurements were performed on this crystal. The location of measured areas is shown in the overlay in figure B.2b. Nine areas, denoted as A-I, were measured in the red highlighted part of the crystal probing the total area of $(1.2 \times 1.2)\text{mm}^2$. Additionally, the stoichiometry of the defective, blue labeled area, denoted as J ($0.25 \times 0.25\text{mm}^2$), was measured.

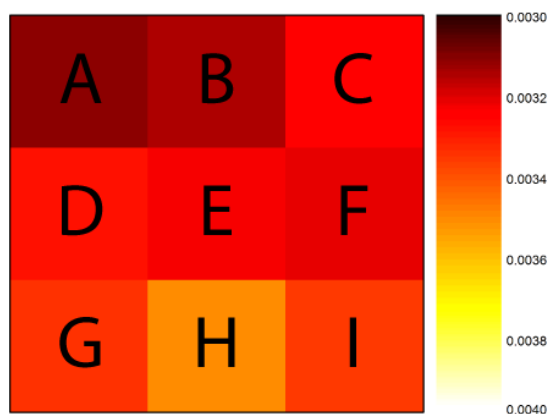


Figure B.3: 2D color coded map shows Fe/O ratio on areas A to I (see overlay in figure B.2b) measured with SIMS on the $\text{Fe}_3\text{O}_4(001)361$ synthetic single crystal.

The results from measurements in area A-I are shown in figure B.3. The Fe/O ratio within the area A to I is relatively uniform, with the mean value of 0.00327 ± 0.00012 , showing the same value as crystal No. 357 within the statistical error. In the disordered area, labeled J in figure B.2b, the Fe/O ratio is 0.0043 ± 0.0009 . This area is clearly Fe rich, compared to areas A-I. Moreover, then taking the Fe/O value from the areas A-I as a reference and assuming that this area is composed of stoichiometric Fe_3O_4 (i.e. Fe/O ratio is 0.75), then the Fe/O ratio in area J will be 0.991. The defective parts of the crystal in area J have an FeO-like stoichiometry. Interestingly, we were unable to transform B layer to Fe-OP on No. 361 sample if we annealed below 873 K. On the other hand we were able to transform B layer to Fe-OP termination by UHV annealing at 893 K. Therefore there exist a thermal barrier for Fe diffusion from Fe-rich areas to the stoichiometric areas of the crystal.

B.1.2 $\text{Fe}_3\text{O}_4(001)349$ NSC

The natural single crystal (NSC) $\text{Fe}_3\text{O}_4(001)349$ had no measurable Verwey transition. This was caused by the impurities (see table B.1). The crystal was always B layer terminated after annealing to temperatures above 873 K, irrespective whether O_2 was present in the chamber, or not. In figure B.4, we show the surface after two cycles of sputtering with Ar^+ ions (1 keV, $1.5 \mu\text{A}$, 20 minutes) and UHV annealing (~ 879 K, 30 minutes). The surface is B layer terminated. Even after annealing at ~ 879 K for extended period of time (16 hours) the surface does not change the termination. This crystal showed exactly the same response to the same sample preparation conditions as SSC No. 357. From our point of view, this NSC represents an ideal sample for experiments performed above the Verwey transition temperature.

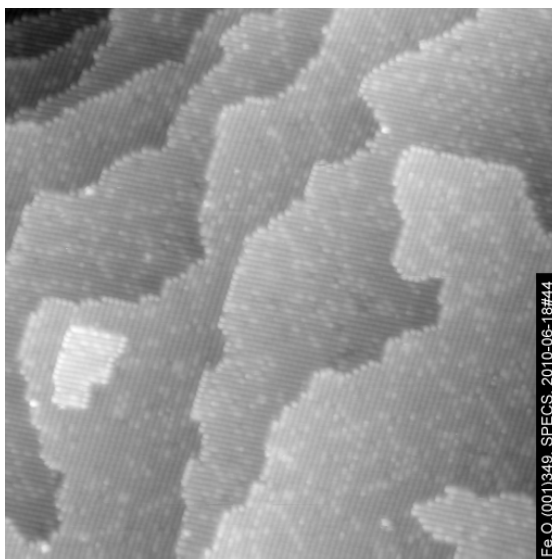


Figure B.4: NSC No. 349: STM image of the B layer terminated surface prepared by two cycles of sputtering, followed by annealing in UHV at ~ 879 K. Scanning details: $(50 \times 50) \text{ nm}^2$, $V_s = +1.16\text{V}$, $I_t = 0.29\text{nA}$.

B.1.3 $\text{Fe}_3\text{O}_4(001)370$ NSC

Another NSC was obtained from the company SurfaceNet. In this case, the sample was prepared in a similar way as NSC No. 349 described above: two cycles of sputtering with Ar^+ ions (1 keV, $1 \mu\text{A}$, 20 minutes), followed by annealing in UHV (~ 879 K, 30 minutes). This sample preparation procedure leads to Fe-OP terminated surface, as shown in figure B.5.

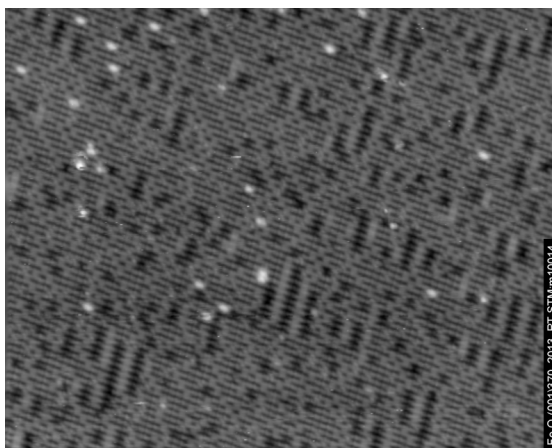


Figure B.5: STM image of the Fe-OP terminated surface prepared by two cycles of sputtering, followed by annealing in UHV at ~ 879 K. Scanning details: $(50 \times 40) \text{ nm}^2$, $V_s = +1\text{V}$, $I_t = 0.3\text{nA}$.

The surface is Fe-OP terminated after this sample preparation procedure. Although in this case, the sputter dose was higher, the surface termination is unexpected. To our knowledge, the same sample preparation with the SSC No. 357 and NSC No. 349 will produce a B layer

Appendix B. List of samples

terminated surface. However, we could not identify the source of extra Fe: it could be due to bulk non-stoichiometry, or Fe-rich areas on the surface, as observed in case of SSC No. 361. For a further understanding of the origin of the non-stoichiometry, SIMS measurements will be needed.

B.1.4 $\text{Fe}_3\text{O}_4(001)/\text{MgO}(001)$ thin film

A thin film of $\text{Fe}_3\text{O}_4(001)$ was grown on a $\text{MgO}(001)$ substrate by S. A. Chambers and co-workers at PNNL¹. The sample was then transferred to Vienna in a UHV vacuum container and subsequently inserted into the SPECS system. The total exposure of the thin film to ambient conditions was less than ten minutes.

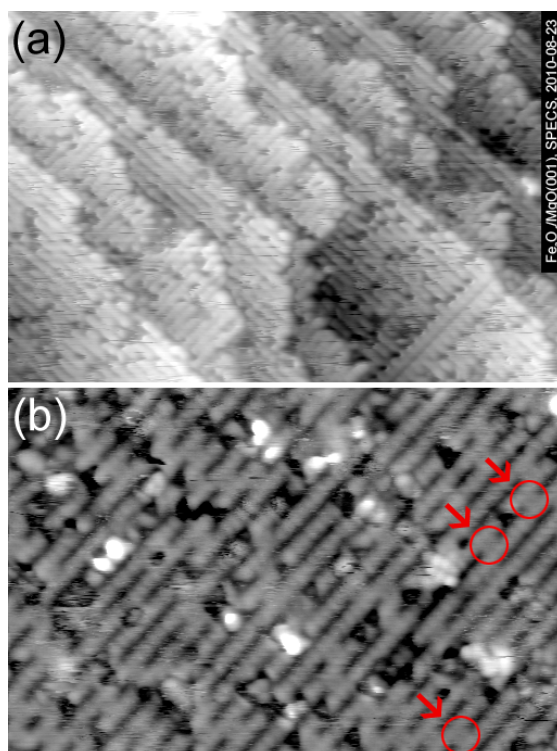


Figure B.6: STM image of a $\text{Fe}_3\text{O}_4/\text{MgO}(001)$ thin film after light sputtering and annealing in UHV at 773 K for 15 minutes. (a) A large scale image showed a relatively small terraces. (b) Atomically resolved image shows a large number of Fe-OP's (three of them highlighted with red arrows).

The sample was initially prepared by growth of Fe in the presence of oxygen plasma [84]. The Fe deposition rate was $0.5 \pm 0.1 \text{ \AA s}^{-1}$. The thin film consist of a 1000 \AA thick Fe buffer layer grown at 723 K, followed by 1000 \AA thick Fe layer grown at 523 K. The buffer layer growth temperature is in the temperature range where Mg out-diffusion takes place [85]. The higher growth temperature was used in order to relieve interfacial strain and to remove defects. The buffer layer was atomically flat, as was monitored by reflection high energy electron

¹Pacific Northwest National Laboratory, Richland, WA 99354, USA.

B.1. Sample-dependent surface terminations

diffraction (RHEED). In-situ analysis after the thin film growth showed a single phase Fe_3O_4 (XPS) with $(\sqrt{2} \times \sqrt{2}) R45^\circ$ symmetry (LEED).

After the film exposure ambient conditions, the surface became dirty (we measured a significant C 1s core-level peak in XPS). We found that these carbon-containing compounds can be removed only by sputtering. We cleaned the thin film by a several cycles of sputtering and annealing in UHV. During sample cleaning, we monitored the composition with XPS, and paid special attention to the concentration of C and Mg. In figure B.6a, we show an STM image of the thin film after light sputtering (1 keV, $I_S = 1 \mu\text{A}$, 10 minutes) and anneal to 773 K for 15 minutes. The XPS spectrum (data not shown) showed an onset of the Mg 2s core level peak, while the intensity of a C 1s peak was minimized. A small area STM image on a flat terrace (see figure B.6b) shows that the surface is terminated with Fe-OP's. We note that the surface was not annealed in oxygen during the cleaning procedure².

²The STM experiments on the $\text{Fe}_3\text{O}_4/\text{MgO}(001)$ thin film were done prior to the work summarized in chapter 7. We never imaged the thin film after annealing in oxygen, however, the surface shown in figure B.6 should transform to B layer after annealing in oxygen (623 K, $p_{\text{O}_2} = 2 \times 10^{-6}$ mbar). This claim is based on the STM surface phase diagram, shown in figure 7.9.

List of Figures

1.1	TOF for CO oxidation at 273K as a function of mean Au particle diameter	2
1.2	TOF for CO oxidation at 300K as a function of mean Au particle diameter on TiO ₂	3
1.3	Two main mechanisms of cluster sintering.	3
2.1	Structural models of different forms of iron oxides	5
2.2	Inverse spinel bulk unit cell of Fe ₃ O ₄	7
2.3	A model of the reconstructed B layer surface	8
3.1	Schematics of electron tunneling in STM	10
3.2	Schematic view of an scanning tunneling microscope	10
3.3	LEIS: schematic model of interaction of an ion with the surface	11
4.1	Temperature-dependent resistance measured on the as grown single crystalline bar	15
4.2	Degradation of the Fe ₃ O ₄ (001)357 crystal after 2 year's use	17
5.1	STM images of a clean reconstructed B layer following the dose of atomic H	22
5.2	TPD spectrum of water desorption from Fe ₃ O ₄ /MgO(001)	23
5.3	Different coverages of water adsorbed onto a clean B layer surface at RT	24
5.4	Density of the surface OH groups observed in STM images versus the nominal water coverage	24
5.5	LEIS spectra on a clean and a water-dosed surface	25
5.6	STM image of an OH saturated surface, annealed to 520 K	26

List of Figures

6.1	STM images of surface with anti-phase domain boundaries	30
6.2	Formation of APDB during terrace growth	31
6.3	STM image of a clean B layer surface with typical defects highlighted in the image	32
7.1	DFT+U derived surface phase diagram of the Fe ₃ O ₄ (001) surface	33
7.2	Fe deposition onto the B layer at RT: FeA and clusters	35
7.3	Formation of Fe octahedral pairs (Fe-OP)	36
7.4	Proof that Fe-OP adsorb in the narrow site	37
7.5	STM image of an FeO-like termination	38
7.6	STM image of a high Fe coverage	39
7.7	Density of states (DOS) and spin density for the Fe-rich terminations	41
7.8	XPS spectra for a reconstructed B layer and an Fe-rich surface terminated with Fe-OP's	42
7.9	Surface phase diagram for a SSC No. 357	44
7.10	STM image of 1.2 ML* Fe deposited at ~373 K and, imaged at RT	45
8.1	STM image of 0.12 ML Au deposited at RT	48
8.2	Au 4 <i>f</i> XPS spectra of a surface containing Au adatoms and for a thick Au film. .	49
8.3	XPS spectra demonstrating chemical stability of adatoms in CO.	50
8.4	Density of Au adatoms as a function of flash-anneal temperature	51
8.5	STM images showing 0.1 ML of Au adatoms after annealing to 673 K, 773 K and 873 K.	52
8.6	Large scale STM images showing Au adatoms after annealing to 773 K and 873 K.	52
8.7	Cluster analysis on 0.4 ML Au deposited at RT.	53
8.8	0.4 ML Au deposited at RT: cluster mobility.	54
8.9	Bar chart showing the change in density of Au adatoms after annealing to 673 K.	54
8.10	STM image of Au deposited at elevated temperature: 0.8 ML Au deposited at 553 K.	55
8.11	STM image of 0.4 ML Au deposited at RT.	56
8.12	LDOS for a clean B layer and for Au adatoms.	57

8.13 Proposed model of Au cluster nucleation.	58
8.14 Nominally 0.2 ML of Pd deposited at RT	61
8.15 Adsorbate induced mobility of one Pd adatom	62
8.16 The effect of CO exposure on Pd adatoms	63
8.17 Overview of an STM movie [82]	64
8.18 Formation of a mobile Pd carbonyl group and a stable Pd adatom at a surface OH	65
8.19 Relaxed geometry obtained from ab-initio GGA+U showing a structural model of a Pd adatom before and after CO adsorption	66
8.20 CO induced formation of a large Pd cluster	67
8.21 Schematic model of each iteration of a Monte Carlo simulation	69
8.22 Monte Carlo simulations of STM images with adatoms	70
8.23 Radial distribution function for a Fe ₃ O ₄ (001) surface with adatoms	71
8.24 Coverage of adatoms as a function of radial travel distance in Monte Carlo simulations	72
8.25 Schematic diagram showing stability of a dimer	73
A.1 STM image of a clean B layer surface with typical defects highlighted in the image	77
A.2 STM image of a flat terrace, containing an APDB	78
A.3 STM image of an Fe-OP terminated surface	78
A.4 STM image of a single Au adatoms	79
A.5 STM image containing single Pd adatoms, one Pd-CO group and one Pd-OH group	79
B.1 STM image of Fe ₃ O ₄ (001)361 sample annealed in UHV and oxygen	85
B.2 Image of the Fe ₃ O ₄ (001)361 SSC taken with an optical microscope	85
B.3 2D color coded map showing Fe/O ratio on areas A to I on Fe ₃ O ₄ (001)361 SSC .	86
B.4 NSC No. 349: STM image of the B layer terminated surface	87
B.5 Fe ₃ O ₄ (001)370 natural: STM image of the Fe-OP terminated surface	87
B.6 STM image of a Fe ₃ O ₄ /MgO(001) thin film	88

List of Tables

8.1	Results of peak fitting of the XP spectra in figure 8.3(b-d). The table shows the BE and FWHM for the Au $4f_{7/2}$ photoelectron peak.	51
A.1	Apparent height of known features on the $\text{Fe}_3\text{O}_4(001)$ surface	77
B.1	List of (001) oriented Fe_3O_4 samples used during the PhD work (1 of 2).	82
B.2	List of (001) oriented Fe_3O_4 samples used during the PhD work (2 of 2).	83

Bibliography

- [1] M. Brown, F. Ringleb, Y. Fujimori, H.-J. F. M. Sterrer, G. Preda, and G. Pacchioni, "Initial formation of positively charged gold on MgO(001) thin films: Identification by experiment and structural assignment by theory," *The Journal of Physical Chemistry C*, vol. 115, pp. 10114–10124, 2011.
- [2] X.-F. Yang, A. Wang, B. Qiao, J. Li, J. Liu, and T. Zhang, "Single-atom catalysts: A new frontier in heterogeneous catalysis," *Acc. Chem. Res. (Published online, doi: 10.1021/ar300361m)*, 2013.
- [3] D. W. Goodman, "Catalytically active Au on Titania: yet another example of a strong metal support interaction (SMSI)?," *Catalysis Letters*, vol. 99, pp. 1–4, 2005.
- [4] M. Valden, X. Lai, and D. W. Goodman, "Onset of catalytic activity of gold clusters on titania with the appearance of nonmetallic properties," *Science*, vol. 281, pp. 1647–1650, 1998.
- [5] G. Hutchings, M. Hall, A. Carley, P. Landon, B. Solsona, C. Kiely, A. Herzing, M. Makkee, J. Moulijn, and A. Overweg, "Role of gold cations in the oxidation of carbon monoxide catalyzed by iron oxide-supported gold," *Journal of Catalysis*, vol. 242, pp. 71–81, 2006.
- [6] S. J. Tauster, S. C. Fung, R. T. K. Baker, and J. A. Horsley, "Strong interactions in supported-metal catalysts," *Science*, vol. 201, pp. 1121–1125, 1981.
- [7] M. Haruta, N. Yamada, T. Kobayashi, and S. Iijima, "Gold catalysts prepared by coprecipitation for low temperature oxidation of hydrogen and of carbon monoxide," *Journal of Catalysis*, vol. 115, pp. 301–309, 1989.
- [8] M. Haruta, "When gold is not noble: catalysis by nanoparticles," *Chemical record*, vol. 3, pp. 75–87, 2003.
- [9] M. Haruta, "Size- and support-dependency in the catalysis of gold," *Catalysis Today*, vol. 36, pp. 153–166, 1997.
- [10] U. Diebold, "The surface science of titanium dioxide," *Surface Science Reports*, vol. 48, pp. 53–229, 2003.
- [11] O. Dulub, M. Batzill, and U. Diebold, "Growth of copper on single crystalline ZnO: Surface study of a model catalyst," *Topics in Catalysis*, vol. 36, pp. 65–76, 2005.

Bibliography

- [12] W. T. Wallace, B. K. Min, and D. W. Goodman, "The nucleation, growth, and stability of oxide-supported metal clusters," *Topics in Catalysis*, vol. 34, pp. 17–30, 2005.
- [13] M. Bowker, "Surface science: The going rate for catalysts," *Nature materials*, vol. 1, pp. 205–6, 2002.
- [14] T. W. Hansen, A. T. Delariva, S. R. Challa, and A. K. Datye, "Sintering of catalytic nanoparticles: Particle migration or Ostwald ripening?," *Accounts of chemical research*, 2013.
- [15] S. B. Simonsen, I. Chorkendorff, S. Dahl, M. Skoglundh, J. Sehested, and S. Helveg, "Direct observations of oxygen-induced platinum nanoparticle ripening studied by in situ TEM," *Journal of the American Chemical Society*, vol. 132, pp. 7968–75, 2010.
- [16] T. Gerber, J. Knudsen, P. Feibelman, E. Granas, P. Stratmann, K. Schulte, J. N. Andersen, and T. Michely, "CO-induced Smoluchowski ripening of Pt cluster arrays on the graphene/Ir(111) moiré," *ACS nano*, vol. 7, pp. 2020–31, 2013.
- [17] D. E. Starr, S. K. Shaikhutdinov, and H.-J. Freund, "Gold supported on oxide surfaces: Environmental effects as studied by STM," *Topics in Catalysis*, vol. 36, pp. 33–41, 2005.
- [18] P. Harris, "Growth and structure of supported metal catalyst particles," *International Materials Reviews*, vol. 40, pp. 97–115, 1995.
- [19] P. A. Thiel, M. Shen, D.-J. Liu, and J. W. Evans, "Adsorbate-enhanced transport of metals on metal surfaces: Oxygen and sulfur on coinage metals," *Journal of Vacuum Science and Technology A*, vol. 28, p. 1285, 2010.
- [20] B. Qiao, A. Wang, X. Yang, L. F. Allard, Z. Jiang, Y. Cui, J. Liu, J. Li, and T. Zhang, "Single-atom catalysis of CO oxidation using Pt₁FeO_x," *Nature chemistry*, vol. 3, pp. 634–641, 2011.
- [21] Q. Fu, H. Saltsburg, and M. Flytzani-Stephanopoulos, "Active nonmetallic Au and Pt species on ceria-based water-gas shift catalysts," *Science*, vol. 301, pp. 935–8, 2003.
- [22] G. Kyriakou, M. Boucher, A. Jewell, E. Lewis, T. Lawton, A. Baber, H. Tierney, M. Flytzani-Stephanopoulos, and C. E. Sykes, "Isolated metal atom geometries as a strategy for selective heterogeneous hydrogenations," *Science*, vol. 335, pp. 1209–1212, 2012.
- [23] R. M. Cornell and U. Schwertmann, *The Iron Oxides: Structure, Properties, Reactions, Occurrences and Uses*. Weinheim: Wiley-VCH, 2003.
- [24] Z. Zhang and S. Satpathy, "Electron states, magnetism, and the Verwey transition in magnetite," *Physical Review B*, vol. 44, pp. 13319–13331, 1991.
- [25] W. Weiss and W. Ranke, "Surface chemistry and catalysis on well-defined epitaxial iron-oxide layers," *Progress in Surface Science*, vol. 70, pp. 1–151, 2002.
- [26] S. Li, S. Krishnamoorthy, A. Li, G. D. Meitzner, and E. Iglesia, "Promoted iron-based catalysts for the Fischer–Tropsch synthesis: Design, synthesis, site densities, and catalytic properties," *Journal of Catalysis*, vol. 206, pp. 202–217, 2002.

- [27] E. Verwey, "Electronic conduction of magnetite ($\text{Fe}_3\text{O}_4(001)$) and its transition point at low temperatures," *Nature*, vol. 144, p. 328, 1939.
- [28] F. Walz, "The Verwey transition - a topical review," *J. Phys.: Condens. Matter*, vol. 14, p. R285, 2002.
- [29] M. S. Senn, J. P. Wright, and J. P. Attfield, "Charge order and three-site distortions in the Verwey structure of magnetite," *Nature*, vol. 481, pp. 173–176, 2012.
- [30] P. Tasker, "The stability of ionic crystal surfaces," *Journal of Physics C: Solid State Physics*, vol. 12, pp. 4977–4984, 1979.
- [31] J. Goniakowski, F. Finocchi, and C. Noguera, "Polarity of oxide surfaces and nanostructures," *Reports on Progress in Physics*, vol. 71, p. 016501, 2008.
- [32] B. Stanka, W. Hebenstreit, U. Diebold, and S. A. Chambers, "Surface reconstruction of $\text{Fe}_3\text{O}_4(001)$," *Surface Science*, vol. 448, pp. 49–63, 2000.
- [33] J. R. Rustad, E. Wasserman, and A. R. Felmy, "A molecular dynamics investigation of surface reconstruction on magnetite (001)," *Surface Science*, vol. 432, pp. L583–L588, 1999.
- [34] G. S. Parkinson, N. Mulakaluri, Y. Losovyj, P. Jacobson, R. Pentcheva, and U. Diebold, "Semiconductor-half metal transition at the $\text{Fe}_3\text{O}_4(001)$ surface upon hydrogen adsorption," *Physical Review B*, vol. 82, p. 125413, 2010.
- [35] R. Pentcheva, F. Wendler, H. L. Meyerheim, W. Moritz, N. Jedrecy, and M. Scheffler, "Jahn-teller stabilization of a "polar" metal oxide surface: $\text{Fe}_3\text{O}_4(001)$," *Physical Review Letters*, vol. 94, p. 126101, 2005.
- [36] R. Wiesendanger, I. V. Shvets, D. Buergler, G. Tarrach, H. J. Guentherodt, J. M. Coey, and S. Graeser, "Topographic and magnetic-sensitive scanning tunneling microscope study of magnetite," *Science*, vol. 255, pp. 583–586, 1992.
- [37] G. Tarrach, D. Buergler, T. Schaub, R. Wiesendanger, and H.-J. Guentherodt, "Atomic surface structure of $\text{Fe}_3\text{O}_4(001)$ in different preparation stages studied by scanning tunneling microscopy," *Surface Science*, vol. 285, pp. 1–14, 1993.
- [38] N. Mulakaluri, R. Pentcheva, M. Wieland, W. Moritz, and M. Scheffler, "Partial dissociation of water on $\text{Fe}_3\text{O}_4(001)$: Adsorbate induced charge and orbital order," *Physical Review Letters*, vol. 103, p. 176102, 2009.
- [39] Z. Novotny, N. Mulakaluri, Z. Edes, M. Schmid, R. Pentcheva, U. Diebold, and G. S. Parkinson, "Probing the surface phase diagram of: Fe_3O_4 towards the Fe rich limit: Evidence for progressive reduction of the surface," *Physical Review B*, vol. 87, p. 195410, 2013.
- [40] Z. Lodziana, "Surface Verwey transition in magnetite," *Physical Review Letters*, vol. 99, p. 206402, 2007.

Bibliography

- [41] R. Pentcheva, W. Moritz, J. Rundgren, S. Frank, D. Schrupp, and M. Scheffler, "A combined DFT/LEED-approach for complex oxide surface determination: $\text{Fe}_3\text{O}_4(001)$," *Surface Science*, vol. 602, pp. 1299–1305, 2008.
- [42] K. J. A. Cazacu, G. Manai, S. F. Ceballos, S. Murphy, and I. V. Shvets, "Scanning tunneling spectroscopy study of the electronic structure of Fe_3O_4 surfaces," *Physical Review B*, vol. 74, p. 085416, 2006.
- [43] G. Binnig, H. Rohrer, C. Gerber, and E. Weibel, "Tunneling through a controllable vacuum gap," *Applied Physics Letters*, vol. 40, pp. 178–180, 1982.
- [44] G. Binnig and H. Rohrer, "Scanning tunneling microscopy," *Surface Science*, vol. 126, pp. 236–244, 1983.
- [45] M. Schmid, "http://en.wikipedia.org/wiki/file:scanningtunnelingmicroscope_schematic.png," Retrieved: July 23rd 2013.
- [46] H.-J. Guentherodt and R. Wiesendanger, *Scanning Tunneling Microscopy I*. Springer, Berlin, Heidelberg, New York, 1994.
- [47] J. W. John F. Watts, *An Introduction to Surface Analysis by XPS and AES*. Wiley, 2003.
- [48] J. W. Rabalais, *Principles and Applications of Ion Scattering Spectrometry: Surface Chemical and Structural Analysis*. Weinheim: John Wiley & Sons, 2003.
- [49] A. Ichimiya, *Reflection High-Energy Electron Diffraction*. Cambridge University Press, 2004.
- [50] E. Napetschnig, "Thin alumina films on $\text{NiAl}(110)$ and $\text{Cu-9\%Al}(111)$: Structure, domain boundaries and nucleation and growth of metallic clusters," *PhD thesis, TU Wien, Austria*, 2008.
- [51] G. S. Parkinson, Z. Novotny, P. Jacobson, M. Schmid, and U. Diebold, "Room temperature water splitting at the surface of magnetite," *Journal of the American Chemical Society*, vol. 133, pp. 12650–5, 2011.
- [52] G. S. Parkinson, T. A. Manz, Z. Novotny, P. T. Sprunger, R. L. Kurtz, M. Schmid, D. S. Sholl, and U. Diebold, "Antiphase domain boundaries at the $\text{Fe}_3\text{O}_4(001)$ surface," *Physical Review B*, vol. 85, p. 195450, 2012.
- [53] G. S. Parkinson, Z. Novotny, P. Jacobson, M. Schmid, and U. Diebold, "A metastable $\text{Fe}(A)$ termination at the $\text{Fe}_3\text{O}_4(001)$ surface," *Surface Science*, vol. 605, pp. L42–L45, 2011.
- [54] Z. Novotny, G. Argentero, Z. Wang, M. Schmid, U. Diebold, and G. S. Parkinson, "Ordered array of single adatoms with remarkable thermal stability: $\text{Au}/\text{Fe}_3\text{O}_4(001)$," *Physical Review Letters*, vol. 108, pp. 6103–6103, 2012.
- [55] G. S. Parkinson, Z. Novotny, G. Argentero, M. Schmid, J. Pavelec, R. Kosak, P. Blaha, and U. Diebold, "Carbon monoxide-induced adatom sintering in a model catalyst: $\text{Pd}/\text{Fe}_3\text{O}_4$," *Nature Materials*, vol. 12, pp. 724–728, 2013.

- [56] S. Nie, E. Starodub, M. Monti, D. A. Siegel, L. Vergara, F. E. Gabaly, N. C. Bartelt, J. de la Figuera, and K. F. McCarty, "Insight into magnetite's redox catalysis from observing surface morphology during oxidation," *Journal of the American Chemical Society*, vol. 135, pp. 10091–10098, 2013.
- [57] N. Mulakaluri, R. Pentcheva, and M. Scheffler, "Coverage-dependent adsorption mode of water on $\text{Fe}_3\text{O}_4(001)$: Insights from first principles calculations," *Journal of Physical Chemistry C*, vol. 114, pp. 11148–11156, 2010.
- [58] C. Peden, G. Herman, I. Ismagilov, B. Kay, M. Henderson, Y. Kim, and S. Chambers, "Model catalyst studies with single crystals and epitaxial thin oxide films," *Catalysis Today*, vol. 51, pp. 513–519, 1999.
- [59] J. M. Pan, B. Maschhoff, U. Diebold, and T. E. Madey, "Interaction of water, oxygen, and hydrogen with $\text{TiO}_2(110)$ surfaces having different defect densities," *Journal of Vacuum Science and Technology A*, vol. 10, pp. 2470–2476, 1992.
- [60] T. Kendelewicz, P. Liu, C. S. Doyle, G. E. Brown, E. J. Nelson, and S. A. Chambers, "Reaction of water with the (100) and (111) surfaces of Fe_3O_4 ," *Surface Science*, vol. 453, pp. 32–46, 2000.
- [61] S. Chambers and S. Joyce, "Surface termination, composition and reconstruction of Fe_3O_4 and $\gamma\text{-Fe}_2\text{O}_3(001)$," *Surface Science*, vol. 420, pp. 111–122, 1999.
- [62] N. Spiridis, J. Barbasz, Z. Lodziana, and J. Korecki, " $\text{Fe}_3\text{O}_4(001)$ films on $\text{Fe}(001)$: Termination and reconstruction of iron-rich surfaces," *Physical Review B*, vol. 74, p. 155423, 2006.
- [63] F. C. Voogt, T. Fujii, P. J. M. Smulders, L. Niesen, M. A. James, and T. Hibma, " NO_2 -assisted molecular-beam epitaxy of Fe_3O_4 , $\text{Fe}_{3-\delta}\text{O}_4$, and $\gamma\text{-Fe}_2\text{O}_3$ thin films on $\text{MgO}(100)$," *Physical Review B*, vol. 60, pp. 11193–11206, 1999.
- [64] K. Reuter and M. Scheffler, "Composition, structure, and stability of $\text{RuO}_2(110)$ as a function of oxygen pressure," *Physical Review B*, vol. 65, p. 035406, 2001.
- [65] J. Ziegler and J. Biersack, "www.srim.org," March 2011.
- [66] K. T. Rim, J. P. Fitts, T. Mueller, K. Adib, N. Camillone, R. M. Osgood, S. A. Joyce, and G. W. Flynn, " CCl_4 chemistry on the reduced seldge of a $\alpha\text{-Fe}_2\text{O}_3(0001)$ surface: a scanning tunneling microscopy study," *Surface Science*, vol. 541, pp. 59–75, 2003.
- [67] N. Spiridis, R. P. Socha, B. Handke, J. Haber, M. Szczepanik, and J. Korecki, "Cluster-supported interaction in $\text{Au-Fe}_3\text{O}_4(001)$ system," *Catalysis Today*, vol. 169, pp. 24–28, 2011.
- [68] K. Jordan, S. Murphy, and I. Shvets, "Initial nucleation of Au on the $(\sqrt{2} \times \sqrt{2})\text{R}45^\circ$ reconstructed $\text{Fe}_3\text{O}_4(001)$ surface," *Surface Science*, vol. 600, pp. 5150–5157, 2006.
- [69] P. Torelli, L. Giordano, S. Benedetti, P. Luches, E. Annese, S. Valeri, and G. Pacchioni, "X-ray photoemission study of the charge state of Au nanoparticles on thin $\text{MgO/Fe}(001)$ films," *The Journal of Physical Chemistry C*, vol. 113, pp. 19957–19965, 2009.

Bibliography

- [70] C. Weilach, C. Spiel, K. Foettinger, and G. Rupprechter, "Carbonate formation on Al_2O_3 thin film model catalyst supports," *Surface Science*, vol. 605, pp. 1503–1509, 2011.
- [71] G. Argentero, "Scanning tunneling microscopy study of the $\text{Fe}_3\text{O}_4(001)$ surface," Master's thesis, University of Turin, Italy, September 2012.
- [72] J. Stroscio, R. Feenstra, and A. Fein, "Electronic structure of the $\text{Si}(111)2 \times 1$ surface by scanning-tunneling microscopy," *Physical Review Letters*, vol. 57, pp. 2579–2582, 1986.
- [73] P. Martensson and R. Feenstra, "Geometric and electronic structure of antimony on the $\text{GaAs}(110)$ surface studied by scanning tunneling microscopy," *Physical Review B*, vol. 39, pp. 7744–7753, 1989.
- [74] L. Giordano, G. Pacchioni, J. Goniakowski, N. Nilius, E. D. L. Rienks, and H.-J. Freund, "Charging of metal adatoms on ultrathin oxide films: Au and Pd on $\text{FeO}/\text{Pt}(111)$," *Physical Review Letters*, vol. 101, p. 026102, 2008.
- [75] D. W. Goodman, "Model catalysts: from imagining to imaging a working surface," *Journal of Catalysis*, vol. 216, pp. 213–222, 2003.
- [76] O. Demoulin, G. Rupprechter, I. Seunier, B. L. Clef, M. Navez, and P. Ruiz, "Investigation of parameters influencing the activation of a Pd/γ -alumina catalyst during methane combustion," *The journal of physical chemistry B*, vol. 109, pp. 20454–62, 2005.
- [77] R. F. Egerton, "Beam-induced motion of adatoms in the transmission electron microscope," *Microscopy and microanalysis*, vol. 19, pp. 479–86, 2013.
- [78] O. L. Krivanek, N. Dellby, M. F. Murfitt, M. F. Chisholm, T. J. Pennycook, K. Suenaga, and V. Nicolosi, "Gentle STEM: ADF imaging and EELS at low primary energies," *Ultra-microscopy*, vol. 110, pp. 935–945, 2010.
- [79] S. R. Challa, A. T. Delariva, T. W. Hansen, S. Helveg, J. Sehested, P. L. Hansen, F. Garzon, and A. K. Datye, "Relating rates of catalyst sintering to the disappearance of individual nanoparticles during Ostwald ripening," *Journal of the American Chemical Society*, vol. 133, pp. 20672–20675, 2011.
- [80] "Movie S3: Pd adatom mobility in UHV. 0.2ML Pd deposited onto clean $\text{Fe}_3\text{O}_4(001)$ surface at RT. The STM movie is comprised of 78 frames acquired over 5 hours 20 minutes under UHV conditions. In the beginning, the sample contains many isolated Pd adatoms, some hydroxyl groups and a few small clusters. The sample area selected for figure 8.15 is indicated by a white square. Over the course of the movie Pd adatoms occasionally become mobile through the interaction with a CO molecule. The mobile Pd carbonyl is trapped by stable Pd adatoms, appearing as a bright "fuzzy" species. This species frequently detaches from its host Pd and diffuses over the surface. In addition to the region of interest, similar events are observed several times through the movie. Movie details: ($50 \times 50\text{nm}^2$, +1V, 0.2nA, $\text{Fe}_3\text{O}_4(001)$ 357, 2012, RT-STM:m10232–m10331)." <http://www.nature.com/nmat/journal/v12/n8/extref/nmat3667-s2.mov>. [Online; Uploaded 23-November-2012].

- [81] S. Horch, H. T. Lorensen, S. Helveg, E. Laegsgaard, I. S. K. W. Jacobsen, J. K. Norskov, and F. Besenbacher, "Enhancement of surface self-diffusion of platinum atoms by adsorbed hydrogen," *Nature*, vol. 398, pp. 134–136, 1999.
- [82] "The effect of CO exposure on a 0.2ML Pd/Fe₃O₄. Initially, the surface contains isolated Pd adatoms, Pd clusters, Pd-H and surface OH. After a short time, CO backpressure in the STM chamber is increased to 5×10^{-10} mbar (indicated in the movie), leading to formation of Pd-carbonyl species. Within a few frames, all the Pd adatoms react with CO and large Pd clusters and Pd-H are formed. Movie details: ($50 \times 50\text{nm}^2$, +1V, 0.3nA, Fe₃O₄(001)357, 2012,RT-STM:m10426–m10460), 36 frames, duration 1 hour 55 minutes." <http://www.nature.com/nmat/journal/v12/n8/extref/nmat3667-s3.mov>. [Online; Uploaded 23-November-2012].
- [83] A. Kolmakov and D. W. Goodman, "Scanning tunneling microscopy of gold clusters on TiO₂(110): CO oxidation at elevated pressures," *Surface Science*, vol. 490, pp. L597–L601, 2001.
- [84] J. G. Tobin, S. A. Morton, S. W. Yu, G. D. Waddill, I. K. Schuller, and S. A. Chambers, "Spin resolved photoelectron spectroscopy of Fe₃O₄: the case against half-metallicity," *Journal of Physics: Condensed Matter*, vol. 19, p. 315218, 2007.
- [85] J. F. Anderson, M. Kuhn, U. Diebold, K. Shaw, P. Stoyanov, and D. Lind, "Surface structure and morphology of Mg-segregated epitaxial Fe₃O₄(001) thin films on MgO(001)," *Physical Review B*, vol. 56, pp. 9902–9909, 1997.

Curriculum Vitae

PERSONAL DETAILS

Zbynek Novotny

Address: Brigittenauer Lände 224/1302, 1200 Vienna, Austria

Phone: +43 680 23 69 790

E-mail: novotny@iap.tuwien.ac.at

EDUCATION

PhD in Engineering Physics

2010-2013*

*(PhD defense and a final exam scheduled for September 3rd 2013)

Vienna University of Technology

Vienna, Austria

Advisor: Prof. Ulrike Diebold

MSc. in Engineering Physics

2008-2010

Brno University of Technology

Brno, Czech Republic

Master's Thesis Advisor: Prof. Peter Varga

BSc. in General Physics

2004-2008

Masaryk University

Brno, Czech Republic

RESEARCH EXPERIENCE

Surface Structure, Adsorption and Reactivity of Metal Oxides 2010-2013

Graduate research supervised by Prof. Ulrike Diebold dedicated to understanding the surface termination, chemical reactivity and adsorption of the of the $\text{Fe}_3\text{O}_4(001)$ at atomic level. Main surface science techniques was STM, supported by XPS, AES, LEED, ISS, FTIR, TPD, SMOKE, HP-XPS, SP-PES and SP-LEEM. Experience with MBE and synchrotron-based techniques.

Ion beam-induced magnetic transformation of thin Fe films on Cu(100)

Undergraduate research supervised by Prof. Peter Varga. Investigation of structure-magnetism relationship of thin Fe films on Cu(100) using SMOKE and LEED.

PUBLICATIONS

Carbon monoxide-induced adatom sintering in a Pd- Fe_3O_4 model catalyst

G.S. Parkinson, **Z. Novotny**, G. Argentero, M. Schmid, J. Pavelec, R. Kosak, P. Blaha, U. Diebold

Nature Materials 12 (2013) 724-728

Probing the surface phase diagram of $\text{Fe}_3\text{O}_4(001)$ towards the Fe rich limit: Evidence for progressive reduction of the surface

Z. Novotny, M. Mulakaluri, Z. Edes, M. Schmid, R. Pentcheva, U. Diebold, G. S. Parkinson

Phys. Rev. B 87 (2013) 195410

Ordered array of single adatoms with remarkable thermal stability: Au/Fe₃O₄(001)
Z. Novotny, G. Argentero, Z. Wang, M. Schmid, U. Diebold, G. S. Parkinson
Phys. Rev. Lett. 108 (2012) 216103

Antiphase domain boundaries at the Fe₃O₄(001) surface
G. S. Parkinson, T. A. Manz, Z. Novotny, P. T. Sprunger, R. L. Kurtz, M. Schmid, D. S. Sholl, U. Diebold
Phys. Rev. B 85 (2012) 195450

Room Temperature Water Splitting at the Surface of Magnetite
G.S. Parkinson, Z. Novotny, P. Jacobson, M. Schmid, U. Diebold
J. Am. Chem. Soc. 133 (2011) 12650-12655

A metastable Fe(A) termination at the Fe₃O₄(001) surface
G.S. Parkinson, Z. Novotny, P. Jacobson, M. Schmid, U. Diebold
Surf. Sci. 605 (2011) L42-L45

Ion beam induced magnetic transformation of CO-stabilized fcc Fe films on Cu(100)
S. Shah Zaman, H. Osmer, J. Jonner, Z. Novotny, A. Buchsbaum, M. Schmid, P. Varga
Phys. Rev. B 82 (2010) 235401

CONTRIBUTED
TALKS

German Physical Society (DPG) Spring Meeting, Regensburg, Germany
CO Induced Adatom Sintering in a Model Catalyst: Pd/Fe₃O₄ Talk

62. Meeting of the Austrian Physical Society, Graz, Austria
Ordered Array of Single Au Adatoms on Fe₃O₄(001) with Remarkable Thermal Stability Talk

29th European Conference on Surface Science 2012, Edinburgh, UK
Ordered Array of Single Au Adatoms on Fe₃O₄(001) with Remarkable Thermal Stability Talk

76. Meeting of the German Physical Society (DPG), Berlin, Germany
Fe Rich Terminations and the Role of Subsurface Charge Order at the Fe₃O₄(001) Surface Talk

25. Symposium on Surface Science 2012, St.Christoph am Arlberg, Austria
Surface Terminations of Fe₃O₄(001) Surface Poster

28th European Conference on Surface Science 2011, Wroclaw, Poland
A Metastable Fe termination of the Fe₃O₄(001) surface Talk

Energy Frontier Research Centers Summit and Forum 2011, Washington D.C., USA
Surface Reactivity of Iron Oxide Talk

Functional Oxide Surfaces and Interfaces - Special Research Program (SFB)
meeting 2011, Vienna, Austria
Surface reactivity of Iron Oxide Poster

RESEARCH STAYS

BESSY II, Berlin, Germany 2012 (two weeks)
Spin-resolved PES experiments on the Fe₃O₄(001) surface

Lawrence Berkeley National Laboratory, California, US 2012 (one week)
Spin-polarized LEEM experiments on the Fe₃O₄(001) surface

Max Lab 2, Lund, Sweden 2012 (two weeks)
High-pressure XPS experiments on the Fe₃O₄(001) surface
XPS and XAS experiments on the SrTiO₃(110)

Paul Scherrer Institute, Villigen, Switzerland 2010 (one week)
Spin-resolved PES experiments on the Fe₃O₄(001) surface

HONORS AND AWARDS

Selected for ECOSS Prize Sessions for the best student talk (2012)

Selected to attend 62nd Lindau Nobel Laureate Meeting (2012)

Dean's prize for outstanding study results (Brno University of Technology, June 2010)

LANGUAGE SKILLS

English, German, Czech

REFERENCES

Prof. Ulrike Diebold
Institut für Angewandte Physik, Technische Universität Wien
Wiedner Hauptstr. 8-10/134, 1040 Wien, Austria
E-mail: diebold@iap.tuwien.ac.at
Phone: Phone: (+43 1) 58801 - 13425

Dr. Gareth S. Parkinson
Institut für Angewandte Physik, Technische Universität Wien
Wiedner Hauptstr. 8-10/134, 1040 Wien, Austria
E-mail: parkinson@iap.tuwien.ac.at
Phone: Phone: (+43 1) 58801 - 13473

Prof. Michael Schmid
Institut für Angewandte Physik, Technische Universität Wien
Wiedner Hauptstr. 8-10/134, 1040 Wien, Austria
E-mail: schmid@iap.tuwien.ac.at
Phone: Phone: (+43 1) 58801 - 13499

Prof. Peter Varga

Institut für Angewandte Physik, Technische Universität Wien

Central European Institute of Technology

Zerotinovo nam. 9, 601 77 Brno, Czech Republic

E-mail: varga@iap.tuwien.ac.at

Phone: Phone: (+43 1) 58801 - 13450